Self-Excited Dust-Density Waves as a Diagnostic of Nanodusty Plasmas

Dissertation
zur Erlangung des Doktorgrades
der Mathematisch-Naturwissenschaftlichen Fakultät
der Christian-Albrechts-Universität zu Kiel

vorgelegt von

Benjamin Tadsen

Kiel, 2018

1. Gutachter:	Prof. Dr. rer. nat. Alexander Piel
2. Gutachter:	Prof. Dr. rer. nat. Sebastian Wolf

Tag der mündlichen Prüfung:	17. Juli 2018
Zum Druck genehmigt:	27. September 2018

gez. Prof. Dr. rer. nat. Frank Kempken, Dekan

Zusammenfassung

Nanostaub ist in vielen natürlichen und technischen Plasmen vorhanden und lädt sich darin je nach den dominierenden Mechanismen positiv oder negativ auf. Wenn Ionen durch eine solche Staubwolke strömen, werden Staubdichtewellen (engl. dust-density waves, DDW) angeregt. Mit herkömmlichen Diagnostiken wie elektrostatischen Sonden oder Emissionsspektroskopie können die Plasmaparameter eines solchen nanostaubigen Plasmas nicht oder nur eingeschränkt bestimmt werden. Diese Dissertation führt eine Diagnostik ein, die dust-density wave diagnostic (DDW-D), mit der diese Parameter aus Wellenzahl und -frequenz der DDW ortsaufgelöst ermittelt werden können. Hierzu werden Wellen in einem nanostaubigen Plasma beobachtet und analysiert, dessen Staubpartikel zuvor in einem Argon-Acetylen Plasma gewachsen sind.
Mithilfe eines hydrodynamischen Modells des komplexen Plasmas aus Staub, Ionen, Elektronen und Neutralen können die beobachteten Wellen mit einer theoretischen Dispersionsrelation verglichen werden. Im Experiment findet sich eine große Variation von Wellenzahl und -frequenz. In Übereinstimmung mit früheren Untersuchungen deutet dies darauf hin, dass die Welle ihre Eigenschaften an die lokal instabilste Mode anpasst, welche durch die Plasmaparameter bestimmt ist.
Die Dominanz der lokal instabilsten Mode verknüpft die im Experiment beobachteten Moden mit den im Modell vorhandenen Plasmaparametern, auf die somit ortsaufgelöst zurückgeschlossen werden kann. Allerdings ist dies erst möglich, wenn ausreichend viele Unbekannte des Modells im Experiment ebenfalls ortsaufgelöst bestimmt werden:
Der Staubradius wird durch Messung des Polarisationszustandes von am Staub gestreutem Laserlicht ermittelt. Außerdem werden Transmissionsbilder der Staubwolke aufgenommen, aus denen mit der inversen Abel-Transformation die ortsaufgelöste Staubdichteverteilung berechnet werden kann.
Durch Anwendung der DDW-D auf das nanostaubige Plasma wird gezeigt, dass die Staubladung durch eine Elektronenverarmung des Plasmas (Havnes-Effekt) nur einige zehn Elementarladungen beträgt. Das Ionendichteprofil weicht von dem sonst beobachteten Glockenprofil ab. Die Elektronendichte folgt in dem Modell nur indirekt und ist um das 100-fache kleiner als die Ionendichte.
Mit den ortsaufgelösten Systemparametern wird es möglich, die Amplitude der Welle mit hydrodynamischer Theorie zu vergleichen. Es konnten die von Theoretikern gefundenen Trends bestätigt werden: Die DDW erhöht ihre Amplitude mit steigender Ionendichte, sinkender Staubladung und sinkender Staubdichte.
Die DDW-D lässt sich auch auf staubige magnetisierte Plasmen anwenden. Dies ist ein neues Gebiet, in dem verschiedene Ansätze verfolgt werden, stabile Bedingungen für Untersuchungen herzustellen. Hier zeigt die DDW-D in Übereinstimmung mit Sondenmessungen im staubfreien Plasma, wie die Ionendichte am Rand der im Magnetfeld eingeschlossenen Plasmasäule abfällt und das elektrische Feld zunimmt. Außerdem wurde beobachtet, dass die Staubwolke ihr Dichtemaximum im magnetisierten Plasma nach außen verschiebt. Dies lässt darauf schließen, dass die Nanostaubwolke im Magnetfeld rotiert, wie es auch schon bei Mikrostaub in magnetisierten Plasmen beobachtet wurde.
Die vorgestellte Methode der DDW-D bietet vielfältige Anwendungsmöglichkeiten für andere staubige Laborplasmen, aber auch für nanostaubige Prozessplasmen.

Abstract

Nanodust can be found in many natural and technical plasmas and attains a charge depending on the charging mechanisms. If ions flow through a cloud of such dust particles, dust-density waves (DDWs) are excited. Common plasma diagnostic techniques like electrostatic probes or emission spectroscopy are inapplicable or are having strong limitations in nanodusty plasmas. This dissertation introduces the dust-density wave diagnostic (DDW-D), which allows to determine the plasma parameters and the dust charge with spatial resolution from the wave frequency and wave number. The waves are observed and analyzed in a nanodusty plasma after the dust has grown in a reactive argon-acetylene plasma.

Using a hydrodynamic model of the complex plasma consisting of dust, ions, electrons, and neutrals, the observed waves can be compared to a theoretical dispersion relation. It is found that the frequency and wave number have strong spatial gradients. In agreement with earlier studies, this indicates that the wave adapts its properties to the local most unstable mode, which is determined by the plasma parameters.

The dominance of the local most unstable mode links the experimentally-observed modes with the plasma parameters in the model, which can be retrieved with spatial resolution. This requires that enough system parameters are measured with spatial resolution in the experiment to reduce the number of unknowns in the model:

The dust radius is found by measuring the polarization state of scattered light from the dust. Additionally, transmission images of the dust cloud are taken that allow to calculate the spatially-resolved dust-density distribution with the inverse Abel transform.

The analysis of the wave data shows that the dust charge is only ten to fifty elementary charges due to electron depletion in the plasma (Havnes effect). The ion density profile deviates from the commonly observed bell-shape profile. The electron density is only indirectly included in the model and is found to be a hundred times smaller than the ion density.

With the spatially-resolved system parameters it becomes possible to compare the amplitude of the wave to hydrodynamic theory. The trends predicted by this model could be confirmed for the first time: The DDW increases its amplitude with increasing ion density and decreasing dust charge and dust density.

The DDW-D can also be applied to dusty magnetized plasmas. This is a new research area, where different approaches to realize stable conditions for experiments are pursued. Here, the DDW-D shows in agreement with probe measurements in the dust-free plasma that the ion density decreases clearly towards the edge of the confined plasma column and that the electric field increases towards this edge. The dust-density distribution shifts its maximum towards the edge of the plasma column if a magnetic field is present. It is concluded that this is a consequence of a rotation of the dust cloud, which was found for micron-sized dust particles in similar situations.

The new diagnostic DDW-D can be applied to many different applications, ranging from basic research to technological nanodusty plasmas.

Contents

1 Introduction

The physics of dusty plasmas originates from astrophysics [1] and has gained increased interest since the early 1980s. Image data of Saturn's rings provided by Voyager-2 [2] showed that spokes in the rings appear dark in backward scattering direction and bright in forward direction. Such behavior indicated that the particles in the spokes must be in the MIE scattering size regime, which meant they must be micron or submicron in diameter [3].

Some years later, G. SELWYN discovered clouds of dust particles levitating in the sheath of rf plasmas used for etching of semiconductor wafers [4]. At roughly the same time, density waves and the COULOMB crystallization in confined particle clouds were predicted theoretically [5, 6]. The predictions could be verified in laboratory experiments in the mid-1990s [7–10], crystallized 3-dimensional systems could be realized a decade later [11]. A variety of different effects have been studied in strongly coupled dusty plasmas, such as the structure of plasma crystals [12], lattice waves [13–15], normal modes in 2D clusters [16, 17], phase transitions [18–21], the influence of a screened potential [22, 23] – to name only a few. In these examples, the dusty plasma is utilized as a model system for solid matter. Its behavior has a certain generality, is simple to observe using digital cameras, and it is easily manipulated with lasers, electric fields, and gas flows. There is a variety of optical diagnostics for the observation and characterization of the dust, such as scattering [24] of polarized light at dust particles to determine properties like size, refractive index, and density of the dust. Holography was used to study the 3D arrangement of particles in a crystal [25] and tomography to resolve the density distribution [26]. The theoretical foundations of dusty plasmas have been summarized in various textbooks [27–33] and review articles [34–42].

From the early stage of laboratory dusty plasma physics, the system itself and its properties have been studied extensively. The dust particle charge was determined with various methods [43–48]. The momentum transfer from ions to dust, the ion drag force, was examined with different theoretical [49–52] and experimental approaches [53, 54]. The ion drag is responsible for the existence of dust-free regions or voids [37, 55–60] and as a force acting on the particles it influences the particle dynamics.

Dusty plasmas have strong impact on technological applications [61]. Reactive plasmas form particles in the gas phase and deposit material on the wall. This allows the creation

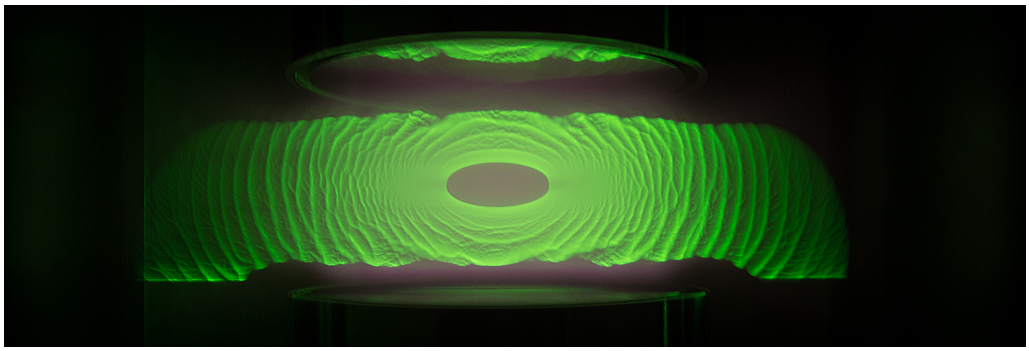

Fig. 1.1: Experimental setup with electrodes at top and bottom. The mid-plane of a 3D dust cloud is illuminated by a laser fan. A reflection of the illuminated plane is visible in the upper electrode surface. Typical properties like a dust-free void in the center and dust-density waves (DDWs) in the cloud volume are clearly visible. [B.4] Additional photos of this geometry are included in the Appendix, Sec. 8.3.

of nanoparticles with special surface properties and the coating of materials with thin films, which are used for many different purposes [62]. In fusion research, transport and control of dust within the fusion device is studied to realize certain plasma conditions despite of an inevitable presence of dust [63–65].

In the following, a plasma whose volume is mainly filled with a significant amount of particles, which are less than 500 nm in diameter, will be called a nanodusty plasma. Basic dusty plasma research is performed in both radio frequency (rf) and direct current (dc) discharges, but usually in a low-temperature plasma environment. Often, it is intended to study the dusty plasma in the absence of gravity. If gravity is too strong, the plasma cannot trap the particles in its bulk. Therefore, dusty plasmas are realized under zero or microgravity conditions on parabolic flights [66, 67], the International Space Station (ISS) [68–70], or in the laboratory. To observe phenomena independent from gravity in a laboratory environment, nanodust particles can be used. Micron-sized particles can be levitated with a thermophoretic force [71, 72].

The dust-density wave (DDW) was first described by RAO *et al.* [6]. Its theoretical model has been refined since [73]. It is a longitudinal wave that emerges if ions drift through a cloud of negatively-charged dust particles. Even the first observation of DDWs in a $SiH_4/O_2/Ar$ discharge [74] was analyzed by matching the observed phase velocity with the theoretical one [75] to determine the dust charge. KORTSHAGEN proposed to use the DDW in plasma-enhanced chemical vapor deposition plasmas to estimate the size of nanoparticles [76]. DDWs in copper [77] and melamin formaldehyde [78] particle clouds trapped inside a plasma have been studied to estimate the particle charge. This allowed to find the reduction of the particle charge as a consequence of charge-exchange collisions of ions with neutrals [45, 51, 79].

In nanodusty plasmas, there is a lack of plasma diagnostic methods. Microwave cavity resonance as well as microwave interferometry can provide the electron density. In principle, the cavity method can provide spatial resolution, but there is a complex weighting

function that averages the measured density. The microwave interferometer averages over its line of sight and has a detection limit. Both methods have been applied to nanodusty plasmas [80–82]. LANGMUIR probes suffer from contamination with dust. Additionally, they are a substantial perturbation to the system. There are only few studies with such probe measurements in dusty plasmas [57, 80, 83, 84]. Emission spectroscopy is difficult to interpret because there is only line-of-sight averaged spatial resolution. Additionally, the dust particles scatter the emitted light as a function of its wavelength.
As diagnostics for the nanodusty plasma are rare, but applications are multifaceted, there are many open questions considering the nanodusty rf discharge: What is the ion density profile like in a dense dust cloud? What is the particle charge and how is the charge distributed within the cloud? How do the dust particles arrange themselves in the plasma? In nanodusty plasmas, dust-density waves as in Fig. 1.1 emerge self-excitedly. The wave is characterized by frequency, wave number, and amplitude. From Fig. 1.1 it becomes clear that these parameters are inhomogeneous in the wave field. The propagating wave adapts its parameters to the local plasma conditions. This thesis aims at providing a new diagnostic, the DDW-D, to retrieve the plasma parameters from the wave number and frequency. With a combination of the observed waves, some additional optical diagnostics, and plasma theory these questions can be approached.
Confinement, charging, and transport of dust in magnetized plasmas are topics that have come up in recent years [85–88]. The DDW shows modified properties, if it propagates through a magnetized plasma [89]. By extending the DDW-D to the case of a magnetized plasma, the transition from the unmagnetized to the magnetized setup can be monitored. In similar systems with micron-sized particles in the sheath of an rf discharge, an entangled rotation of the particles with the neutral gas was found [85].
The basic physics of dusty plasmas is laid out in chapter 2 and the theory of the DDW in chapter 3. An overview of the experimental setup is given in chapter 4. A dedicated description of the newly-developed method DDW-D and its application to the nanodusty plasma can be found in chapter 5. Finally, the preparation of a nanodusty plasma for use in a magnetic field as well as the characterization of this situation with the DDW-D is done in chapter 6, until the conclusions will be discussed in chapter 7.

2 Fundamentals of Dusty Plasmas

The basic concepts of dusty plasma physics including collective effects, charging, and forces acting on dust particles will be introduced in this chapter. Beyond the scope of text books covering this field it is intended to include some advanced aspects and to classify them w.r.t. the experiments presented in the following chapters.
The orbital motion limited theory of dust charging is often not sufficient for a decent calculation of the charge. Additional effects must be considered: There is an increase of the charge as a consequence of an ion flow and a decrease following from charge-exchange collisions of ions with neutrals. If the particle number density is large, then the plasma cannot provide the free-space OML charge to every particle leading to a reduced particle charge.
If the charge can be calculated, this is the foundation for an understanding of the confinement of dust particles in plasmas. The relevant forces will be reviewed. Some rule-of-thumb calculations have been included to illustrate the significance of the presented models for my studies. Two systems have been chosen for these calculations which are representative for a large range of experiments in dusty plasmas: a dusty plasma containing micron-sized particles at low number density and the nanodusty plasma with a high number density of particles.

2.1 Some Collective Effects in Complex (Dusty) Plasmas

A plasma is a system consisting of charged objects. Due to their charge, there is an interaction of every particle with all others. Therefore, the system responds collectively to external and internal perturbations.
Pristine plasmas contain singly and multiply ionized positive ions of a single species, electrons, and neutrals. Complex plasmas can have different kinds of positive and negative ions. Often, this is realized with chemically reactive neutral gases that produce different molecules.
A dusty plasma can be described as a complex plasma with the dust taking the role of a heavy ion species. Thus, a dusty plasma is consisting of electrons (e), ions (i), neutrals, and charged dust particles (d). Generally, the charge of the dust depends on the mechanisms of charging, e.g., photoemission, secondary emission, charging currents from ions

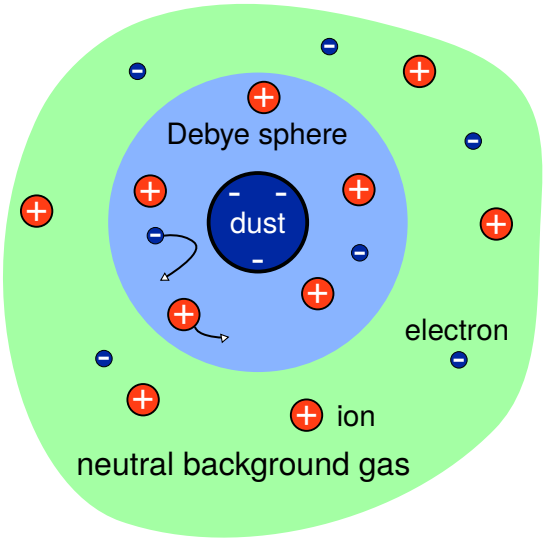

Fig. 2.1: Sketch of a single dust particle in a plasma. The particle is screened by electrons and ions on the scale of the DEBYE length. The charged particles are embedded in a neutral gas having much higher density than all other species. The trajectories of electrons and ions are bent increasing or decreasing their time-averaged density in the DEBYE sphere. This effect decreases with increasing temperature as seen from Eq. (2.3). In a dusty plasma, the DEBYE spheres of neighbouring particles can be overlapping.

and electrons. In this chapter, the characteristics of dusty plasmas with singly charged positive ions of one species, electrons, one type of neutrals and one type of negatively charged dust particles will be discussed. The plasma parameters are such that there are no quantum effects and the dust dynamics follow mostly from classical mechanics.

2.1.1 DEBYE Shielding

In dusty plasmas, electrons, ions, and dust perform thermal motion. They have a kinetic energy as atoms in a gas and collide with neutrals. A dust particle will attract ions in its local neighborhood and it will reject electrons as depicted in Fig. 2.1. This leads to a screening effect called DEBYE shielding. As a consequence, the potential around the dust particle is not of the COULOMB but of the DEBYE-HÜCKEL or of the YUKAWA type:

$$\Phi_{\mathrm{Y}}(r) = \frac{q_{\mathrm{d}}}{4\pi\epsilon_0 r} \exp(-r/\lambda_{\mathrm{D}}) \tag{2.1}$$

with the linearized DEBYE shielding length λ_{D}. Here, it is assumed that the DEBYE length is much larger than the particle radius. The YUKAWA potential is only an approximative ("linearized") solution of the POISSON equation assuming that the charged object produces only a small potential perturbation. This means that in comparison to a charged particle in empty space, whose potential is of the COULOMB type, the potential around a particle in a plasma converges faster to the undisturbed (plasma) potential. As electrons and ions contribute to the shielding, they are both reducing the effective shielding length

$$\lambda_{\mathrm{D}} = \left(\lambda_{\mathrm{De}}^{-2} + \lambda_{\mathrm{Di}}^{-2}\right)^{-1/2} . \tag{2.2}$$

In a plasma with the electron and ion gas at rest, the DEBYE length of a single species depends only on its temperature T_j, density n_j, and charge q_j:

$$\lambda_{\mathrm{D}j} = \sqrt{\frac{\epsilon_0 k_\mathrm{B} T_j}{n_j q_j^2}} \,. \tag{2.3}$$

In low-temperature plasmas, the electron temperature is much higher than the ion temperature. Therefore, the DEBYE length of electrons is much larger than the DEBYE length of ions. In those situations, the DEBYE length is determined by the ion DEBYE length. Flowing ions in a plasma contribute inefficiently to shielding. The DEBYE length is then approximately given by [90, 91]: [1]

$$\lambda_\mathrm{D}^2 \approx \frac{\lambda_\mathrm{De}^2}{1 + k_\mathrm{B} T_\mathrm{e} / (k_\mathrm{B} T_\mathrm{i} + 1/2\, m_\mathrm{i} v_\mathrm{i}^2)} \,. \tag{2.4}$$

In plasmas containing only a few dust particles, e.g., some micron-sized particles in an rf discharge, Fig. 2.1 is a good representative of the situation. In contrast, nanodusty plasmas have very high particle densities and the DEBYE spheres of neighbouring particles can overlap. As the potential between the particles cannot equilibrate to the plasma potential, the plasma properties are significantly influenced by the dust. This distinguishes a dusty plasma from a plasma containing only a few dust particles.

2.1.2 Quasineutrality

As described before, the plasma around a charged object is not neutral as ions are attracted and electrons are repelled. These violations of the neutrality appear only in a sphere with the radius of a DEBYE length. Any uncompensated charge will produce strong electric fields, which lead to the reduction of the local violation of charge neutrality. Therefore, on scales larger than the DEBYE length, the plasma is quasineutral:

$$0 = \sum_k q_k n_k \,. \tag{2.5}$$

Complex plasmas in general may consist of multiply charged positive and negative ions and electrons. In the present investigation, a low-temperature dusty plasma is used with singly-charged positive ions, negatively-charged electrons, and highly negatively-charged dust particles. Then, the quasineutrality condition takes the form

$$n_\mathrm{i} = n_\mathrm{e} + Z_\mathrm{d} n_\mathrm{d} \,. \tag{2.6}$$

The dust charge q_d is represented by the number of elementary charges Z_d residing on a particle. In the dust-free plasma, the ion density n_i equals the electron density n_e whereas

[1] This formula applies if $n_\mathrm{i} = n_\mathrm{e}$. If that is not the case, the increase of the ion DEBYE length can be included by replacing $k_\mathrm{B} T_\mathrm{i}$ in Eq. (2.3) with $k_\mathrm{B} T_\mathrm{i} + 1/2\, m_\mathrm{i} v_\mathrm{i}^2$.

in dusty plasmas the contribution from dust particles may influence this relationship. From Eq. (2.6) one can see that this will only happen if $Z_d n_d$ becomes comparable to n_i.

2.1.3 Thermal Energy in a Plasma: Coupling and Ambipolar Diffusion

Each plasma component can be in the solid, fluid, or gaseous state. The interaction of charged objects favors high coupling whereas the thermal energy in the system reduces coupling. For an ideal gas in three dimensions, the temperature and the particle velocity are connected via

$$\text{(a)} \quad v_{th} = \sqrt{\frac{8k_B T}{\pi m}} \qquad\qquad \text{(b)} \quad v_T = \sqrt{\frac{k_B T}{m}} \tag{2.7}$$

where (a) is mean thermal speed in a gas with MAXWELLIAN velocity distribution and (b) is the standard deviation of this distribution in one space direction. The MAXWELLIAN distribution of speeds is the most important velocity distribution:

$$f_M(v) = 4\pi v^2 n \left(\frac{m}{2\pi k_B T}\right)^{3/2} \exp\left(-\frac{mv^2}{2k_B T}\right) . \tag{2.8}$$

Often, the electron velocity distribution function deviates from MAXWELLIAN because high energy electrons contribute to excitation and ionization of atoms and molecules resulting in a distribution function with a depletion of higher energy states compared to a MAXWELLIAN.

The ratio of potential to kinetic thermal energy determines the state of the particle system and is called the coupling parameter. For charged particles with COULOMB repulsion this parameter is:

$$\Gamma = \frac{q^2}{4\pi\epsilon_0 a_{WS} k_B T} \tag{2.9}$$

with the WIGNER-SEITZ radius $a_{WS} = (4\pi n/3)^{-1/3}$. To incorporate the effect of shielding, the screening parameter $\kappa = a_{WS}/\lambda_D$ for this situation has to be accounted for [92]:

$$\Gamma_Y = \Gamma(1 + \kappa + \kappa^2/2)\exp(-\kappa) . \tag{2.10}$$

Using this parameter to characterize the dust one-component plasma, crystallization appears [93, 94] at roughly $\Gamma_Y = 175$.

In low-temperature argon plasmas, electrons usually have a temperature[2] $k_B T_e$ ranging from 2 eV to 4 eV. The electrons do not thermalize with the neutral gas because their mass is much smaller than that of the neutral gas atoms. Therefore, momentum transfer in collisions of the electrons with neutral gas atoms is inefficient. Ions stay at room temperature or close to it. Consequently, the ion thermal speed is much smaller than the electron thermal speed. This effect is amplified by the ion-to-electron mass ratio.

[2] In this section, the calculations are performed with $k_B T_e = 2.6\,\text{eV}$ matching $T_e/T_i = 100$ and $k_B T_i = 26\,\text{meV}$, which is room temperature.

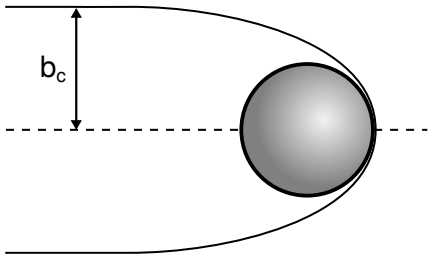

Fig. 2.2: Critical impact parameter of an ion orbiting about a dust particle. An ion of same energy but smaller impact parameter would reach the dust surface.

The plasma in a vessel, which is generated by ionization in the plasma volume, has its density maximum in its center and vanishes at the wall. In such a situation with complete neutrality of the plasma, the free electron diffusion towards the wall is larger than the free ion diffusion. This leads to a charge separation with a slightly positive plasma center and a negative vessel wall. The outward directed electric field arising from this effect is called the ambipolar electric field. This field increases the ion flow and decreases the electron flow towards the wall resulting in equal ambipolar ion and electron flows. The ion flow from the center to the wall is the cause of self-excited dust-density waves.

2.1.4 Coupling and Shielding

There is a relation between coupling and shielding. It can be derived with the number of particles in the DEBYE sphere:

$$N_{\mathrm{D}} = \frac{4}{3}\pi\lambda_{\mathrm{D}}^3 n \; . \tag{2.11}$$

Using this definition, the coupling strength appears in a different form

$$\Gamma = \frac{1}{3}N_{\mathrm{D}}^{-2/3} \; . \tag{2.12}$$

Thus, any plasma species with $\Gamma < 1/3$ has $N_{\mathrm{D}} > 1$.

2.2 Charging of Dust Particles

Charging is the sum of different mechanisms. In astrophysical situations, dust particles are often subjected to UV radiation or high-energy particle beams. By photo- or secondary emission these particles can attain a positive charge. In most laboratory plasmas, charge collection from the surrounding plasma is the dominating effect leading to negatively charged particles. In the following, the charging currents of electrons and ions will be introduced for the laboratory situation.

2.2.1 Orbital Motion Limited Theory

In laboratory plasmas, the high thermal velocity of electrons compared with the ions yields a net negative charge on a spherical particle injected into a plasma. The collection cross section of a point charge with velocity v for impact on a dust particle of attracting

potential Φ is given by

$$\sigma_c = \pi b_c^2 \,, \qquad b_c = a\sqrt{\left(1 - \frac{2q\Phi}{mv^2}\right)} \tag{2.13}$$

with a being the dust particle radius and b_c the critical impact parameter for collection of the point charge. See Fig. 2.2 for a visualization. This is a well known result from the Orbital Motion Limited (OML) theory of spherical LANGMUIR probes [95, 96]. Eq. (2.13) states that – depending on the potential of the dust particle – the critical impact parameter gets larger/smaller than the actual particle radius a.
Using the MAXWELLIAN velocity distribution function from Eq. (2.8) one can calculate the charging current for a repelling potential Φ with $q\Phi > 0$. The minimum velocity of contributing particles is $v_0 = \sqrt{2q\Phi/m}$:

$$I_{\text{rep}} = q \cdot \int_{v_0}^{\infty} v\sigma_c(v) f_M(v) \mathrm{d}v = qn\pi a^2 \sqrt{\frac{8k_\mathrm{B}T}{\pi m}} \exp\left(-\frac{q\Phi}{k_\mathrm{B}T}\right) \,, \tag{2.14}$$

which is an exponential function. In the case of a negatively floating dust particle, Eq. (2.14) would be the correct description of the electron current towards the dust surface.
For an attractive potential one has $q\Phi < 0$. In this case, there is no minimum velocity to overcome the potential barrier:

$$I_{\text{attr}} = q \cdot \int_{0}^{\infty} v\sigma_c(v) f_M(v) \mathrm{d}v = qn\pi a^2 \sqrt{\frac{8k_\mathrm{B}T}{\pi m}} \left(1 - \frac{q\Phi}{k_\mathrm{B}T}\right) \,. \tag{2.15}$$

In a simple model this is used to calculate the ion current on a dust particle.
Even in the bulk of a laboratory low-temperature plasma, the ambipolar electric field causes an ion flow, which is usually in the range of or even faster than the thermal velocity of the ions. Therefore, one has to include the effect of the ion flow on the ion charging current onto a dust particle in many situations. The following formula from Ref. [97] can be used for a spherical object and a COULOMB potential:

$$I_\mathrm{i} = en_\mathrm{i}\pi a^2 v_\mathrm{i} \left[\left(1 + \frac{v_\mathrm{Ti}^2}{2v_\mathrm{i}^2} - \frac{2e\Phi_\mathrm{fl}}{m_\mathrm{i}v_\mathrm{i}^2}\right) \mathrm{erf}\left(\frac{v_\mathrm{i}}{v_\mathrm{Ti}}\right) + \frac{v_\mathrm{Ti}}{\sqrt{\pi}v_\mathrm{i}} \exp\left(-\frac{v_\mathrm{i}^2}{v_\mathrm{Ti}^2}\right)\right] \,. \tag{2.16}$$

The drift velocity of the ion flow is introduced as v_i and the ion thermal velocity as $v_\mathrm{Ti} = \sqrt{2k_\mathrm{B}T_\mathrm{i}/m_\mathrm{i}}$. A discussion of the strength of this effect will be given at the end of this section.

2.2.2 Floating Condition and Dust as a Spherical Capacitor

The ion and electron currents towards a dust particle in a plasma must cancel as the particle reaches its equilibrium charge. This is the floating condition and it determines

the particle potential. It is therefore called the floating potential. Using the Eqs. (2.14) and (2.15) for electrons and ions, the requirement $I_\mathrm{i} + I_\mathrm{e} = 0$ leads to

$$(\mu\tau)^{-1/2}\,(1+\eta_\mathrm{fl}\tau) - \exp(-\eta_\mathrm{fl}) = 0 \tag{2.17}$$

with the normalized quantities

$$\mu = \frac{m_\mathrm{i}}{m_\mathrm{e}}\,, \qquad \tau = \frac{T_\mathrm{e}}{T_\mathrm{i}}\,, \qquad \eta_\mathrm{fl} = -\frac{e\Phi_\mathrm{fl}}{k_\mathrm{B}T_\mathrm{e}}\,. \tag{2.18}$$

This equation allows to calculate the dust particle floating potential Φ_fl. Nevertheless, for the calculation of the dust particle charge one needs a model describing the connection between potential and charge.

The net negative charge on the dust particle is counterbalanced by a positive charge situated in the plasma around the dust particle. Most of this charge is located within the DEBYE sphere. As an approximation one can consider the dust particle in the plasma as a spherical capacitor with the inner electrode being the particle surface and the outer electrode being the DEBYE sphere. The capacitance of a spherical capacitor with radii R_1 and R_2 is

$$C_\mathrm{d} = 4\pi\epsilon_0\frac{R_1R_2}{R_2-R_1} \approx 4\pi\epsilon_0 R_1\,, \qquad R_1 \ll R_2\,. \tag{2.19}$$

If the counter electrode is very far away, the capacitance becomes independent of R_2. This approximation can be applied as the DEBYE length is of the order of tens of microns whereas the dust particles considered here have radii ranging from hundreds of nanometers to a few microns. Then the dust particle charge is given by

$$q_\mathrm{d} = 4\pi\epsilon_0 a\Phi_\mathrm{fl}\,. \tag{2.20}$$

The linear relation between charge and particle size was experimentally confirmed [98]. The equations presented so far allow to calculate the charge of single particles in a plasma. Extensions to this model must be made to include the effect of very dense dust clouds and to cover the influence of collisions that ions might undergo on their trajectories about the dust particle.

2.2.3 Charge Reduction in Dense Dust Clouds (HAVNES-Effect)

The floating condition Eq. (2.17) is independent of the dust particle density n_d because electron and ion densities cancelled assuming they were equal. From the quasineutrality condition in Eq. (2.6) it becomes clear that this assumption is violated if $Z_\mathrm{d}n_\mathrm{d}$ is in the same range as n_i. As a consequence, the plasma is unable to provide all dust particles with their free-space charge. The electron density is reduced resulting in smaller charging currents and in smaller dust particle charges. This effect was first discussed for Saturn's

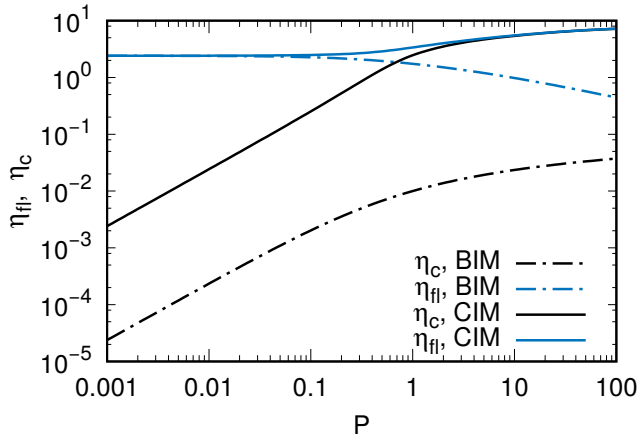

Fig. 2.3: Solution of quasineutrality and floating condition for the Boltzmann ion density model (BIM, dot-dashed lines) and the constant ion density model (CIM, solid lines). The dust-floating potential is shown in blue whereas the cloud floating potential is shown in black.

ring system [3, 99–101], but it was also demonstrated experimentally [83, 102]. It will be pointed out later that the same effect is present in laboratory nanodusty plasmas.
The original works on the HAVNES effect consider a dust cloud which is embedded in a large plasma. In such a situation, the dust cloud is floating in the surrounding plasma environment at a potential Φ_c, attracting ions and repelling electrons. The individual BOLTZMANN distributions of ion and electron densities w.r.t. the floating dust cloud have to be accounted for [100]:

$$n_i = n_0 \exp\left(-\frac{e\Phi_c}{k_B T_i}\right) = n_0 \exp(\eta_c \tau) \,, \quad n_e = n_0 \exp\left(\frac{e\Phi_c}{k_B T_e}\right) = n_0 \exp(-\eta_c) \,. \tag{2.21}$$

The plasma density n_0 refers to the unperturbed electron and ion density outside the dust cloud. In the following, this model will be called the BOLTZMANN ion density model (BIM). The naming convention goes back to Ref. [83]. For the charging mechanism of the dust, the respective densities inside the dust cloud determine the charging currents. The floating condition for this situation is modified:

$$(\mu\tau)^{-1/2}\,(1 + (\eta_{fl} - \eta_c)\tau) - \exp(-\eta_{fl} - \tau\eta_c) = 0 \,. \tag{2.22}$$

The enhanced ion density and reduced electron density in the dust cloud in the presence of the negatively-charged dust must be connected by the quasineutrality condition:

$$\exp(-\eta_c) - \exp(\eta_c \tau) + P(\eta_{fl} - \eta_c) = 0 \,, \qquad P = 4\pi\epsilon_0 a \frac{k_B T_e}{e^2} \frac{n_d}{n_0} \,. \tag{2.23}$$

Floating and quasineutrality condition describe a self-consistent solution for η_{fl} and η_c if fixed values of μ, τ, and P are given. Here, a typical low-temperature argon plasma is considered with $\mu = 72{,}800$ and $\tau = 100$. The values of η_{fl} and η_c for variable P are given in Fig. 2.3. For small P, the cloud potential vanishes and the floating potential is constant. As P gets larger, the normalized floating potential starts to decrease and the normalized cloud potential increases. The small values of the cloud potential already have a large influence on the ion density: At $P = 10$ in the BIM, the normalized cloud

potential is roughly 2×10^{-2}. Thus, the ion density in the cloud is $\exp(2 \times 10^{-2} \cdot 100) \approx 7$ times higher than outside the cloud. Such a high multiplicator for the complete volume of the dust cloud is unrealistic for a laboratory low-temperature plasma that is almost completely filled with dust. To resolve this issue, a HAVNES model without the reference to an external plasma will be introduced below. A comparison to that "local" model below is enabled by calculating the quantities

$$\zeta = \frac{n_\mathrm{e}}{n_\mathrm{i}} = \exp(\eta_\mathrm{c} - \eta_\mathrm{c}\tau) \,, \qquad \eta'_\mathrm{fl} = \eta_\mathrm{fl} - \eta_\mathrm{c} \tag{2.24}$$

instead of the floating and cloud potential η_c, η_fl. For the charging of the dust, only η'_fl is relevant.

As a next step, the ion density will be kept constant outside and inside the dust cloud and only the electron density responds to the cloud potential [31]. In this case, the floating and quasineutrality conditions are:

$$(\mu\tau)^{-1/2}\,(1 + (\eta_\mathrm{fl} - \eta_\mathrm{c})\tau) - \exp(-\eta_\mathrm{fl}) = 0 \tag{2.25}$$

$$\exp\left(-\eta_\mathrm{c}\right) - 1 + P(\eta_\mathrm{fl} - \eta_\mathrm{c}) = 0 \,. \tag{2.26}$$

The solution for this constant ion density model (CIM) is included in Fig. 2.3. Compared with the BIM, the normalized cloud potential increases a lot more. Electrons are more repelled from the cloud. The dust charge is lower at the same values of P.

In a laboratory nanodusty plasma, there is no environment from which additional ions could be attracted. This is why the model equations will now be changed to include only the local electron and ion densities in the dust cloud. In the naming convention, this can be called a LIM (local ion density model). This is equivalent to the assumptions of the CIM. The equivalence is shown in the Appendix, Sec. 8.1. Another reason for the choice of the LIM against the BIM is that in this thesis the DDW will be analyzed locally. Therefore, the parameters provided must only fulfill a local quasineutrality condition.

In the following notation, the cloud potential η_c does not exist because the floating potential η_fl is already referenced to the cloud environment. The floating condition for this situation is:

$$(\mu\tau)^{-1/2}\,(1 + \eta_\mathrm{fl}\tau) - \zeta \cdot \exp(-\eta_\mathrm{fl}) = 0 \,, \qquad \zeta = \frac{n_\mathrm{e}}{n_\mathrm{i}} \,. \tag{2.27}$$

Now, the ratio of electron and ion density ζ appears in the floating condition. This equation contains two unknown variables, namely ζ and η_fl instead of η_c and η_fl in the original model. Inserting the unitless quantities from Eq. (2.18) in the quasineutrality condition Eq. (2.6) yields

$$\zeta - 1 + P \cdot \eta_\mathrm{fl} = 0 \,, \qquad P = 4\pi\epsilon_0 a \frac{k_\mathrm{B} T_\mathrm{e}}{e^2} \frac{n_\mathrm{d}}{n_\mathrm{i}} \,. \tag{2.28}$$

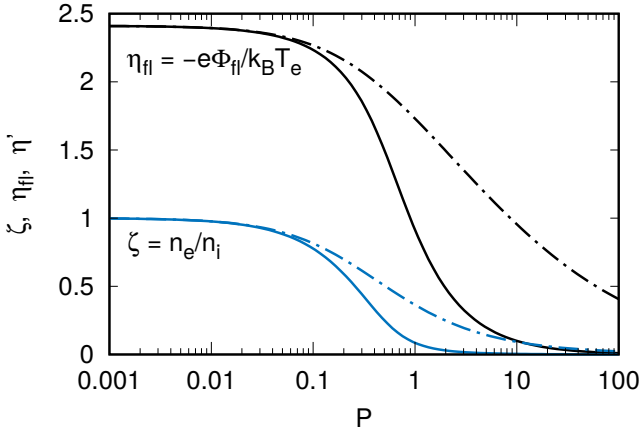

Fig. 2.4: Solution of BIM as dot-dashed lines as well as solution of the local HAVNES effect (LIM) as solid lines w.r.t. the HAVNES parameter P. The unitless quantities $\mu = 72{,}800$ and $\tau = 100$ were chosen to resemble a typical situation in a low-temperature argon plasma. The value 2.41 for η_{fl} in the limit $P \to 0$ is a standard result for the floating potential of a spherical probe.

This HAVNES parameter P is not referenced to the plasma density outside the dust cloud any more, but to the ion density inside the dust cloud. The Eqs. (2.27) and (2.28) form a closed set of equations that determine ζ and η_{fl} depending on the values of P, μ, and τ. In Fig. 2.4, the results for ζ and η_{fl} for the same values of μ and τ as above are shown. If $P = 0$, then $\zeta = 1$ follows directly from Eq. (2.28). In this case, Eq. (2.27) reduces to the standard floating condition as in Eq. (2.17) and the dust charge is only determined by the charging currents. For larger P, the electron density begins to fall and converges to zero. The same applies for the floating potential and the dust charge. These effects are called electron depletion and charge reduction. In the regime $P \gg 1$, the dust charge is only characterized by the quasineutrality condition and can be calculated as $Z_{\mathrm{d}} = n_{\mathrm{i}}/n_{\mathrm{d}}$.
Comparing the BIM with the LIM, it becomes evident that electron depletion and charge reduction appear at much higher values of P in the BIM than in the LIM. This can be attributed to the fact that the BIM allows to pull ions from outside into the cloud. Therefore, the dust charge remains higher in the BIM.
An interesting feature caused by the nonlinearity of the underlying equations is that at the same value of P the electron depletion is quantitatively stronger than the charge reduction. A characteristic location in Fig. 2.4 is at $P = 1$ in the LIM. Here, the electron density is already under 10 % of the ion density whereas η_{fl} is still 40 % of its maximum value.
The HAVNES effect is the dominating process that determines the dust charge in a nanodusty plasma. The ratio $\zeta = n_{\mathrm{e}}/n_{\mathrm{i}}$ introduced in this model stresses that the local densities in the dust cloud are dominating the dust charge.

2.2.4 Charge-Exchange Collisions

With the charging model discussed so far, single dust particles and dense dust clouds can be described and their equilibrium charge can be calculated. The theory of dust charging is closely linked to the theory of a floating LANGMUIR probe. The influence of collisions on the ion current has been a long-standing issue for probes [103–105].

The problem arises from charge-exchange collisions of orbiting ions with neutrals. An ion hitting a neutral can transmit its charge without exchange of momentum. In the case of charge transfer, the neutral loses an electron becoming an ion and its velocity will be a random sample from the velocity distribution function of the neutrals. If an incoming untrapped ion undergoes a charge-exchange collision, it can be replaced by a slow ion that is trapped in the potential well of the dust particle. The ions created from such events will not be able to escape from the potential well unless they are so far away that the thermal energy $k_\mathrm{B}T_\mathrm{n}$ is large enough to overcome the attractive potential Φ. This defines a sphere about the dust particle of radius R_0 with the following properties [106]:

$$e\Phi(R_0) = -k_\mathrm{B}T_\mathrm{n}\,, \qquad \frac{a\Phi_\mathrm{fl}}{R_0}\exp\left(-\frac{R_0}{\lambda_\mathrm{D}}\right) = -\frac{k_\mathrm{B}T_\mathrm{n}}{e}\,. \tag{2.29}$$

Ions that enter the sphere with radius R_0 and suffer a charge-exchange collision will probably contribute to the ion current on the dust particle. These events can substantially increase the ion current to the dust particle above the OML value introduced in Eq. (2.15) because R_0 is usually large compared with the DEBYE length.
The probability of a charge-exchange collision is approximately R_0/λ_mfp [107] assuming a weakly collisional plasma with $R_0 \ll \lambda_\mathrm{mfp}$. The exact probability can be derived to be $(4/3)R_0/\lambda_\mathrm{mfp}$ [108]. Weighting the ion current into the sphere with the probability of a collision results in the collision-induced ion current to the dust particle:

$$I_\mathrm{corr} = n_\mathrm{i}e\sqrt{\frac{8k_\mathrm{B}T_\mathrm{i}}{\pi m_\mathrm{i}}}\left[\pi R_0^2 - \pi a^2\left(1-\frac{e\Phi_\mathrm{fl}}{k_\mathrm{B}T_\mathrm{i}}\right)\right]\frac{R_0}{\lambda_\mathrm{mfp}}\,. \tag{2.30}$$

The OML current was subtracted as the ions in the OML term will reach the dust surface anyway, regardless of whether they experience a charge-exchange collision. Since the OML current multiplied with the probability of a collision can be neglected, the corrected ion current on a dust particle is

$$I_\mathrm{i} = n_\mathrm{i}e\sqrt{\frac{8k_\mathrm{B}T_\mathrm{i}}{\pi m_\mathrm{i}}}\pi a^2\left(1-\frac{e\Phi_\mathrm{fl}}{k_\mathrm{B}T_\mathrm{i}}+\frac{R_0^3}{a^2\lambda_\mathrm{mfp}}\right)\,. \tag{2.31}$$

KHRAPAK *et al.* [106] have shown that the solution for R_0 can approximately be written as a quadratic correction to the linear OML formula:

$$\beta_\mathrm{T} = \frac{Z_\mathrm{d}e^2}{4\pi\epsilon_0 k_\mathrm{B}T_\mathrm{i}\lambda_\mathrm{D}}\,, \qquad \frac{R_0^3}{a^2\lambda_\mathrm{mfp}} \approx H(\beta)\left(\frac{e\Phi_\mathrm{fl}}{k_\mathrm{B}T_\mathrm{i}}\right)^2\frac{\lambda_\mathrm{D}}{\lambda_\mathrm{mfp}}\,. \tag{2.32}$$

β is called the thermal scattering parameter. H is only a weak function of β and is approximately 0.1. The mean-free path can be calculated from the cross section for charge-exchange collisions σ_cx:

$$\lambda_\mathrm{mfp} = \frac{1}{\sigma_\mathrm{cx}n} = \frac{k_\mathrm{B}T_\mathrm{n}}{\sigma_\mathrm{cx}p_\mathrm{n}}\,. \tag{2.33}$$

	Microdust	Nanodust
a / nm	3,000	150
n_d / m^{-3}	1×10^{11}	3×10^{13}
P	0.5	8
$\lvert q_{\mathrm{d}0}\rvert/e$	13,000	650
$\lvert q_\mathrm{d}\rvert/e$	7,700	33
n_e / m^{-3}	2.3×10^{14}	5.6×10^{12}
Γ	7,800	3

Tab. 2.1: Typical parameters of dusty plasmas with micron-sized and nanodust. Shown are the respective values of the dust density n_d, HAVNES Parameter P, and electron density n_e. The dust charge is presented for the case of isolated particles in an otherwise dust-free plasma as $q_{\mathrm{d}0}$ as well as in a cloud with the given dust density n_d using the LIM HAVNES model as q_d. In the latter case, the coupling parameter Γ is calculated.

The effect of charge-exchange collisions was picked up in the discussion of dust charging after dust charges determined from the observation of dust-density waves [45, 78, 79] were a factor of 2 smaller than expected. Since then, this is an established model which has to be considered when calculating the dust charge. The influence of charge-exchange collisions in the plasma sheath is discussed in Ref. [108].

2.2.5 Example Calculations of the Dust Charge

To illustrate the considerations so far, the dust charge is now calculated for some typical situations that can be realized in low-temperature dusty plasma experiments. Therefore, we assume an ambient argon plasma with an ion density $n_\mathrm{i} = 10^{15}\,\mathrm{m}^{-3}$ and an electron temperature of $k_\mathrm{B}T_\mathrm{e} = 2.6\,\mathrm{eV}$ as well as an ion temperature of $k_\mathrm{B}T_\mathrm{i} = 25\,\mathrm{meV}$. Starting with a stationary plasma, there are no flows or drifts and the simple OML theory presented in Sec. 2.2.1 applies.

Two situations are compared: First, a plasma with injected micron-sized dust particles, which have a radius of 3 microns, is considered. Due to their size, these particles are usually too heavy to be confined in the bulk plasma. Therefore, experiments with dust clouds are often realized under weightless conditions, e.g., on the ISS or on parabolic flights. Typical values of such a system are presented in the left column of Tab. 2.1. Second, the same setup is filled with in-situ grown nanodust particles. The chosen size of 150 nm leads to a mass ratio of the two kinds of dust of $20^3 = 8{,}000$. The respective parameters of the nanodusty system can be found in the right column of Tab. 2.1.

Comparing the two situations, it is found that the dust charge in the nanodusty plasma is much more reduced than in a cloud of micron-sized dust particles. As there is currently no method to realize the high densities of nanodusty systems in clouds of micron-sized particles, the strong reduction of the charge in a cloud of nanodust particles is an exclusive property of this system affecting the electron density, which is almost unchanged between the dusty and the dust-free situation.

Now, extensions to the OML current theory should be included. Tab. 2.1 represents four situations for which the ion currents in the OML frame have been calculated. In an ex-

tended model with charge-exchange collisions the ratio of the collision-induced to the OML ion current determines whether collisions have to be accounted for. For an example calculation, a neutral pressure of $p_n = 11.5\,\mathrm{Pa}$ is set. The cross section σ_{cx} for the charge exchange process $Ar^+ + Ar \longrightarrow Ar + Ar^+$ is energy-dependent. Here, ions with $50 - 100\,\mathrm{meV}$ are considered. A comparison of experimental results for σ_{cx} can be found in Ref. [109]. For low-energy ions, the data from Ref. [110] point out that there is not much variation in σ_{cx} for the energy range under scrutiny. Therefore, a constant $\sigma_{cx} \approx 6 \times 10^{-19}\,\mathrm{m}^2$ is a good approximation. In the dust-free plasma, the ion current from ion-neutral collisions is always significant. For the micron-sized particle, it is about 28 % of the OML ion current, for the nanoparticle it is even 270 %. In the dusty situation with micron-sized dust, this ratio of currents is almost unchanged whereas in the nanodusty plasma the ratio is decreased to less than 3 %. This means that – out of the four considered situations – the effect of charge-exchange collisions can only be neglected in a dense nanodust cloud. In all cases the sphere radius R_0 is significantly smaller than the interparticle distance.

Another effect is the flow of ions through the dust cloud. A typical drift velocity of argon ions in the bulk plasma is 25 % of the ion sound (BOHM) velocity $v_B = \sqrt{k_B T_e / m_i}$. At such a flow velocity the ion current is reduced to only half of its OML value in all cases but the nanodusty plasma. In the nanodusty situation, the ion current is only decreased to 60 % of its OML value. The resulting charge of the nanodust particle will not change because it is mainly determined by the quasineutrality condition, not by the charging currents. But since the charging currents must be equal and now the ion current is lower, the resulting electron density will be even smaller than shown in Tab. 2.1.

2.3 Forces on Dust Particles

For the setup of a dusty plasma experiment, the confinement of dust particles in the plasma is essential. The basic forces that provide the particle confinement are discussed here. For a description of the complete confinement situation, practically all system parameters must be included whose quantities cannot be determined fully from the experiment. Therefore, a broad overview is preferred over a detailed discussion of confinement. In Fig. 2.5, the confining forces acting on the dust particles are sketched for the situation of a dust cloud being trapped in a plasma between two electrodes.

2.3.1 Gravity

The gravitational force on dust particles scales with the third power of the radius:

$$\mathbf{F_G} = \frac{4}{3}\,\pi a^3 \rho\,\mathbf{g}\,. \tag{2.34}$$

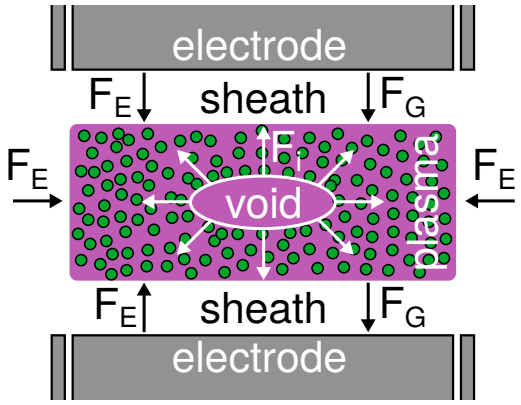

Fig. 2.5: Sketch of the confinement situation of dust (green circles) in the parallel-plate rf plasma. The dust particles experience the gravitational ($\mathbf{F_G}$), the ion drag ($\mathbf{F_i}$), and electrostatic forces ($\mathbf{F_E}$). The motion of the particles is damped by collisions with neutrals. These forces trap the dust into the plasma bulk (pink area). The sheath in front of the electrodes and the central volume, the void, remain dust-free.

This restricts experiments with micrometer-sized dust particles because the confining forces in the plasma bulk are much smaller than gravity. Therefore, many experiments were performed on parabolic flights, on the ISS, on a sounding rocket, or in a falling setup. Particles below the micrometer size range can be confined within the plasma even in presence of gravity. A typical result for the mass density[3] of hydrogenated carbonaceous (a-C:H) material is $\rho \approx 1{,}300\,\mathrm{kg\,m^{-3}}$. It is assumed here that this constant applies to the plasma-grown dust particles as well.

2.3.2 Electrostatic Force

The ambipolar electrostatic field in the bulk plasma is directed towards the wall of the chamber and therefore pulls the negatively-charged dust particles into the discharge center. In the plasma bulk, the electric field is much weaker than in the sheath in front of the wall or the electrode. It depends on the particle mass whether the electrostatic force can balance gravity in the plasma bulk or in the sheath.

$$\mathbf{F_E} = q_\mathrm{d} \cdot \mathbf{E} \propto a \tag{2.35}$$

If the HAVNES parameter is small, the electrostatic force scales linearly with the particle radius. In nanodusty plasmas, the strength of the electrostatic force depends mostly on the dust density because of the HAVNES effect.

2.3.3 Friction with Neutral Gas

A relative motion between dust particles and neutral background gas produces a frictional force that reduces the relative motion:

$$\mathbf{F_N} = -m_\mathrm{d}\nu_\mathrm{dn}(\mathbf{v_d} - \mathbf{v_n})\,, \qquad \nu_\mathrm{dn} = \delta\,\frac{32}{3}\,a^2\,\frac{p_\mathrm{n}}{v_\mathrm{th,n} m_\mathrm{d}}\,, \qquad v_\mathrm{th,n} = \sqrt{\frac{8k_\mathrm{B}T_\mathrm{n}}{\pi m_\mathrm{n}}}\,. \tag{2.36}$$

This is called EPSTEIN friction [112]. The coefficient δ has a value of 1.44 in the case of gas atoms that are reflected from heavy dust particles, which was confirmed experimentally

[3] The value used here can be found in Tab. I of Ref. [111]. It was determined for a layer of a-C:H material created with plasma-enhanced chemical vapor deposition (PECVD).

for different gases [B.1]. In experiments with dusty plasmas, a flow of the neutral gas can be present to renew the gas or it can be a consequence of the magnetization of the plasma. If there is a temperature gradient in the neutral gas, then the gas will flow against the gradient and transfer momentum on the dust particles. This force is called the thermophoretic force and can be written as [71]:

$$\mathrm{F_{th}} = -3.33\frac{k_\mathrm{B}a^2}{\sigma}\nabla T_\mathrm{n} \; . \tag{2.37}$$

2.3.4 Ion Drag

The ion drag force appears if there is a relative motion between the ions and the dust particles. Ions impinging on the surface of the dust particle transfer their complete momentum to the dust particle. The resulting force is called collection force $\mathrm{F_C}$. An ion whose trajectory is deflected by the YUKAWA potential of the dust particle also transmits momentum to the dust because it changes its direction. The force from scattering of ions is called orbit force. The ion drag force is the sum of the collection force and of the orbit force:

$$\mathrm{F_i} = \mathrm{F_c} + \mathrm{F_o} \; . \tag{2.38}$$

Beginning with the collection force and assuming a monoenergetic ion beam, the collection force is simply given by the product of the OML cross section and the momentum flow of ions arriving at that cross section:

$$\mathrm{F_c} = n_\mathrm{i} m_\mathrm{i} v_\mathrm{i}^2 \pi a^2 \left(1 - \frac{2e\Phi_\mathrm{fl}}{m_\mathrm{i} v_\mathrm{i}^2}\right) \; . \tag{2.39}$$

In general, the flowing ions in a plasma are not monoenergetic but have a MAXWELLIAN velocity distribution function. To account for this distribution, BARNES *et al.* replaced the flow velocity with a "mean speed" v_s [49]:

$$\mathrm{F_c} = n_\mathrm{i} m_\mathrm{i} v_\mathrm{i} v_\mathrm{s} \pi a^2 \left(1 - \frac{2e\Phi_\mathrm{fl}}{m_\mathrm{i} v_\mathrm{s}^2}\right), \qquad v_\mathrm{s} = \sqrt{v_\mathrm{i}^2 + \frac{8k_\mathrm{B}T_\mathrm{i}}{\pi m_\mathrm{i}}} \; . \tag{2.40}$$

The two-term structure in Eq. (2.40) shows the transition from low to high ion flow velocities: The influence of the distribution function becomes important when the ion flow velocity is small. Eq. (2.40) is not the mathematical solution to average the OML momentum transfer with a shifted MAXWELLIAN but it is rather a heuristic ansatz. The analytically correct formula would be [52]:

$$\begin{aligned} \mathrm{F_c} \;=\; & n_\mathrm{i} a^2 m_\mathrm{i} v_\mathrm{Ti}^2 \frac{\sqrt{\pi}}{2} \left\{ u \left(2u^2 + 1 - 2\frac{e\Phi_\mathrm{fl}}{k_\mathrm{B}T_\mathrm{i}}\right) \exp(-u^2) \right. \\ & \left. + \left[4u^4 + 4u^2 - 1 + 2(1-2u^2)\frac{e\Phi_\mathrm{fl}}{k_\mathrm{B}T_\mathrm{i}}\right] \frac{\sqrt{\pi}}{2}\mathrm{erf}(u) \right\} / u^2 \end{aligned} \tag{2.41}$$

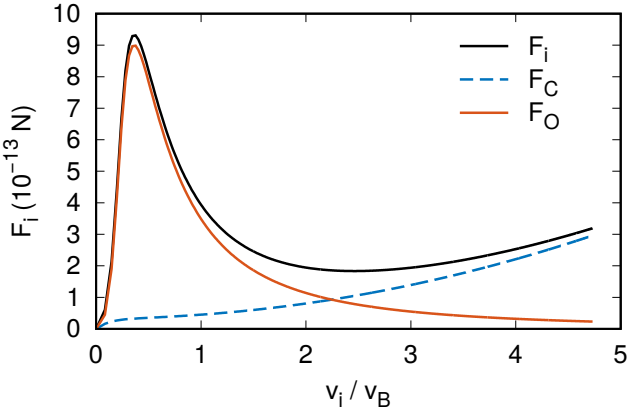

Fig. 2.6: Ion drag force for the micron-sized dust particle (left column of Tab. 2.1) using the formulas from BARNES [49]. At small drift velocities, the orbit force is dominating, at large drift velocities the collection force determines the ion drag.

with $v_{\mathrm{Ti}} = \sqrt{2k_{\mathrm{B}}T_{\mathrm{i}}/m_{\mathrm{i}}}$ as in Eq. (2.16). u denotes the relative ion flow velocity $u = v_{\mathrm{i}}/v_{\mathrm{Ti}}$. The calculation of the orbit force is a well-known problem if the interaction between the particles is of the COULOMB type. In the collisionless limit, this is the RUTHERFORD scattering problem. Drifting ions in a plasma can be considered collisionless while passing the dust particle, if the pressure is not too high. But the interaction is of the YUKAWA type. To solve this problem, it is usually assumed that this interaction can be reproduced by integrating the momentum transfer in the COULOMB case over all ions that have impact parameters between the critical collection impact parameter and one DEBYE length. This is called the cut-off approximation. The orbit force can be obtained by integration of the momentum transfer for every differential scattering cross section over all scattering angles that apply for ions that have impact parameters between b_{c} and λ_{D}. In the BARNES model, this yields:

$$\mathrm{F_o} = 4\pi r_{\mathrm{C}}^2 n_{\mathrm{i}} m_{\mathrm{i}} v_{\mathrm{i}} v_{\mathrm{s}} \ln\left(\sqrt{\frac{r_{\mathrm{C}}^2+\lambda_{\mathrm{D}}^2}{r_{\mathrm{C}}^2+b_{\mathrm{c}}^2}}\right), \qquad r_{\mathrm{C}} = -\frac{eq_{\mathrm{d}}}{4\pi\epsilon_0 m_{\mathrm{i}} v_{\mathrm{i}}^2} \tag{2.42}$$

with r_{C} being the COULOMB scattering parameter and b_{c} being defined in Eq. (2.13). The logarithm in this equation is called COULOMB logarithm, often shortened as $\ln\Lambda$. There are many refinements of this theory, especially by integration of the ion velocity distribution [50, 51] and by applying PIC simulations [91]. The most important analytical improvement on the cut-off assumption was to use a modified COULOMB logarithm [50]:

$$\ln(\Lambda) = \ln\left(\frac{r_{\mathrm{C}}+\lambda_{\mathrm{D}}}{r_{\mathrm{C}}+a}\right). \tag{2.43}$$

This expression is obtained when the cut-off is extended to all ions whose maximum distance from the dust particle during their orbit is one DEBYE length.

To take into account the velocity distribution function of the ions in the orbit force, the model from HUTCHINSON is presented here [52]:

$$F_{\mathrm{o}} = n_{\mathrm{i}} \frac{e^2\Phi^2}{m_{\mathrm{i}} v_{\mathrm{Ti}}^2} a^2 8\pi G(u) \ln(\Lambda) \,, \tag{2.44}$$

$$G(u) = \left[\mathrm{erf}(u) - 2u \exp\left(-u^2\right) / \sqrt{\pi}\right] / \left(2u^2\right) \tag{2.45}$$

with the above-mentioned refined COULOMB logarithm. HUTCHINSON extended this theory further in order to match this formula with PIC computation results [91]. These are only valid for micron-sized dust particles and therefore not considered here.
Obviously, the correct choice of the DEBYE length is crucial because it determines the upper limit of the integration and has therefore a significant influence on the results. Usually, a drift-modified shielding length is applied, e.g., as in Eq. (2.4).
The separation of the ion drag force into orbit and collection force is illustrated in Fig. 2.6 for the micron-sized dust particle. The force is calculated as a function of the ion drift velocity. For low drift velocity, there is a distinct maximum of the orbit force. At larger flow velocities, the ion trajectories straighten and the orbit force gets smaller. At very large drift velocities, the collection force determines the overall ion drag force.

2.3.5 Interparticle Force

The interparticle force follows from the YUKAWA potential by derivation:

$$\mathrm{F_Y}(r_{12}) = -q_{\mathrm{d}} \nabla \Phi_{\mathrm{Y}} = -\frac{q_{\mathrm{d}}^2}{4\pi\epsilon_0 r_{12}^2} \left(1 + \frac{r_{12}}{\lambda_{\mathrm{D}}}\right) \exp\left(-\frac{r_{12}}{\lambda_{\mathrm{D}}}\right) \,. \tag{2.46}$$

The interparticle distance is given by r_{12}. The repulsion of two neighbouring dust particles in a dust cloud provides the spatial extent of the dust cloud.

2.3.6 Comparison of Forces

The forces that have been introduced determine the confinement of the dust particles in a dusty plasma. A closer discussion of Fig. 2.5 is now possible. The confinement depends strongly on the actual situation with its parameters. Here, the examples given above with micron-sized and nano-sized particles in a low-temperature rf plasma are pursued. For the two systems in Tab. 2.1 the typical forces have been calculated and collected in Tab. 2.2.
Beginning with the gravitational force that scales $\propto a^3$, the micron-sized dust particles cannot be levitated by the ambipolar electric field. Therefore, such particles drop into the plasma sheath in front of the electrode where a much stronger electric field is able to compensate the gravitational force. In this system, spatially-extended dust clouds in the bulk plasma are created under zero- or microgravity conditions or using a thermophoretic force. In the nanodusty system, the electrostatic confinement excels gravity roughly by a

	Microdust (10^{-13} N)	Nanodust (10^{-16} N)
gravity	14	1.8
electrostatic	4	16
interparticle	0.1	2
ion drag	0.4	2

Tab. 2.2: Typical values of forces for the two considered systems in Tab. 2.1. Mass density $\rho = 1{,}300\,\mathrm{kg\,m^{-3}}$ and an ambipolar electric field $\mathrm{E} = 300\,\mathrm{V\,m^{-1}}$ have been assumed. For the calculations, the reduced charge $|q_\mathrm{d}|$ was used.

factor of ten. The system is therefore only weakly affected by gravity and the dust stays in the bulk plasma.

In both systems, the interparticle forces are typically smaller than the confining forces and the ion drag is usually smaller than the electrostatic force because otherwise an equilibrium position inside the dust cloud would not be possible. In the plasma sheath, the electrostatic force is even stronger than in the plasma bulk. Therefore, the dust cloud cannot extend into the sheath and remains trapped in the bulk plasma.

In most 3D dusty plasmas, a small central volume remains dust-free or void. This volume is characterized by a high ion density and a low ion flow velocity. This behavior becomes clear from the ion drag and electrostatic force as a function of the ion flow velocity in Fig. 2.7. Ion drag and electrostatic force are pointing in opposite directions. These forces are laid out for a micron-sized particle in Fig. 2.7 (a): At low ion drift velocity, the ion drag force excels the electrostatic force. The particles are pushed outside. With increasing distance from the plasma center, the drift velocity gets larger and the electrostatic force excels the ion drag force. At the intersection of the two curves, there is a stable position, at least in the HUTCHINSON model. Since the dust cannot move into the plasma center where the small ion drift velocity leads to large ion drag, the central volume is dust-free (void) and the dust cloud arranges itself "above" the void edge, the position of vanishing net force.

The difference between the two models can be attributed to the influence of the ion velocity distribution. If the flow velocity is comparable to the ion thermal velocity v_Ti, there is an effect of the velocity distribution function on the ion drag. This is included correctly in the HUTCHINSON model. At larger drift velocities, there is no difference between the models.

In the nanodusty situation [Fig. 2.7 (b)], the BARNES model predicts a high peak of the orbit force, which is not reproduced by the HUTCHINSON formula. At larger drift velocities, both models agree well. For nanodust particles, the ion drag is poorly investigated and the presented calculations must be handled with care: The nanodust particles have interparticle distances that are in the same range than the DEBYE length. Therefore, ions can be influenced by more than one dust particle during the orbital transit. This is a conditon for which a correct model is not yet available.

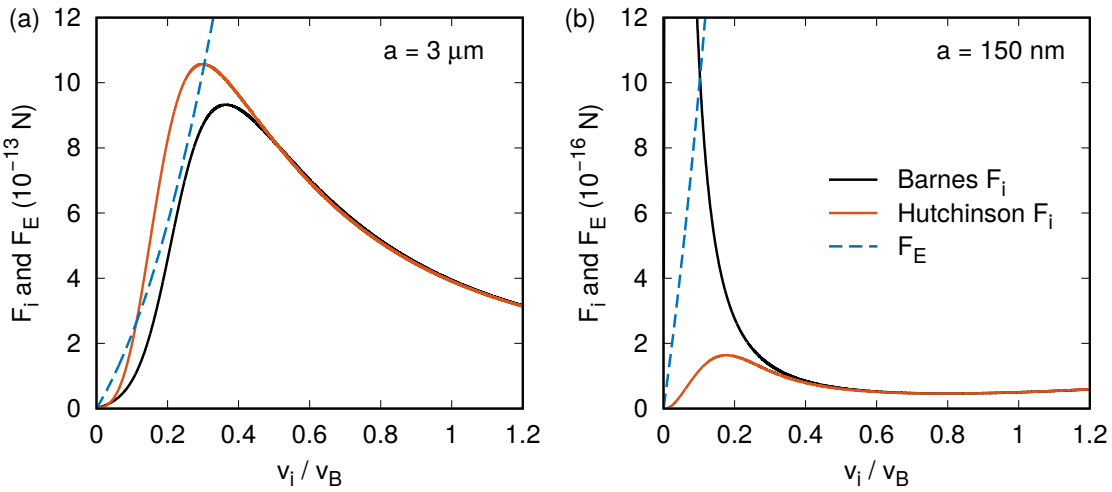

Fig. 2.7: Example calculation of the ion drag force and the electrostatic force as a function of the ion drift velocity. The underlying parameters are those from Tab. 2.1, mainly an argon ion density of $1 \times 10^{15}\,\mathrm{m}^{-3}$, a neutral pressure of 11.5 Pa, and a dust charge of (a) 7,700 elementary charges for the micron-sized particle and (b) 33 elementary charges for the nano-sized particle.

Electrostatic and ion drag force do not scale identically with the particle size. This is why dusty plasmas demix particles of different size. If a force equilibrium is given for a certain particle group, particles that are larger or smaller, cannot be in force equilibrium at the same position. It is observed that mixtures of different particle sizes separate spatially in a diffusion process [67, 113]. When one group of particles penetrates another, lane formation was observed [114] during the demixing of the groups. In the nanodusty plasma, shells of different particle sizes could be observed [115].

Concluding this chapter, it can be stated that the basic models must be applied to each system individually. The nanodusty plasma with its unique properties like low particle charge, low coupling parameter, and high number density differs from the more widely investigated microdusty plasma in many ways, which makes it interesting for further studies.

3 Theory of Dust-Density Waves

The dust-density wave (DDW) is – compared to other plasma modes, e.g., the ion-acoustic wave – a low-frequency wave due to the inertia of the dust particles. The excitation of the wave is a consequence of the relative motion of the dust and the ions in the plasma. Therefore, the DDW is a BUNEMAN-type instability [116, 117], also called an ion-dust streaming instability [118].
It is often referred to as a dust-acoustic wave (DAW). In the following, dust-density wave will be the preferred name. After an historical overview of the past 25 years of DDW research, the underlying mechanism will be derived in the fluid model, for the general case of a magnetized plasma. The unmagnetized limit will follow as a simplified case. The kinetic model and the most unstable mode as well as their importance for the experiments will be discussed. This chapter will be completed by the presentation of some example dispersion relations and their interplay with the plasma parameters.

3.1 Historical Remarks

The DDW was first discussed in the frame of fluid/hydrodynamic theory by RAO *et al.* [6]. A first observation was made in an in-situ grown dust cloud of a $SiH_4/O_2/Ar$ plasma [74], which was later interpreted as a dust-acoustic wave [75].
Since the mid-1990s many laboratory investigations of DDWs have been performed, e.g., with dust particles in anodic plasmas [10, 119]. The dispersion relation was measured experimentally by applying a modulation signal to the anode potential [120, 121]. Experiments under microgravity conditions with parallel-plate discharges were carried out with a modulation of the electrode potential [122–124]. This allowed the estimation of particle charges by comparison with fluid theory. Oblique propagation of the wave with respect to the ion flow direction was theoretically considered and found in clouds of micron-sized dust particles under microgravity conditions [125, 126]. The synchronization behavior of DDWs with external modulation was put under scrutiny [127–129]. Spatial frequency clustering with similarities to the VAN DER POL oscillator was found [130]. Many experiments were focused on measuring the spatial growth rate of the DDW amplitude [131–134], and on quantifying nonlinearity effects if the amplitude saturates like the generation of harmonics [135–137], sawtooth-like and shock waves [138, 139].

Micron-sized dust particles can be observed on the kinetic level, which allows to investigate the wave-particle interaction in the nonlinear regime. Using this method, it was found that the wave is kinetically heating the dust population [140–145]. By reducing the neutral pressure, the wave field could be driven to turbulent behavior [137, 146]. At high amplitudes, it was possible to observe a dust-dust streaming instability within a wave trough [139]. Under certain circumstances, the wave can provide enough kinetic energy to even overcome the repelling forces of the dust particles leading to sticking events [147, 148]. Another type of experiments covered the modification of the DDW due to strong coupling [149–151].

3.2 The Governing Equations

A plasma can be described by the MAXWELL equations, the law of continuity, and the momentum transfer equation. Such a fluid description of the dust system is justified for weakly coupled dust. The experiments conducted here only facilitate low-density low-temperature plasmas. Thus, plasma-induced magnetic fields and currents can be neglected completely. Then, the governing equations are the law of continuity

$$0 = \frac{\partial n_j}{\partial t} + \nabla \cdot (n_j \mathbf{v_j}) \tag{3.1}$$

with j representing one of the plasma constituents ions (i), electrons (e), and dust (d), the POISSON equation

$$\nabla^2 \Phi = -\frac{\rho}{\epsilon_0} = -\sum_{j=\mathrm{e,\,i,\,d}} \frac{q_j n_j}{\epsilon_0} \tag{3.2}$$

with the plasma potential Φ and the charge density ρ, as well as the momentum transfer equation:

$$\frac{\partial \mathbf{v_j}}{\partial t} + (\mathbf{v_j} \cdot \nabla)\mathbf{v_j} = -\frac{q_j}{m_j}\nabla\Phi + \frac{q_j}{m_j}(\mathbf{v_j} \times \mathbf{B}) - \nu_{j\mathrm{n}}\mathbf{v_j} - \frac{v_{\mathrm{T}j}^2}{n_{j0}}\nabla n_j \tag{3.3}$$

with the magnetic induction $\mathbf{B}$, the friction rate $\nu_{j\mathrm{n}}$, and the thermal velocity $v_{\mathrm{T}j} = \sqrt{k_\mathrm{B} T_j / m_j}$. Without loss of generality, it will be assumed that the magnetic field is aligned with the z-axis of the system. The given equations are valid for all species j and the momentum transfer equation has 3 dimensions, so this totals to a system of 13 equations.
So far, two simplifications have been made: The continuity equation assumes that ionization and neutralization in the plasma reach an equilibrium. The hydrodynamic/fluid approach does not take into account a distribution function of the velocities. Apart from that, these equations fully describe the system dynamics.

3.3 Perturbation Analysis and Dispersion Relation

A perturbation analysis of the governing equations yields the stable and unstable modes of the system. Therefore, a plane wave is assumed with fluctuating velocities, densities and potential:

$$\mathbf{v_j} = \mathbf{v_{0j}} + \tilde{\mathbf{v}}_\mathbf{j} \exp(\mathrm{i}(\mathbf{k}\cdot\mathbf{r} - \omega t)) \,, \tag{3.4}$$

$$n_j = n_{0j} + \tilde{n}_j \exp(\mathrm{i}(\mathbf{k}\cdot\mathbf{r} - \omega t)) \,, \tag{3.5}$$

$$\Phi = -\mathbf{E_0}\cdot\mathbf{r} + \Phi_0 + \tilde{\Phi}\exp(\mathrm{i}(\mathbf{k}\cdot\mathbf{r} - \omega t)) \,. \tag{3.6}$$

The offsets $\mathbf{v_{0j}}$ and n_{0j} are independent of space and time. Insertion in the continuity equation and neglecting second-order products of the form $\tilde{n}_j\tilde{\mathbf{v}}_\mathbf{j}$ results in

$$\tilde{n}_j = n_{0j}\frac{\tilde{\mathbf{v}}_\mathbf{j}\cdot\mathbf{k}}{\Omega_{1j}} \,, \qquad \Omega_{1j} = \omega - \mathbf{k}\cdot\mathbf{v_{0j}} \,. \tag{3.7}$$

The density perturbation depends on the DOPPLER-shifted wave frequency Ω_{1j}. Doing the same with the POISSON equation and inserting the quasineutrality condition, the density and potential modulations are linked:

$$0 = 1 + \sum_{j=\mathrm{e,i,d}} \chi_j \,, \qquad \chi_j = -\frac{q_j\tilde{n}_j}{\epsilon_0 k^2\tilde{\Phi}} \,. \tag{3.8}$$

χ_j is the susceptibility, e.g., 1 represents the vacuum susceptibility, and k is the absolute value of $\mathbf{k}$. Finally, the plane wave ansatz is inserted into the momentum transfer equation. Again, second-order products are neglected. Then, two sorts of contributions in the equation must be distinguished: oscillating terms determine the wave behavior whereas non-oscillating terms determine the force equilibrium. The non-oscillating terms must cancel each other because otherwise the system would not stay in place. This yields a drift of the corresponding plasma species that consumes the momentum from the electric field into neutral friction. With this additional condition, the mobility tensor M follows in general

$$\mathbf{v_{0j}} = M\,\mathbf{E_0} = \mu \begin{pmatrix} (1+\mu^2B^2)^{-1} & \mu B(1+\mu^2B^2)^{-1} & 0 \\ -\mu B(1+\mu^2B^2)^{-1} & (1+\mu^2B^2)^{-1} & 0 \\ 0 & 0 & 1 \end{pmatrix} \mathbf{E_0} \,. \tag{3.9}$$

The four entries in the upper left corner form a sub-matrix, which describes the motion in the plane perpendicular to the magnetic field direction. For a strong magnetic field, the non-diagonal elements of the submatrix are dominating. Then, the particle motion is perpendicular to $\mathbf{E}$ and $\mathbf{B}$ resulting in the $\mathbf{E}\times\mathbf{B}$ drift:

$$\mathbf{v_{0j}} = \frac{\mathbf{E}\times\mathbf{B}}{B^2} \,. \tag{3.10}$$

At intermediate magnetic inductions, $B = 1/\mu$, the diagonal and the non-diagonal elements are equal. Therefore, the current parallel (PEDERSEN current) and perpendicular (HALL current) to the electric field are equal. For low magnetic inductions, the entries on the diagonal are dominating. In the unmagnetized case, this simplifies to:

$$\mathbf{v_{0j}} = \mu \mathbf{E_0} \,, \qquad \mu = q_j/(m_j \nu_{jn}) \tag{3.11}$$

with μ being the mobility of the unmagnetized species. These equations are important for a description of ions in ambipolar electric fields. Their mobility μ has a weak dependence on the strength of the electric field [152]. The electrostatic force in Fig. 2.6 shows a light upward bending because the ion mobility depends on the electric field.
The solution of $\mathbf{v_{0j}}$ determines the state of the system, e.g., a constant flow of ions is present that can excite the DDW. For the dust, such a flow does not have to be present because the uncompensated forces from the confinement situation cancel with the interparticle interaction.
Next, the oscillating part in the momentum transfer Eq. (3.3) is considered. The solution for $\tilde{\mathbf{v}}_\mathbf{j}$ from the momentum transfer equation together with the solution for $\tilde{n}_j$ from the continuity equation and the POISSON Eq. (3.8) determine the dispersion relation of the DDW in the hydrodynamic/fluid model:

$$0 = 1 + \sum_{j=\mathrm{e,i,d}} \chi_j \,, \qquad \chi_j = \frac{\omega_{\mathrm{p}j}^2 \Omega_{1\mathrm{c}j}^2}{k^2 v_{\mathrm{T}j}^2 \Omega_{1\mathrm{c}j}^2 - \Omega_{1j}\Omega_{2j}\Omega_{2\mathrm{c}j}^2} \,, \tag{3.12}$$

where some useful abbreviations have been introduced:

$$\begin{aligned} \Omega_{1j} &= \omega - \mathbf{k}\cdot\mathbf{v_{0j}} \,, & \Omega_{2j} &= \omega - \mathbf{k}\cdot\mathbf{v_{0j}} + i\nu_{jn} \,, \\ \Omega_{1\mathrm{c}j}^2 &= \Omega_{2j}^2 - \omega_{\mathrm{c}j}^2 \cos^2\theta \,, & \Omega_{2\mathrm{c}j}^2 &= \Omega_{2j}^2 - \omega_{\mathrm{c}j}^2 \end{aligned} \tag{3.13}$$

with θ being the angle between $\mathbf{B}$ and $\mathbf{k}$, the plasma frequencies $\omega_{\mathrm{p}j} = q_j\sqrt{n_j/\epsilon_0 m_j}$, and thermal velocities $v_{\mathrm{T}j} = \sqrt{k_\mathrm{B} T_\mathrm{j}/m_j}$. Here, the cyclotron frequencies $\omega_{\mathrm{c}j} = q_j B/m_j$ are introduced. Ω_{2j} is the DOPPLER-shifted frequency Ω_{1j} with the addition of neutral friction. Ω_{2j} enters the dispersion relation by the momentum transfer equation. The frequencies $\Omega_{1\mathrm{c}j}$, $\Omega_{2\mathrm{c}j}$ represent the influence of the magnetic field, which is strongest if the wave propagates perpendicularly to the magnetic field. The term $k^2 v_{\mathrm{T}j}^2$ is included due to the thermal pressure in the momentum transfer equation and will therefore be named thermal pressure term below. An equivalent expression to Eq. (3.12), though for the cold plasma limit $T \to 0$, was given in Ref. [153].
In general, the wave propagates with an oblique orientation towards the magnetic field and the ion flow direction. The wave frequency ω can be interpreted as a complex number. Its real and imaginary parts are each a function of the wave vector $\mathbf{k}$. The real part represents the actual oscillation frequency and the imaginary part represents the growth

rate. A negative growth rate means that the mode is damped. Those modes cannot survive in the system and will not be observed. The growing modes are of interest.
Most dusty plasma experiments are conducted in the absence of a magnetic field. In the unmagnetized limit of Eq. (3.12) the dispersion relation follows directly:

$$\epsilon(\omega,k) = 0 = 1 + \sum_{j=\mathrm{e,i,d}} \chi_j \,, \qquad \chi_j = \frac{\omega_{\mathrm{p}j}^2}{k^2 v_{\mathrm{T}j}^2 - \Omega_{1j}\Omega_{2j}} \,. \tag{3.14}$$

The dispersion relation in the electrostatic case is given by the dielectric function $\epsilon(\omega, k)$. In my experimental situation the unstable waves have reached saturation. In this equilibrium state, all modes experience additional damping, which is not included in the linear dispersion theory. Such stabilizing mechanisms are wave-particle interaction, heating, trapping, mode coupling with the harmonics, and turbulence. These effects have been studied in the context of the BUNEMAN instability. The nonlinear development after the initial linear stage yields saturation of the most unstable mode, which is still dominating the saturated system [154–156].
The linear perturbation theory does not only predict the self-excitation mechanism by finding the growing modes, it is also able to describe the spatial growth of the wave when an ion beam enters the dust cloud. Such a situation is given at the void edge in my experiment. For this purpose, the wave number k can be assumed to be complex in the dispersion relation Eq. (3.12) and the real and imaginary part of k are determined as a function of ω. The validity of these spatial growth rates is also limited to a small region, in which saturation does not occur.

3.4 Kinetic Model

The influence of the velocity distribution function is modeled by using the momentum transfer equation as a differential equation for the distribution function. Assuming a MAXWELLIAN velocity distribution leads to a susceptibility of the following form [118, 157]:

$$\chi_j = \frac{1}{k^2\lambda_{\mathrm{D}j}^2} \frac{1 + \zeta_j \cdot Z(\zeta_j)}{1 + (\mathrm{i}\nu_{j\mathrm{n}}/(\sqrt{2}kv_{\mathrm{T}j}))Z(\zeta_j)} \tag{3.15}$$

with $\zeta_j = \Omega_{2j}/(\sqrt{2}kv_{\mathrm{T}j})$ and the plasma dispersion function

$$Z(\zeta) = \frac{1}{\sqrt{\pi}} \int_{-\infty}^{\infty} \frac{\exp(-t^2)}{t-\zeta} \mathrm{d}t \,, \tag{3.16}$$

which is computed with a PADÉ approximation [158].

3.5 The Temperature of Flowing Ions

Due to the self-consistent ambipolar electric field in the plasma, the ions are flowing from the center towards the wall. As they experience collisions with neutrals, their kinetic energy is translated into their thermal motion. This effect increases the ion temperature significantly above room temperature and has been discussed by TROTTENBERG *et al.* [119] using the mean ion energy from Refs. [159, 160]:

$$T_\mathrm{i}(v_\mathrm{i}) = T_\mathrm{n} + \frac{\pi - 2}{6k_\mathrm{B}} m_\mathrm{i} v_\mathrm{i}^2 \,. \tag{3.17}$$

The increase in the ion temperature due to the second term on the right-hand side is usually equal to or larger than the temperature of neutrals.

3.6 Some Practical Simplifications

The DDW frequency is very low due to the high mass of the dust particles in situations with micron-sized particles or due to the low charge of the nano-sized particles. In mathematical terms, this is a consequence of the low dust plasma frequency:

$$\mathrm{Re}(\omega),\ \mathrm{Im}(\omega) \sim \omega_\mathrm{pd} \approx 100 \ldots 2{,}000\,\mathrm{rad\,s^{-1}} \,. \tag{3.18}$$

DDWs show typical wave numbers $k \sim 10^4\,\mathrm{rad\,m^{-1}}$ and are excited at ion flow velocities of $v_\mathrm{i} \sim 10^3\,\mathrm{m/s}$. For the calculation of the wave dispersion relation in the unmagnetized case, Eq. (3.14) must be solved for all values of k. A lot of input variables are needed for this, but many are already defined in the preceding sections. The electron friction rate can be derived with the total electron-neutral collision cross section σ_en as well as neutral pressure p_n and temperature T_n:

$$\nu_\mathrm{en} = \frac{p_\mathrm{n} \sigma_\mathrm{en} v_\mathrm{th,e}}{k_\mathrm{B} T_\mathrm{n}} \,. \tag{3.19}$$

The cross section for electron-neutral collisions is roughly $5 \times 10^{-20}\,\mathrm{m^2}$. A complete table of energy-dependent cross sections can be found in Ref. [161]. Additionally, the electron flow velocity can be found from the equality of electron and ion currents. This requirement yields $v_\mathrm{e} = (n_\mathrm{i}/n_\mathrm{e}) v_\mathrm{i}$. The dust is assumed to be non-drifting.
In the following, the contributions to the susceptibility of each plasma component will be discussed.

3.6.1 Dust Susceptibility

The DDW frequency is the main quantity and dominating against thermal pressure of the dust population (cold dust). This might not hold true if it is assumed that the dust is heated by wave activity. But as there is no way to probe the single-particle motion

in a nanodust cloud, this remains the assumption of choice. The imaginary part of the susceptibility is given by the wave frequency and the dust-neutral friction rate. The dust particles have no net flow and experience no DOPPLER shift of the wave frequency. This means that the dust susceptibility is almost independent of the wave number. The dust-neutral friction rate can be calculated using the EPSTEIN formula in Eq. (2.36).

3.6.2 Ion Susceptibility

The ion plasma frequency is three orders of magnitude larger than the dust plasma frequency. The same applies for the DOPPLER shift frequency $kv_{0\mathrm{i}}$ that appears due to the ion flow velocity. The wave frequency is three orders of magnitude smaller than the ion-neutral friction rate. Consequently, the ion susceptibility can be considered as being completely independent of the wave frequency. This was demonstrated for the micro-dusty situation in Ref. [126] and applies here, too. The thermal pressure term kv_{Ti} and the DOPPLER shift are only separated by usually less than an order of magnitude. Hence, the ion temperature cannot be neglected. The complex part of the ion susceptibility is introduced completely due to the ion-neutral collisions.

3.6.3 Electron Susceptibility

The electron contribution to the DDW is different from ions and dust in many ways. The overall susceptibility of electrons is almost two orders of magnitude smaller than the dust and the ion susceptibility. Neglecting electrons completely would therefore introduce an error of only a few percent. Nevertheless, a correct model of the electron gas can be kept even with strong simplifications. The wave frequency is six orders of magnitude, the electron-neutral friction rate two orders of magnitude, and the electron DOPPLER shift one order of magnitude smaller than the thermal pressure frequency for electrons at typical conditions ($k_{\mathrm{B}}T_{\mathrm{e}} = 2.6\,\mathrm{eV}$, $p_{\mathrm{n}} = 11.5\,\mathrm{Pa}$). Therefore, the electron susceptibility is considered independent of the electron current, wave frequency, and neutral friction.

3.6.4 Approximative Solutions

Using all of these simplifications, the dispersion relation takes a quadratic form in ω:[1]

$$0 = 1 + \frac{1}{k^2\lambda_{\mathrm{De}}^2} + \frac{\omega_{\mathrm{pi}}^2}{k^2 v_{\mathrm{Ti}}^2 + \mathbf{k}\cdot\mathbf{v}_{\mathrm{i}}(-\mathbf{k}\cdot\mathbf{v}_{\mathrm{i}} + \mathrm{i}\nu_{\mathrm{in}})} + \frac{\omega_{\mathrm{pd}}^2}{k^2 v_{\mathrm{Td}}^2 - \omega(\omega + \mathrm{i}\nu_{\mathrm{dn}})}\,, \tag{3.20}$$

for which an analytic solution can be given:

$$\omega = -\mathrm{i}\frac{\nu_{\mathrm{dn}}}{2} + \sqrt{-\frac{\nu_{\mathrm{dn}}^2}{4} + k^2 v_{\mathrm{Td}}^2 + \frac{\omega_{\mathrm{pd}}^2}{1 + \chi_{\mathrm{e}} + \chi_{\mathrm{i}}}}\,, \tag{3.21}$$

[1] The index "0" is dropped, since the perturbed quantities do not appear any more in the dispersion relation.

$$\chi_\mathrm{e} = \frac{1}{k^2\lambda_\mathrm{De}^2}\,, \qquad \chi_\mathrm{i} = \frac{\omega_\mathrm{pi}^2}{k^2 v_\mathrm{Ti}^2 + \mathbf{k}\cdot\mathbf{v}_\mathrm{i}(-\mathbf{k}\cdot\mathbf{v}_\mathrm{i} + \mathrm{i}\nu_\mathrm{in})}\,. \tag{3.22}$$

If the solution of ω needs to be calculated for many values of k, this analytical form saves much cpu time. It is important to note that Eq. (3.22) can be replaced with the susceptibilities derived in the kinetic model Eq. (3.15) to retain the effect of LANDAU damping. Then, $\omega = 0$ has to be inserted which is a justified approximation as proven above. This is important for ions because the phase velocity of the DDW is comparable to the thermal velocity in the moving frame of reference of the flowing ions.
With Eq. (3.21) a very simple form of the dispersion relation can be reached by making some rough approximations. Assuming that the friction rates vanish, the dust is cold, and the ions are not streaming, the solution for ω yields:

$$\omega^2 = k^2 \frac{q_\mathrm{d}^2 n_\mathrm{d}}{\epsilon_0 m_\mathrm{d}} \frac{\lambda_\mathrm{D}^2}{1 + k^2\lambda_\mathrm{D}^2}\,. \tag{3.23}$$

This is equivalent to Eq. (7) in Ref. [6], thus it is the original result of RAO. He called the respective instability "dust-acoustic waves" (DAW) because the dispersion relation becomes linear for small values of k. Therefore, this model will be referred to as the DAW model in contrast to the fluid description above, which also includes neutral friction rates and plasma flows. In the DAW model, the phase velocity $v_\varphi = \omega/k$ follows in the limit of small k:

$$v_\varphi = \sqrt{\frac{Z_\mathrm{d}^2 n_\mathrm{d}/n_\mathrm{i}}{1 + \frac{n_\mathrm{e} T_\mathrm{i}}{n_\mathrm{i} T_\mathrm{e}}} \frac{k_\mathrm{B} T_\mathrm{i}}{m_\mathrm{d}}}\,. \tag{3.24}$$

Even if these formulas follow from approximations that do not apply directly to the experiments, they show the basic properties of the DDW/DAW. Since $T_\mathrm{i}/T_\mathrm{e} \to 0$, one can see that the phase velocity is mainly determined by the dust charge and the ratio of dust to ion density. The dust mass limits the phase velocity. The parameters of the electrons are almost irrelevant for the behavior of the wave.

3.7 Comparison of the Models

All plasma constituents participate in the dust-density wave. Therefore, a correct description of the susceptibilities in terms of the kinetic model would be desirable for all plasma species. Solving the dispersion relation numerically is time-consuming. If the kinetic model was applied to electrons, ions, and dust, this effort is inevitable.
The speed-up given by the analytical solution of Eq. (3.21) is tremendous, but it requires that the fluid/hydrodynamic description is applied to the dust. Since the susceptibilites of a plasma species are independent entries of the POISSON equation, different models can be applied to form some kind of hybrid dispersion relation.

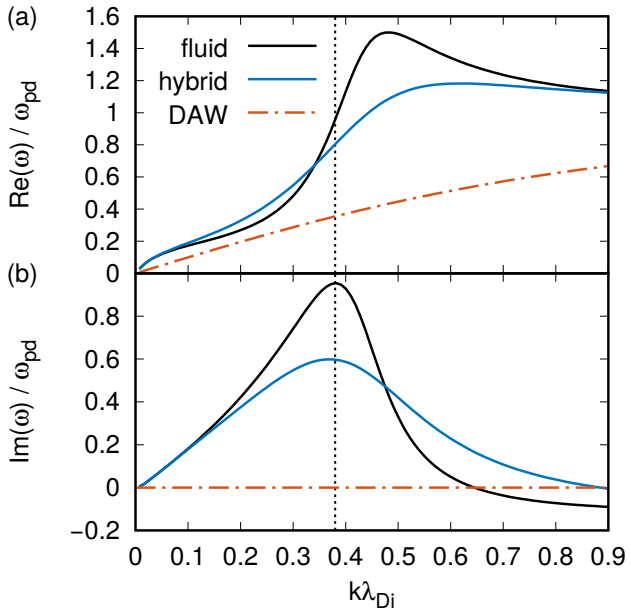

Fig. 3.1: Dispersion relations for the nanodusty situation depicted in the right column of Tab. 2.1. The frequencies have been normalized to the dust plasma frequency and the wave lengths are normalized to the ion DEBYE length. The dispersion is separated into (a) the real part of the frequency and (b) the imaginary part or growth rate. The depicted models are: the fluid model, the hybrid model of fluid description for dust and electrons and kinetic description of ions as well as the DAW model of Eq. (3.23). The most unstable mode is marked with a vertical dashed line in the fluid model. The most unstable mode of the hybrid model is only slightly shifted to the left and therefore not shown.

As stated above, the dust thermal velocity is far below the wave phase velocity and therefore, it cannot be expected that the velocity distribution of the dust interacts with the wave. A fluid description of the dust particles is fully justified. For the ions, this is not the case. They experience the DOPPLER shifted phase velocity of the wave due to their drift motion. In the preceding chapter, it was discussed that at typical conditions in the plasma bulk, the ion thermal velocity is comparable to the ion drift velocity. This made it necessary to correctly integrate over the velocity distribution function in order to get a decent estimate of the ion drag force. The same applies for the ion susceptibility. The slowly drifting ions in the plasma bulk have a thermal velocity comparable to the DOPPLER-shifted phase velocity of the wave. The velocity distribution function of the ions contributes to the excitation of the wave by inverse LANDAU damping. Therefore, the ion velocity distribution must be taken into account and a kinetic model for the ions improves the quality of the complete model significantly. Since the electron susceptibility is not important for the overall wave properties, the electrons can be modelled with the fluid ansatz given above.

A comparison of the resulting dispersion relation for the fluid model, the hybrid model, and the DAW model is shown in Fig. 3.1. In agreement with the arguments given above, the fluid and the hybrid description of the system are similar, but they do not provide identical results. A typical behavior of the fluid model is that the real part of ω rises far above the dust plasma frequency in a kind of overshoot. With the kinetic description of ions, this behavior is suppressed.

The DAW model provides completely different frequencies. It should be noted that this model cannot be used for the experimentally observed waves since it does not take into account the ion drift and the friction rates. The growth rate given by the DAW model is zero. It does not predict self-excited waves. The self-excitation mechanism is due to a balance of energy provided by the ion flow that gets lost in friction of dust and ions with neutrals.

The dispersion relation calculated with the fluid or hybrid model is a complex-valued function. The imaginary part of the frequency denotes the growth rate of the wave. A general constraint for the existence of the wave is that the growth rate must be positive or zero. If all modes are damped, the wave cannot emerge self-excitedly. It could still be driven by external modulation, of course. In those situations where the wave is unstable, usually a wide range of modes is unstable at the same time. In the linear stage of the wave growth, the fastest growing (most unstable) mode dominates the amplitude spectrum. All other modes need more time to develop. In the nonlinear growth stage, the amplitude saturates and all modes are stabilized. The waves in the experiment have grown to this saturated amplitude. Therefore, the observed wave has a growth rate of zero for its resulting mode. It is assumed (and plausible) that this surviving mode is similar – if not equal – to the fastest growing or most unstable mode from the model. This assumption is supported by simulations of the BUNEMAN instability in Ref. [162] where it was shown that the energy spectrum of the saturated wave remains centered about the most unstable mode from linear theory. The most unstable mode is marked by a vertical dashed line in Fig. 3.1 (b).

The most unstable mode is at almost the same value of the wave number in the fluid and the hybrid model. The respective frequencies differ only by a few percent. For very small wave numbers, the models coincide. At intermediate wave numbers, the hybrid model predicts smaller growth rates and at large wave numbers larger growth rates than the fluid model.

3.8 Oblique Modes – An Example of the Most Unstable Mode

In the subsequent chapters, the experimentally observed modes will be identified with the most unstable modes in the model. This concept has already been applied to the dust-density wave propagating through a cloud of micron-sized particles under microgravity conditions [125, 126].

The experimental finding was that the wave propagates aligned with the ion flow in the plasma bulk, but as it approaches the sheath, it changes its direction to almost perpendicular propagation. The bending of the wave fronts was directly observed [126]. The new wave mode was named “obliquely propagating dust-density wave” (OPDDW). Its existence was also predicted for the magnetized plasma [89, 163].

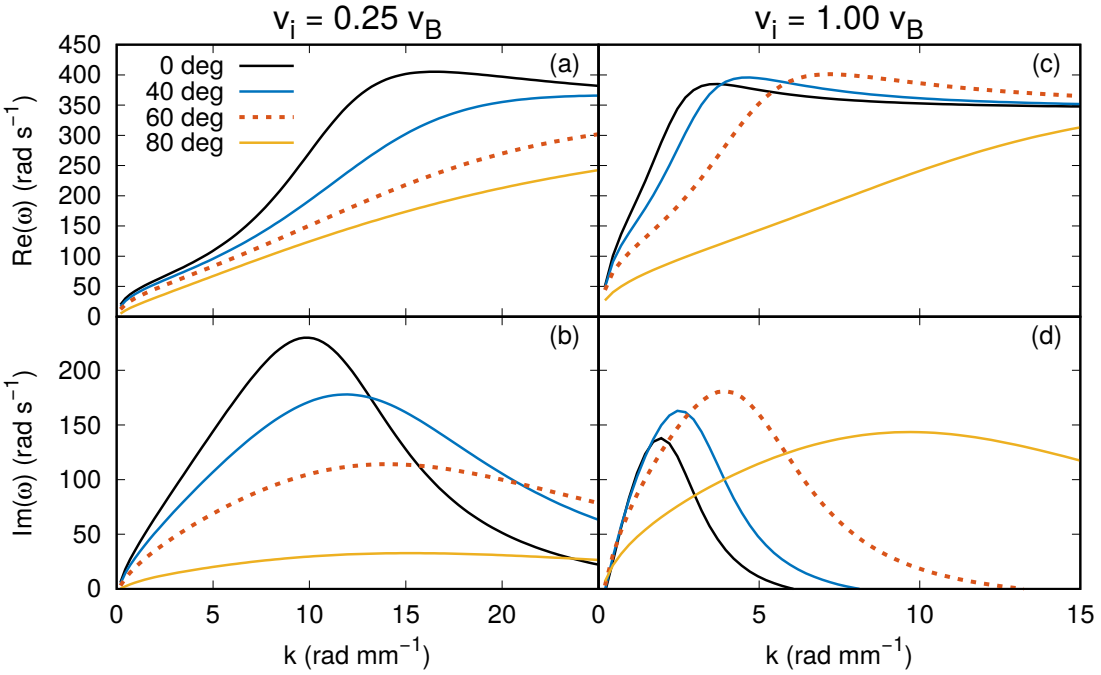

Fig. 3.2: Dispersion relations for the microdusty situation in the left column of Tab. 2.1 calculated with the hybrid model. The angle between ion flow and wave vector is varied (different colors). The dispersions are calculated for (a, b) a flow velocity of 25 % and (c, d) a flow velocity of 100 % of the BOHM velocity. The upper panel (a, c) denotes the real part and the lower panel (b, d) denotes the imaginary part or growth rate of the wave.

The concept of an oblique mode can be introduced by setting an angle between $\mathbf{k}$ and $\mathbf{v}_\mathrm{i}$. The dot product of $\mathbf{k}$ and $\mathbf{v}_\mathrm{i}$, which is included in the dispersion relation, produces the term $kv_\mathrm{i}\cos(\vartheta)$. This means that the complete dispersion relation depends on ϑ, the angle between $\mathbf{k}$ and $\mathbf{v}_\mathrm{i}$. In Fig. 3.2, dispersion relations for the microdusty configuration that was introduced in the left column of Tab. 2.1 are shown for different values of ϑ.
If the ion flow velocity is low as in Fig. 3.2 (a, b), the dispersion of the wave is influenced by ϑ: For higher values of ϑ, the dispersion curve gets shifted towards larger wave numbers. The most unstable mode is realized for $\vartheta = 0°$, since $\mathrm{Im}(\omega)$ decreases at larger ϑ.
A different behavior can be found at larger ion drift velocity, as depicted in Fig. 3.2 (c, d). The most unstable mode is found for $\vartheta = 60°$ and has a much larger growth rate than for $\vartheta = 0°$. This is why – from the model of the system – it can be expected that oblique propagation towards the ion flow will be favored over parallel propagation of the wave. In this thesis, the dust-density wave will only be analyzed in the midplane of the plasma bulk. Oblique propagation of the wave can be excluded due to the symmetry in this location of the plasma. The ion flow is slow so that the oblique mode would not be expected to appear.
The good agreement between model and experiment concerning the dominance of the most unstable mode for the example of oblique wave propagation helps to evaluate the significance of the model equations introduced above. A change in the properties of the

most unstable mode that emerges from the local plasma conditions is directly imposed on the wave during its propagation through the inhomogeneous dusty plasma. A change in the ion flow velocity leads to a variation of ϑ. This is the foundation for the applicability of the model for the experiments presented in the coming chapters. If the wave adapts its parameters to the local conditions, then it allows direct conclusions about the plasma parameters. Therefore, the finding of the oblique mode in the experiment and its locality is of great importance for the applicability of the dust-density wave as a plasma diagnostic technique.

The observed dominance of the most unstable mode in every location of the experiment leads to an interpretation of the equations above: The perturbation analysis in terms of a FOURIER plane wave ansatz describes a spatially unlimited homogeneous plasma. In the experiment, there are strong gradients of the plasma parameters so that they change drastically on only a few wavelengths. The complex plasma on the propagation path of the wave can be interpreted as a chain of small plasma cells. In each of the cells the unstable mode is comparable to the most unstable mode from the infinite model system and it prevails against the incoming wave mode. In this way the plasma on the propagation path forces the incoming wave to overtake the properties of its most unstable mode.

This finding has some similarity to the WKB approximation in quantum mechanics. One assumes that the parameters, e.g., the potential in the case of WKB, change slowly so that the resulting wave can be determined without the direct inclusion of gradients in the model. Instead, the system is supposed to have constant parameters on a length scale, which is large enough that the solution does not collapse. In the case of the propagating DDW, the oblique mode has proven that the interpretation of the system as a sequence of complex plasma cells, in which the parameters are assumed to be constant, is quite successful.

3.9 Sensitivity of the DDW to the System Parameters

From the preceding section it can be seen that the propagation direction of the dust-density wave is sensitive to the ion flow velocity in a microdusty plasma.

Now, the sensitivity of the wave to the plasma parameters in the nanodusty situation will be considered. An example calculation of the dispersion relation for different values of the ion density can be found in Fig. 3.3. It is found that the dispersions are very different in the three considered cases.

Since the experiments are performed in a regime with very high dust number density, the dust charge depends directly on the ion density: $Z_\mathrm{d} = n_\mathrm{i}/n_\mathrm{d}$. Hence, a modification of the ion density leads not only to a variation of the ion plasma frequency, but also to a variation of the dust plasma frequency. The frequency of the wave is completely ruled by the dust plasma frequency since in the frame of the moving ions, the wave fronts are "frozen" or moving much slower than the ions drift. Therefore, the wave frequency is ir-

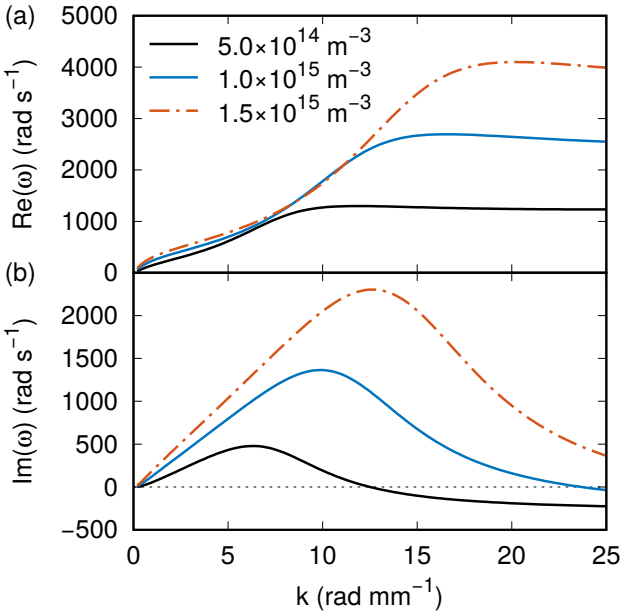

Fig. 3.3: Dispersion relations for the nanodusty situation in the right column of Tab. 2.1 at different values of the ion density. (a) Real and (b) imaginary part of ω. Here, not only the ion density is varied, but the dust charge is calculated for the different ion densities self-consistently using the LIM HAVNES model. Note that the frequencies are almost one order of magnitude larger than those in Fig. 3.2, which belong to the microdusty situation, while the excited wave numbers are almost equal.

relevant to the ions and is only determined by the dust charge, dust number density, and the dust mass. For very different dust parameters, e.g., a nanodusty versus a microdusty plasma, one yields very different frequencies. If the dust plasma frequency increases, then the complete dispersion is shifted to larger frequencies.

Another aspect of the increased ion density is that the ion plasma frequency gets larger. The DDW is unstable if the DOPPLER shift frequency of the flowing ions is close to the ion plasma frequency. This condition is independent from the dust parameters. Since the flow velocity is kept constant in Fig. 3.3, an increased ion plasma frequency leads to a larger wave number of the most unstable mode.

Both effects are visualized in Fig. 3.3. For the larger ion densities, the dispersion curve shifts to higher frequencies and to higher wave numbers. The same applies for the respective growth rates. The most unstable mode shifts to larger wave numbers.

Comparing Fig. 3.3, which shows the dispersion relations for the nanodusty situation, with the dispersion curves in Fig. 3.2 for the microdusty situation, two statements can be made: The frequencies differ by almost one order of magnitude while the excited wave numbers are in the same range. An example is the blue curve in Fig. 3.3 and the black curve in Fig. 3.2 (b): The wave number from the most unstable mode is almost identical. The microdusty and the nanodusty situation differ only by the dust component.

The influence of the ion flow velocity can now easily be found and was already included in Fig. 3.2. At larger ion flow velocity, the most unstable mode appears at much lower wave numbers. The frequency of the most unstable mode is almost conserved.

Summarizing these thoughts, it is found that the ion flow velocity is mainly influencing the wave number, while the dust plasma frequency determines the wave frequency. Additionally, in the nanodusty situation the ion density and the dust plasma frequency are

connected by the HAVNES effect. From the considered example calculations, it becomes clear that the DDW is very sensitive to the ion flow velocity, the ion density, and the dust plasma frequency. Further, it can be concluded that the dust-density wave is an excellent indicator for these parameters.

4 Experimental Setup

Experiments have been performed using an rf plasma in a stainless steel chamber, which has a cylindrical volume with a height of 20 cm and a diameter of 15 cm. Using an admixture of a reactive gas, plasma-chemical reactions lead to the formation of dust particles. By suspending the reactive admixture, a pristine dusty plasma is provided whose dust particles stay constant in size. The plasma chamber resides in the DUSTWHEEL, a magnetic solenoid. By variation of the neutral gas flow through the chamber, the neutral pressure can be set in a wide range. Using optical diagnostics positioned around the plasma chamber to image the propagation of density waves and the optical properties of the dust particles, the system can be fully probed.
In this chapter, a basic experimental outline is given. Each diagnostic will be explained in detail.

4.1 Plasma Source

The plasma chamber is a stainless steel vessel, in which electrodes are inserted from top and bottom. The electrodes have a diameter of 58 (*setup A*) or 50 mm (*setup B*)[1] and have a radial FARADAY shield, which is grounded. The electrodes are electrically contacted through a grounded tube. The inside of the tube is at atmospheric pressure to prevent parasitic discharges. The plasma chamber has four observation windows. At the top and at the bottom, symmetrically around the electrodes are the inlet of gas and the connection to the pumping system, see Fig. 4.1 (a). Differing from this figure, the gas inlet was installed via two flanges in the upper chamber cap in *setup A*.[2]
The electrodes are placed in parallel and driven in push-pull mode. The plasma is generated using a DRESSLER LPGC 133 at 13.56 MHz and a PALSTAR AT4K matching "T" network. The rf generator output is connected to a balun via a matching network (MB).[3] The matching network reduces the reflected power coming back to the generator to zero. The balun is a 1 : 1 transformer used to drive electrodes in push-pull mode. The secondary

[1] The two different setups that were used for the conduction of experiments are shown in Fig. 4.5 and Fig. 4.11 and will be reviewed below. The electrode radius was reduced in *setup B* to enhance the visibility of the edge regions of the dust cloud through the windows.
[2] See Fig. 1 in Ref. [A.1].
[3] MB abbreviates matchbox.

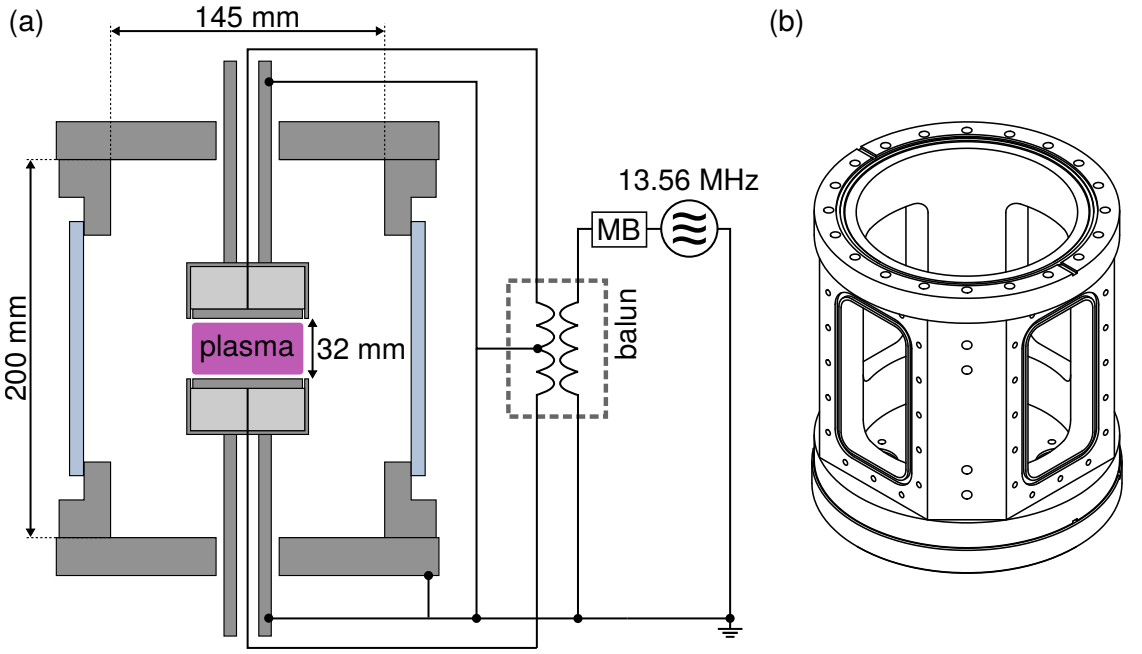

Fig. 4.1: (a) Side view section sketch through the plasma chamber and electrodes. Windows are displayed in blue. Neutral gas flow goes from top to bottom through the chamber entering symmetrically around the electrode pipe. Grounding of the chamber, the electrode shield, and the center tap of the secondary coil of the balun is realized with copper bands. The rf signal is provided to the electrodes via a matching network (MB). (b) 3D visualization of the plasma chamber without electrodes, windows, and the upper cap.

coil of the transformer has a center tap, which was grounded in all experiments. This means that the signal at both electrodes is symmetric w.r.t. ground. Typical forwarded rf power from the generator was 8 (*setup A*) or 12 W (*setup B*).

The gas flow is depicted in Fig. 4.2. A vacuum is produced with a turbomolecular pump and a rotary vane pump providing the fore-vacuum. It can also be used directly bypassing the turbomolecular pump. Bypassing becomes necessary when the reactive gas acetylene is used because its compression can cause explosions. The rotary vane pump prevents this behavior with its gas ballast function. The pumping power is much lower for the rotary vane pump resulting in a higher residence time for the acetylene, which is supportive for dust production. With a throttle valve the pumping power of the turbomolecular pump can be reduced in very small steps. Therefore, it is possible to switch between the turbomolecular and rotary vane pump without changing the pumping power or the pressure. Afterwards, by slowly opening the throttle valve, the pressure can be set to much lower values without disturbing the dusty plasma. In this configuration, a reactive plasma can be realized securely and low pressure can be reached for the pristine argon plasma.

The two pumping modes can be set one after another because acetylene is only used in the beginning to grow dust particles to a certain size. If this size is reached, the acetylene flow is stopped, and there is no need for a gas ballast any more. Base pressure of the

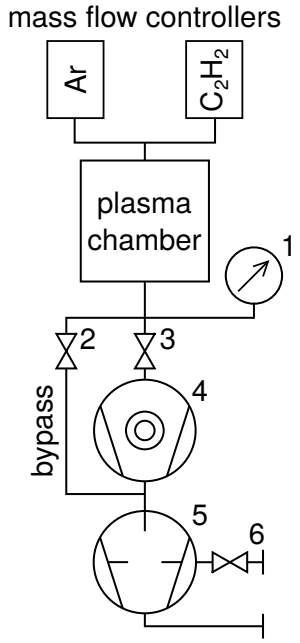

Fig. 4.2: Gas flow concept. Argon and acetylene are supplied via two MKS mass flow controllers. The pressure is measured with a PFEIFFER PKR-251 (1). The valves (2,3) (dis-)connect the chamber and the pumps. (2) is a spin valve and (3) is an electronic throttle valve of the type MKS T3Bi. The latter can be opened continuously between 0 and 100 %. The gas is pumped with a turbomolecular pump (4), which is a PFEIFFER TSH 261, and a rotary vane pump (5) from EDWARDS of the type RV5F. The latter has a gas ballast valve (6). If valve (2) is opened and (3) closed, the turbomolecular pump is bypassed. In the opposite case, the chamber is evacuated to its base pressure.

system is 3×10^{-3} Pa. The gas flow is controlled using two MKS mass flow controller, one for argon, one for acetylene. Both gases are mixed before the chamber inlet, i.e., the input gas composition can be altered dynamically during the conduction of experiments.

4.2 Dust Particle Formation

Acetylene (C_2H_2) is used as a precursor gas for synthesis of dust particles. One industrial application of acetylene plasmas is to generate diamond-like thin films. These can be used for tribological purposes. They can be very hard and are transparent in the IR [62, 164, 165]. The plasma-polymerised dust and its IR spectrum can serve as a model system for interstellar dust [166]. The Cassini-Huygens mass spectrometer has revealed that acetylene and methane are present in the atmosphere of Saturn's moon Titan [167].
In the conducted experiments, an argon plasma is used to provide electrons that have activation energy for chemical reactions and serve as partners in these reactions with acetylene. There are too many primary reactions to list them all here. An overview can be found in Ref. [168]. After the primary reactions, there are reaction pathways that lead up to very large molecules. This process is called polymerisation. There are three main pathways:

- ionization
  $C_2H_2 + e^- \longrightarrow {C_2H_2}^+ + 2\,e^-$
  ${C_2H_2}^+ + C_2H_2 \longrightarrow {C_4H_2}^+ + H_2$
  ...

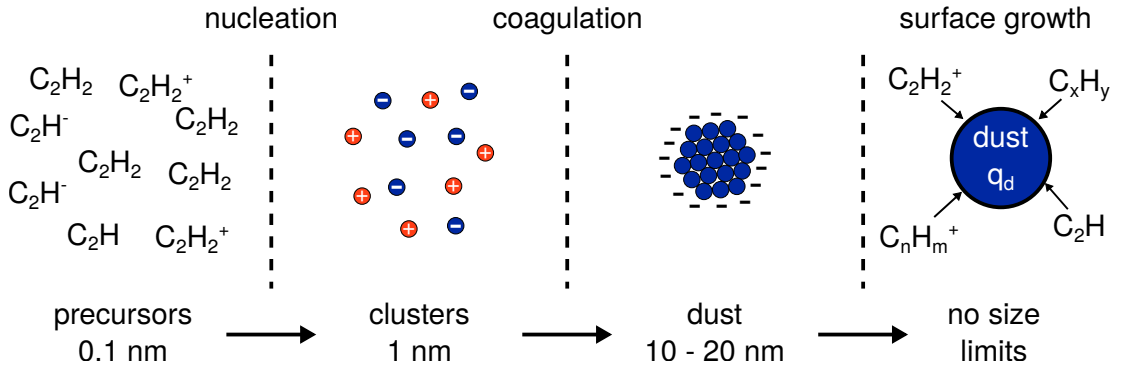

Fig. 4.3: Dust particle formation as a three-step process according to BOUCHOULE and BOUFENDI [172]. The visualization idea goes back to KOVAČEVIĆ *et al.* [173]. The chemical notation of the dust material is *a*-C:H, amorphous hydrogenated carbon.

- attachment
  $C_2H_2 + e^- \longrightarrow C_2H^- + H$
  $C_{2n}H^- + C_2H_2 \longrightarrow C_{2n+2}H^- + H_2$

- dissociation
  $C_2H_2 + e^- \longrightarrow C_2H + e^- + H$
  $C_{2n}H_2 + C_2H \longrightarrow C_{2n+2}H_2 + H$.

Such molecules can be found with mass spectrometric methods in acetylene plasmas [169, 170]. In the plasma, the molecules behave w.r.t. their charge. Neutrals have no spatial preference, they are equally distributed in the chamber volume whereas ions, positive and negative, are influenced by the ambipolar plasma potential. Negative ions are pulled in the discharge, positive ions are repelled. Negative ions are confined into the plasma bulk and supposed to be the dust particle precursors. Experiments with pulsed acetylene plasmas showed that dust formation can be suppressed at low pulse frequencies, probably due to the loss of negative ions in the plasma-off time [171].
The transition from chemical reactions to dust formation is modeled as a three-step process [172] and is visualized in Fig. 4.3. If a sufficient density of clustered molecules with fluctuating charges is present in the plasma, coagulation appears suddenly. Although coagulation can also be observed in neutral gases, the alternating charges of the clusters are supposed to enhance the coagulation due to the mutual attraction of the clusters [174]. They have a size of up to 10 nm and have not been found to be spherical [172].[4] The coagulation phase ends abruptly when the aggregates are large enough to attain a net negative charge from the plasma that prevents further collision events. During the coagulation step, the dust particle density decreases by more than an order of magnitude [172,

[4]This finding corresponds to silane plasmas. When two dust particles merge, this could only lead to spherical shape if the colliding particles both have the shape of hemispheres, regardless of the chemical composition of the particles. Therefore, it can be expected that the particles are not spehrical right after the coagulation phase.

175]. The resulting dust particles grow further as they attract positive ions. Neutrals and radicals from the precursor gas can stick to their surface. This process is called accretion or surface growth. In the accretion step, the particles are spherical [B.2, 172], monodisperse [176], and their size increases linearly with time [177] since the mass flow to the particle is proportional to its surface and the density of sticking objects n [178]:

$$\frac{\mathrm{d}m}{\mathrm{d}t} = \rho\frac{\mathrm{d}V}{\mathrm{d}t} = 4\pi r^2\rho\frac{\mathrm{d}r}{\mathrm{d}t} \propto nr^2 \tag{4.1}$$

$$\Rightarrow \frac{\mathrm{d}r}{\mathrm{d}t} \propto n = \text{const}\,. \tag{4.2}$$

This argument is restricted to neutrals and radicals. For ions, the situation is more difficult because they are repelled or attracted w.r.t. the dust charge, which changes during the process. The maximum particle size depends on the confinement strength provided by the plasma. For the specific experiments of this thesis, the upper particle radius varied between 400 nm and more than a micron. If gravity and ion drag exceed the confining forces, the particles are removed from the plasma. In principle, micron sized particles can be generated by increasing the confinement, e.g., by placing a metallic ring on the electrode, which produces a particle trap in the plasma sheath [179].
Surface growth can be stopped if no more sticking neutrals or positive ions are available. This is realized by stopping the acetylene supply to the chamber. It takes a short time of a few seconds to refill the complete chamber volume with argon. This can be calculated as the ratio of chamber volume to volume flow rate: In the experiments with *setup A*, the mass flow controller was always set to a flow of $s = 8\,\mathrm{sccm}$ at a pressure of $p_\mathrm{n} = 24\,\mathrm{Pa}$ during the surface growth of dust particles. With a chamber volume of about $V = 3.5 \times 10^{-3}\,\mathrm{m}^3$, this results in a lifetime of neutrals in the chamber τ_n:

$$s' = s \cdot \frac{p_\mathrm{S}}{p_\mathrm{n}} \cdot \frac{T}{T_\mathrm{S}} \approx 6.2 \times 10^{-4}\,\mathrm{m}^3\,\mathrm{s}^{-1}\,, \qquad \tau_\mathrm{n} = V/s' \approx 6\,\mathrm{s}\,. \tag{4.3}$$

The index S denotes standard conditions ($p_\mathrm{S} = 101{,}325\,\mathrm{Pa}$, $T_\mathrm{S} = 273.15\,\mathrm{K}$). It takes the system six seconds to renew the neutral gas volume. The actual time for this might be slightly larger because the window openings and the supply line enlarge the effective volume, but not significantly. Remaining positive ions are then pushed out of the plasma bulk by the ambipolar electric field. Removal of the negative ion species in the plasma is a requirement for the analysis of density waves in the subsequent chapters because every additional plasma species would alter the wave dispersion relation. Therefore, the experiments are aimed at generating a pristine dusty argon plasma without any carbon ion species. The main loss channel for negative ions in the plasma is the ion-ion mutual neutralization reaction for which an approximative rate coefficient formula is given in Refs. [180, 181]:

$$k_N = 5.34 \times 10^{-13}\,\mathrm{m}^3\,\mathrm{s}^{-1} \cdot (EA)^{-0.4} \cdot \mu^{-0.5} \cdot \left(\frac{T_\mathrm{gas}}{300}\right)^{-0.5} \tag{4.4}$$

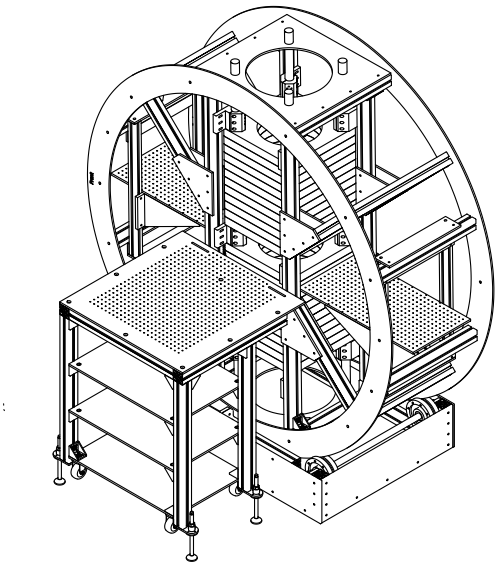

Fig. 4.4: DUSTWHEEL with optical breadboards to the front and to the sides. The plasma chamber can be inserted into the central bore of the coils. The gap between the two groups of copper coils is visible at the height of the optical breadboards. The wheel has an outer diameter of 2 m.

with the electron affinity EA of the anion in eV, the reduced mass of the anion-cation pair μ in atomic mass units, and the temperature T_{gas} in KELVIN. The negative ion with highest density in acetylene plasmas is C_2H^-. Its electron affinity is 2.9 eV [182]. The time constant for the depletion of C_2H^- via $C_2H^- + Ar^+ \longrightarrow C_2H + Ar$ with an Ar^+ density of $10^{15}\,\mathrm{m}^{-3}$ is roughly

$$\tau_{\mathrm{i}} = \frac{1}{k_N n_{\mathrm{i}}} \approx 11.2\,\mathrm{ms}\,. \tag{4.5}$$

This is much smaller than the lifetime of neutrals in the chamber ($\tau_{\mathrm{i}} \ll \tau_{\mathrm{n}}$). It can be assumed that negative ions – not just C_2H^- – are depleted as soon as the gas has been completely renewed. This means that it is possible to change between a chemically reactive and a non-reactive plasma within just a few seconds. Additionally, the growth of dust particles can be stopped in order to have constant conditions for observation and time-consuming diagnostics.

4.3 DUSTWHEEL – A Tiltable Magnet

The complete experiment is placed inside the DUSTWHEEL, which is a water-cooled copper-coil magnet, depicted in Fig. 4.4. Before this work with nanodust was started, it had been used for experiments with long magnetized plasma columns to study the effect of negative ions on drift waves [183, 184].

DUSTWHEEL consists of 24 water-cooled coils, which are grouped in two sets of each 12 coils. The two groups are separated by a gap of 10.5 cm. Inside of the coils, there is a central bore of 30 cm diameter. The plasma chamber can be placed there using a crane so that the chamber windows are directly accessible in the observation gap between the coils. In this way, DUSTWHEEL provides a good environment for observation of dynamics in dusty plasmas.

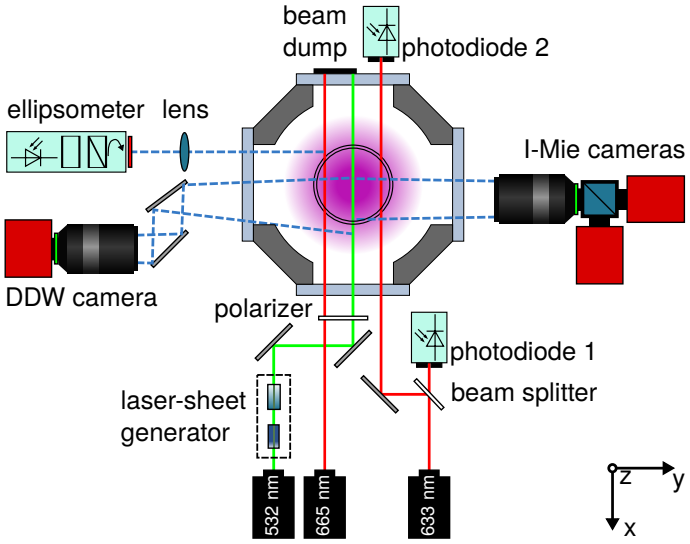

Fig. 4.5: Top view sketch of the optical diagnostics in *setup A*. Each diagnostic is operated at its own wavelength. A linearly polarized vertical green laser line illuminates the central plane of the dust cloud. Density wave propagation is observed using the Bonito CL400-B (DDW camera) whereas the q parameter distribution inside the dust cloud is examined with the I-Mie cameras. Optical depth τ is measured with photodiodes before and after a red (He-Ne) laser beam has passed the cloud. This laser enters the system at a distance of 25 mm from the central vertical axis. A second red laser is sent through the polarizer and the polarization state of the scattered light is measured by an ellipsometer. The cameras and the ellipsometer are protected with interference filters for their respective laser wavelength. [A.3]

The wheel has an outer diameter of 2 m and a width of 0.65 m. To the left and to the right of the magnet, there is an optical breadboard inserted into the wheel, which allows to install optical diagnostics, even with a multitude of components like mirrors, cameras, lasers, lenses, and so on. On the front of DUSTWHEEL there is an additional table with a third big optical breadboard. DUSTWHEEL is placed on a roller block to tilt the complete experiment including the chamber. The experiments of KNIST *et al.* [183] have been conducted in horizontal orientation whereas all experiments presented here have been conducted in vertical orientation.
The maximum power consumption of DUSTWHEEL is $500\,\mathrm{A} \times 700\,\mathrm{V} = 350\,\mathrm{kW}$, which results in a maximum magnetic induction of 0.5 T in the original setup of the device. Due to a limited pressure in the water supply, the maximum induction in the presented work was 0.4 T. Within the observation gap, the magnetic induction is homogeneous.

4.4 Optical Diagnostics

Two slightly differing optical setups have been used, which are referred to as *setup A* and *setup B*. Both setups consist of diagnostics to follow the DDW dynamics with digital cameras, determine the dust particle size by polarization measurements of scattered laser light and the dust particle density by extinction measurements. All three objectives can be realized with imaging techniques. Due to the limited access to the experiment provided

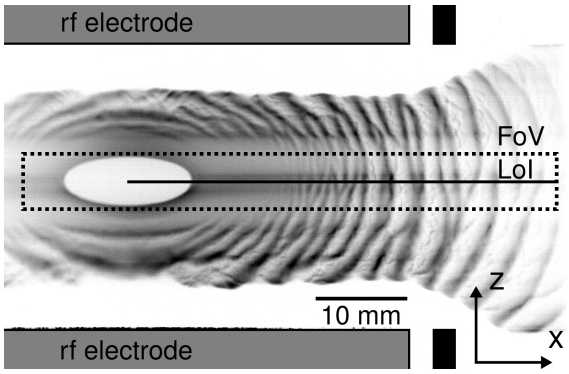

Fig. 4.6: Inverted image of the DDWs with sketched electrodes in gray and FARADAY shield in black. A dashed rectangle marks the field of view (FoV) and a straight line marks the line of interest (LoI), from which data are analyzed. [A.2]

by the chamber windows, not all of these techniques can be applied at the same time. A well-considered selection has to be made. The discussion starts with *setup A* as in Fig. 4.5.

4.4.1 Video Recordings of Dust-Density Waves

The key diagnostic is the measurement of DDWs. The central vertical plane of the dust cloud is illuminated with a laser sheet. Therefore, a 532 nm laser spot is directed on a POWELL lens, which is located in the focal point of a cylinder lens.[5] The POWELL lens serves as a laser-line generator. The laser line is collimated by the cylinder lens. It is directed over two mirrors into the dust cloud. A fast camera, the AVT Bonito CL400-B in conjunction with a ZEISS Makroplanar T*2/100 mm, is used to capture DDW propagation in the illuminated vertical sheet with a reproduction scale of 5.7 : 1 (*setup A*) or 5.2 : 1 (*setup B*). The frame rate was set to 2,000 fps at an exposure time of 0.48 ms. This camera system will be referenced as the DDW camera. In *setup A*, a 200 mW laser was used, which was later replaced by a 1,000 mW laser in *setup B* to account for the short exposure time. In *setup A*, the laser line is also used for a spatially-resolved polarization measurement. Therefore, a polarizer is inserted right before the chamber window.
The camera settings lead to a large output rate of video data. Even with the Camera Link interface it is not possible to transmit the complete image of the dust cloud at the chosen settings. Therefore, only a small field of view (FoV) is recorded, see Fig. 4.6. The DDW properties will be examined along the line of interest (LoI).

4.4.2 Extinction Measurements with a Laser Spot

Scattering and absorption of light by spherical particles leads to a decrease of the transmitted laser light [185]. The ratio of transmitted and incoming intensity of light is given by the BEER-LAMBERT law:

$$I/I_0 = \exp\left(-\int_{-\infty}^{\infty} Q_{\text{ext}}\pi a^2 n_{\text{d}}\,\mathrm{d}x\right) \tag{4.6}$$

[5] See the two objects in the dashed rectangle in Fig. 4.5.

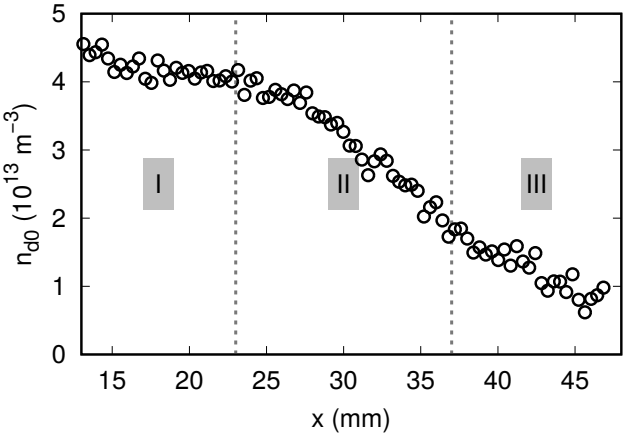

Fig. 4.7: Dust density profile obtained from the medium intensity of 1,024 images taken by the DDW camera. Calibration to absolute values of the density is performed using the measurement of the optical depth τ. Horizontal axis is referenced to the radial center of the plasma chamber. The profile is taken along the LoI defined in Fig. 4.6. The sectioning in three regions will be discussed in the next chapter. [A.3]

with Q_{ext} being the extinction efficiency, which depends on the particle size and the refractive index. The extinction efficiency is the ratio of effective to geometric scattering cross section [185]. The integral in the exponent is called optical depth $\tau = -\log(I/I_0)$. Its measurement allows to determine a medium dust density if particle radius and refractive index are known.

The incident and transmitted intensities I_0, I are measured with two photodiodes because the laser intensity is not temporally constant. The Texas Instruments OPT101-type photodiode was used for this purpose. To calibrate the photodiodes, the intensity ratio without the presence of a dust cloud was measured before dust operation.

If the particle cloud is assumed to be optically thin and monodisperse, then the averaged (oscillation-free) profile of scattered light, visible with the DDW camera, is the dust density profile in arbitrary units. The calibration factor can be determined by measuring τ and calculating the calibration factor with Eq. (4.6). Therefore, the zero-dimensional extinction measurement can be used together with an image of the dust cloud to calculate a one-dimensional dust density profile. Results are shown in Fig. 4.7.

4.4.3 Rotating Compensator Ellipsometer

Knowledge about the optical particle properties is indispensable for the work with in-situ grown dust particles. A very important prerequisite of the analysis of DDWs is the dust particle size. There have been preceding works by H. KETELSEN [186], F. GREINER [176], and S. GROTH [B.2] that deal with the in-situ size diagnostic of growing dust particles. These methods have been used extensively here because the particle size is necessary for the calculation of the particle mass, which influences the dust plasma frequency and the size is also an input to calculate the dust-neutral friction rate. Finally, it is an input parameter for the charging theory presented before. Here, the size of the dust particles is indirectly determined by analysis of the polarization state of scattered laser light. In the experiments, the size parameter $x = 2\pi a/\lambda$ is of the order of unity. The scattering of the polarized light can be described with the MIE theory.

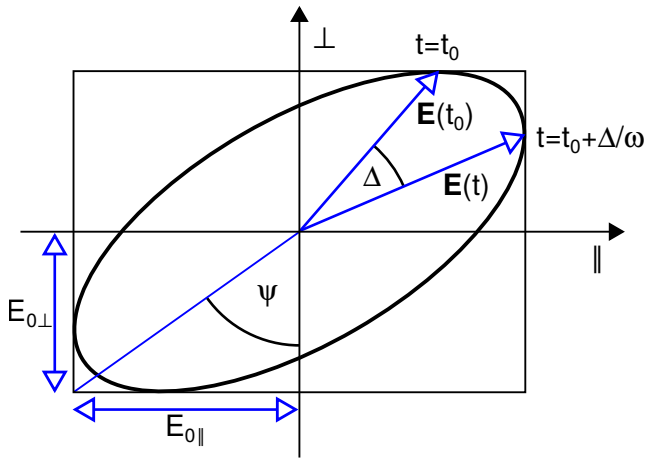

Fig. 4.8: Electric wave vector **E** for elliptically-polarized light. The ellipse can be described with the ellipsometric angles Ψ and Δ. Ψ denotes the amplitude ratio of the oscillation in parallel and perpendicular direction, $E_{0\parallel}$ and $E_{0\perp}$: $\Psi = \arctan(E_{0\parallel}/E_{0\perp})$. Δ is the phase shift between the EM oscillation in parallel and perpendicular direction.

The polarization of light describes preferred oscillation directions of the electrostatic vector of an electromagnetic (EM) wave. The general case of polarization is elliptically polarized light where the electric field vector runs along the points on an ellipse, see Fig. 4.8. The polarization state of light can be described with the STOKES formalism. Light intensities behind ideal linear polarizers with an angle of 0 ($I_\parallel$), $\pi/2$ ($I_\perp$), $\pi/4$ ($I_{\pi/4}$), $-\pi/4$ ($I_{-\pi/4}$) as well as behind an ideal right-circular (I_R) and left-circular (I_L) polarizers are combined in the STOKES vector whose entries are I, Q, U, and V:

$$\mathbf{S} = \begin{pmatrix} I \\ Q \\ U \\ V \end{pmatrix} = \begin{pmatrix} I_0 \\ I_\parallel - I_\perp \\ I_{\pi/4} - I_{-\pi/4} \\ I_\mathrm{R} - I_\mathrm{L} \end{pmatrix} = I_\mathrm{p} \begin{pmatrix} 1/\mathrm{DOP} \\ -\cos(2\psi) \\ \sin(2\psi)\cos(\Delta) \\ -\sin(2\psi)\sin(\Delta) \end{pmatrix} = I_\mathrm{p} \begin{pmatrix} 1/\mathrm{DOP} \\ q \\ u \\ v \end{pmatrix} . \tag{4.7}$$

These intensities can be related to the ellipsometric angles Δ and Ψ, which are defined in Fig. 4.8. The degree of polarization (DOP) denotes the ratio of polarized light intensity to the full intensity: $\mathrm{DOP} = I_\mathrm{p}/I_0$. Normalization of Q, U, and V to I_p results in the normalized STOKES vector $(1/DOP, q, u, v)^\intercal$. The incident light in the performed experiments is fully polarized with an angle of 45° w.r.t. the horizontal plane. Scattering at single particles does not alter the DOP. The amount of polarized intensity I_p depends on the number density of particles n_d and is therefore not a clear size indicator. From the STOKES vector of the scattered light, Ψ and Δ can be directly connected to the particle size and refractive index. The scattering process as well as any other polarization-changing process can be described by multiplication of a MÜLLER matrix with the STOKES vector. The 16 elements of the 4×4 matrix can be determined for any optical part of a setup. In the case that light passes several optical elements, the STOKES vector $\mathbf{s}_\mathrm{s}$ of the transmitted light follows from consecutive application of all respective MÜLLER matrices on the incident STOKES vector $\mathbf{s}_\mathrm{i}$:

$$\mathbf{s}_\mathrm{s} = M_\mathrm{n} \cdots M_2 \cdot M_1 \cdot \mathbf{s}_\mathrm{i}. \tag{4.8}$$

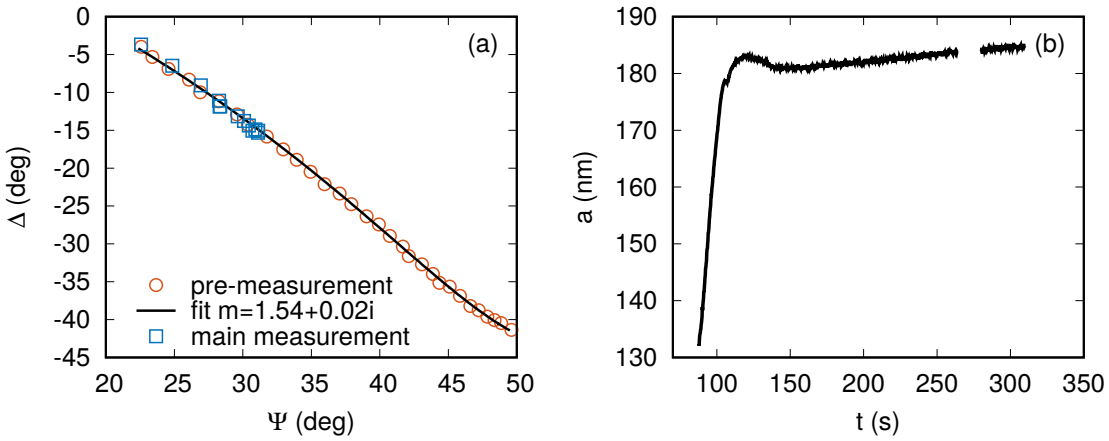

Fig. 4.9: (a) Ellipsometric angles Δ over Ψ for the pre-measurement, fit result (CRAS-MIE), and main measurement. During growth of particles data points propagate from top left to bottom right. Every point on the synthetic curve (black) corresponds to a radius so that data (circles and rectangles) can be mapped to dust particle size. (b) Temporal dust size evolution calculated from CRAS-MIE. After a short time of linear growth, the radius saturates when the acetylene supply to the chamber is closed. The gap in the data results from a manual operation in the setup, during which the laser did not enter the cloud. [A.3]

In both setups a commercial rotating compensator ellipsometer (RCE) from THORLABS, the PAN5710VIS, measures the polarization state of scattered light by the particles. An imaging lens is placed between the chamber and the RCE to collect enough light increasing the signal-to-noise ratio in the ellipsometer. With the RCE data, a time-resolved $\Delta(\Psi)$ evolution is provided. These data can be compared with theoretical values of the MIE function [187], which has been implemented for *MATLAB*^{TM} by MÄTZLER [188]. Internally, this function determines the MÜLLER matrix of the dust for light scattering into a certain direction. It takes as inputs the polarization state of incident light, observation angle, wavelength, refractive index of particle material, and the particle size. It outputs the STOKES vector of the scattered light, for which Ψ and Δ can be calculated. Repeating this call to the MIE function from MÄTZLER with growing particle sizes, a synthetic $\Delta(\Psi)$ data set can be generated. The CRAS-MIE algorithm[6] by S. GROTH [B.2] calculates such synthetic data sets and determines the time resolved radius evolution by appointing every measured $\Delta(\Psi)$ to the point in the data set with the smallest distance in the Ψ-Δ plane. The remaining summed squared distances are the error sum, which is minimized by variation of the refractive index m. This procedure yields the optimal refractive index $m = m_\mathrm{r} + \mathrm{i}m_\mathrm{i}$ and its corresponding temporal size evolution.

When it comes to the application of this method to lab experiments, some refinements had to be made to increase the sensitivity of the method. First, the error in the refractive index gets smaller if a larger part of the particle growth history over time is known. For the study of dust clouds with DDWs, small particles were favored because they are not as much affected by gravity compared with larger particles. But if the growth of the

[6] CRAS-MIE abbreviates **C**onstant **R**efractive Index but **A**rbitrary **S**ize using **MIE** theory.

particles was stopped too early, the obtained data might not allow to determine a valid refractive index. To resolve this conflict, the reproducibility of the particle formation process is utilized. A pre-measurement with a longer growth phase is introduced, for which the refractive index is determined. The plasma is turned off, the cloud vanishes from the chamber, and the plasma is turned on again. Now, the main measurement starts with the growth of new particles. This time, the particle growth is stopped early enough to obtain small particles. Their refractive index is already known with high accuracy from the pre-measurement. With this knowledge, the size evolution can be determined directly without a prior minimization of an error sum. This method is demonstrated in Fig. 4.9 for a measurement run, which will be discussed in the next chapter. Fig. 4.9 (b) shows a radius development, which is typical for the chosen experimental situation. The dust particles grow linearly in the initial phase of the experiment. Then, after closing the acetylene supply, the radius saturates to a value of 183 nm. At this point, the extinction efficiency from Eq. (4.6) equals $Q_{\text{ext}} = 1.54$.

The application of CRAS-MIE requires two assumptions. First, the model only provides the scattering process for a single spherical particle. In the experiment, a laser is sent into a dust cloud with billions of particles. The signal in the sensor is a sum of the scattered photons from many particles. This is not an issue as long as photons do not scatter twice or more times before they reach the sensor. Second, the growth process is assumed to increase the particle size while keeping the refractive index constant. Advanced effects like core-shell structures of the particles, particle size distribution functions or a distribution of particle shapes cannot be handled by the method. However, the considered system is demixing [67, 114, 115, 189], i.e., particles of different sizes should separate into different shells or droplets. The influence of a distribution function can be neglected as long as the observed volume is not too large. The particle shape has been studied with SEM [B.2] and found to be spherical. The assumption of single scattering can be violated if the optical depth becomes too large. In that case, multiple scattering events start to change the measurement results and have to be taken into account. Radiative transport simulations of the used system with MONTE-CARLO-type algorithms have been performed recently [190]. There, larger particles have been grown on purpose to provoke a situation with significant multiple scattering effects. Direct comparison of radiative transfer in theory and experiment is a promising field for application of codes originally devised for astrophysical situations where the optical depth can be much larger than unity. Additionally, these codes could help extend CRAS-MIE to optically thick particle clouds [191].

4.4.4 Imaging MIE

Because the RCE consists of a photodiode behind a rotating quarter wave plate and a linear polarizer, the analysis of these data yields the particle size only in one observation spot. The assumption of a particle cloud, which is homogeneous in particle size

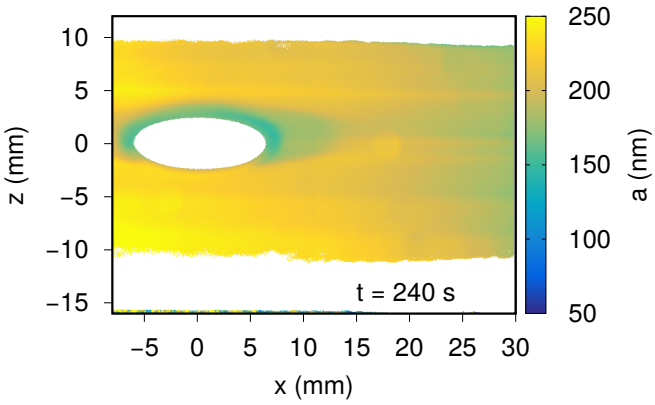

Fig. 4.10: Resulting size map of the dust particles at $t = 240\,\mathrm{s}$. For every pixel, the calculated q' (see Eq. (4.9)) is mapped to a particle size with a function obtained from the RCE and CRAS-MIE data. The image is taken from the same measurement that led to the data in Fig. 4.9. [A.3]

(monodisperse), needs to be verified, at least for a single run of the experiment. For this purpose, the imaging MIE device, introduced by GREINER *et al.* [176], is included in *setup A* (Fig. 4.5).

This technique measures the amount of parallel and perpendicular polarized light, $I_{\parallel}$ and $I_{\perp}$. These quantities are determined by splitting the images from a CANON lens with a polarizing cube and taking these images with two Prosilica GE680 cameras. Finally, the parameter q' is calculated:

$$q' = \frac{I_{\parallel} - I_{\perp}}{I_{\parallel} + I_{\perp}} \,. \tag{4.9}$$

For fully polarized light, the parameter q' equals the second entry in the STOKES vector. In the measurements, the DOP was roughly 70 %. From the RCE data, q' can be calculated and mapped to the resulting radius curve. The underlying assumption here is that the DOP has a global development, which is independent from the observed location. By applying this mapping function to the I-MIE obtained q' data, a spatially and temporally resolved size map can be computed. Such an image is shown in Fig. 4.10. This shows that the assumption of a monodisperse dust cloud is justified but there is a central shell of distinctively smaller particles surrounding the void. The shell configuration was also found in similar experiments [113, 115, 192].

4.4.5 Comparison of the Setups

For the study of the system without a magnetic field, *setup A* proved to be very effective. Particle size, density, and wave properties could be determined synchronously and allowed to examine the internal structure of the system without intrusive methods.

The biggest disadvantage of *setup A* is that the dust density is determined with a rough approximation: It is assumed that the incoming laser light is not attenuated in the first half of the cloud. The calibration of the scattered light profile to absolute density allows to determine the dust density only along one central line of the system because the incident

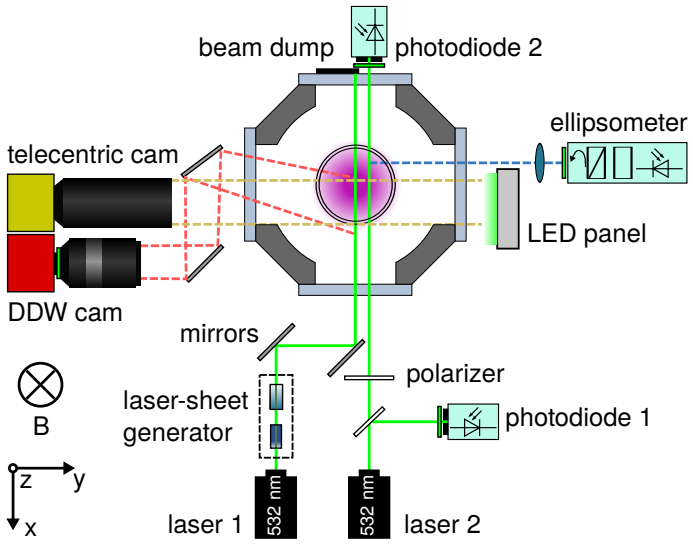

Fig. 4.11: Top view sketch of the optical diagnostics in *setup B*. In comparison with *setup A* in Fig. 4.5 only 532 nm lasers and a green LED panel are used. The ellipsometer was switched to the other side and a telecentric lens camera system was added to take extinction images of the dust cloud. © 2018 American Physical Society [A.4]

laser line is not homogeneous. These issues had to be resolved for the study of dusty plasmas in an external magnetic field because the spatial distribution of dust particles changes at different magnetic inductions. Therefore, *setup B* was developed with the aim of providing a 2D density map, see Fig. 4.11. KILLER *et al.* have realized such a system before [B.3, 26, 193]. With an LED illumination panel and a telecentric lens they recorded extinction images of the dust cloud, which appears as a dark shadow in front of the bright LED panel.

The introduction of such a measurement system creates an additional restriction to the MIE technique. All optical properties of the dust material depend on the wavelength. Therefore, the LED panel and the laser used for the MIE scattering measurements must be at the same wavelength. For the illumination panel, it was appreciated to choose green because most camera chips are optimized for the middle of the visible spectrum. Consequently, the red laser used in *setup A* for the laser-light scattering measurements is replaced with a green laser in *setup B*. In contrast to *setup A* where all illumination sources could run synchronously, the use of the same wavelength now demands that every diagnostic can only be used one after another. This restriction is not a strong limitation for the measurement process because the lasers as well as the LED panel can be switched on and off on the millisecond time scale.

4.4.6 Inverse ABEL Transform

Using *setup B*, extinction images as in Fig. 4.12 (a) are available. The dust cloud has a cylindrical symmetry in the magnetized and in the unmagnetized situation. The extinction image originates from a line-of-sight integration through the dust cloud and the

real-space dust-density distribution follows by the inverse transform of this integration. The forward transform is called ABEL transform

$$F(y) = \int_{-\infty}^{\infty} f\left(\sqrt{x^2+y^2}\right)\,\mathrm{d}x = 2\int_{|y|}^{\infty} \frac{f(r)r}{\sqrt{r^2-y^2}}\,\mathrm{d}r \tag{4.10}$$

and the backward transform the inverse ABEL transform

$$f(r) = -\frac{1}{\pi}\int_{r}^{\infty} \frac{\mathrm{d}F}{\mathrm{d}y}(y)\,\frac{\mathrm{d}y}{\sqrt{y^2-r^2}}\,. \tag{4.11}$$

Application of this equation to noisy measurement data will obviously result in large errors as the derivative has to be calculated as well as a fraction of this derivative with infinitely small numbers at $y \longrightarrow r$. KILLER *et al.* used an indirect method by representing $f(r)$ with a cosine series whose coefficients are determined by minimizing the deviation between the modelled $F(y)$ against the measured one [26, 194]. This method, originally devised by PRETZLER [195], tends to oscillatory solutions. In this work, the solution was computed by calculating the derivative of the data with first-order polynomes on small 30-point windows around the current position and inserting the resulting derivative data in Eq. (4.11). Unfortunately, this is still numerically unstable for every position r because the integration starts at $y = r$ where the denominator in the integral is zero. This problem is avoided by a simple coordinate transform of the form $y = \sqrt{t^2+r^2}$. Then, Eq. (4.11) takes the form

$$f(r) = -\frac{1}{\pi}\int_{0}^{\infty} \frac{\mathrm{d}F}{\mathrm{d}y}\left(\sqrt{t^2+r^2}\right)\,\frac{\mathrm{d}t}{\sqrt{t^2+r^2}}\,. \tag{4.12}$$

The derivative at the shifted positions $\sqrt{t^2+r^2}$ is found by linear interpolation. This solution is only unstable for $r \longrightarrow 0$ whereas Eq. (4.11) would be numerically unstable for all values of r.

In the experiment, the ABEL transformed quantity f is the argument of the integral in Eq. (4.6). Therefore, the inverse ABEL transform yields

$$f(r) = Q_{\mathrm{ext}}\pi a^2 n_{\mathrm{d}}\,. \tag{4.13}$$

Note that this equation is valid for every cylindrically symmetric distribution of Q_{ext}, a, and n_{d}. It is not limited to the considered case of a monodisperse dust cloud. As stated above, the extinction efficiency Q_{ext} for the wavelength of the illumination panel has to be known, which is why the illumination laser for MIE scattering needs to have the same wavelength. Otherwise, this equation could not be solved for the dust density n_{d}. Applying this method to experimental data, images like the ones shown in Fig. 4.12 can be obtained.

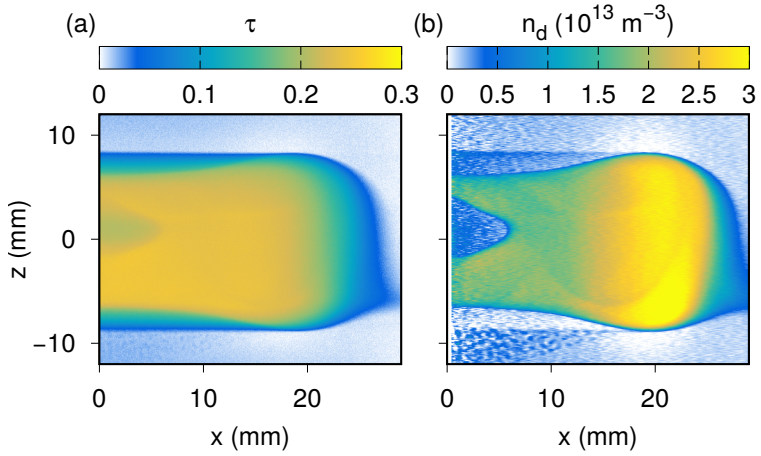

Fig. 4.12: (a) Optical depth τ measured with *setup B*. (b) Dust density calculated with Eq. (4.12). Since the transform is unstable for $r \longrightarrow 0$, the density cannot be obtained at $x = 0\,\mathrm{mm}$. © 2018 American Physical Society [A.4]

Given this extended set of optical diagnostics, it is possible to examine the particle size, the cloud density distribution, and the DDW properties almost synchronously. These are requirements for the comparison of experiment and theory that will be given in the next chapter.

5 Dust-Density Waves as a Diagnostic Tool

The dust-density wave (DDW) can be used in different ways to determine parameters of the plasma and the dust. The core idea is to compare (hydrodynamic) theory as presented in chapter 3 with video recordings of DDWs in the experiment.
In published works, three methods of DDW diagnostics can be identified: The first one uses the phase velocity, which can be obtained by tracking wave fronts in subsequent video frames. For comparison with theory, the plasma parameters are usually known from other plasma diagnostic techniques. Only one parameter, usually the dust charge, is varied in order to align the measured and predicted phase velocity. Thus, the dust charge can be determined [10].
A second method is to control the frequency of the DDW by modulation of the electrode bias voltage or the input power. By variation of ω, the dispersion relation can be measured [120]. Matching with theory can then be achieved by finding the correct system parameters that result in the measured curve [122, 123, 127, 142, 196–199].
In a third method, the naturally-occurring DDW is directly compared to theory. From the hydrodynamic approach a complete solution of ω over k can be derived. The imaginary part of ω, the growth rate, is calculated and its maximum determines the most unstable mode. It is assumed that this mode is the dominant contribution to the wave field and will be observed in the experiment [45, 78, 79, 106, 122]. The parameters in the model are varied to find a solution, for which the most unstable mode is equal to the observed mode.
The last method has several advantages over the others: The naturally-occurring mode can be observed without influencing the plasma. Modulation of the system is a global intervention, which can be avoided. In comparison with the first method, twice as much information is obtained because the most unstable mode is characterized by k and ω whereas the phase velocity yields only the ratio of ω and k. Therefore, the third method will be expanded to an algorithm, the dust-density wave diagnostic (DDW-D). It will be applied and demonstrated with data obtained from the experiment presented in the preceding chapter.

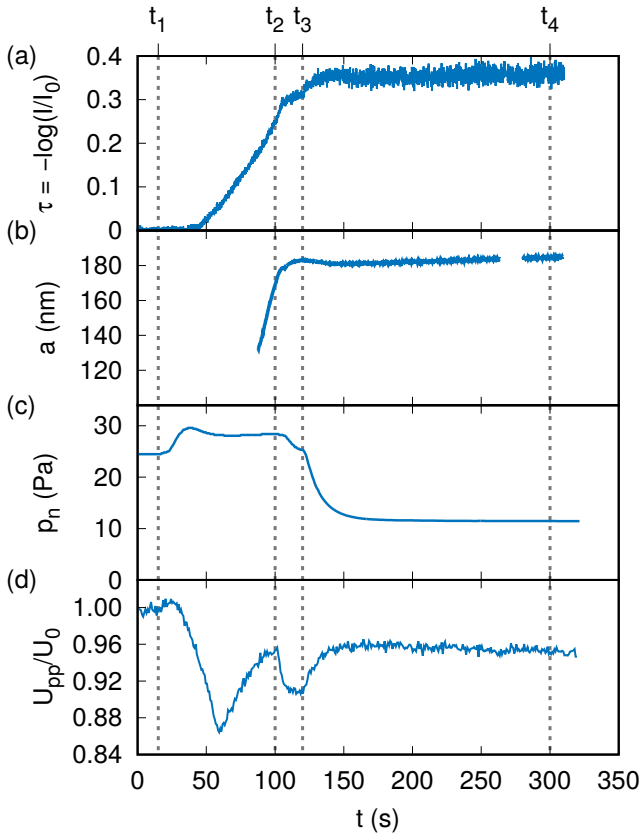

Fig. 5.1: Timing diagram of the experiment. At $t_1 = 15\,\mathrm{s}$ the acetylene flow is opened and closed again at $t_2 = 100\,\mathrm{s}$. After giving the system some time to rearrange, the flow is reduced from 8 to 2 sccm at $t_3 = 120\,\mathrm{s}$. When the pressure has reached a stable value, video recording of the DDW starts at $t_4 = 300\,\mathrm{s}$. (a) Optical depth of the particle cloud measured with the photodiodes and the He-Ne laser. (b) Dust particle size obtained from CRAS-MIE. (c) Pressure measured by a full range gauge. The data between t_1 and t_2 are uncertain because the gauge is gas-type dependent. (d) Relative peak-to-peak voltage measured between the two electrodes. [A.3]

5.1 Experiment Schedule

The experiment described in this chapter was conducted with *setup A*. For the study of DDWs, a distinct schedule was designed. It is discussed w.r.t. Fig. 5.1 where the time stamps t_j are defined. All diagnostics have been initialized at $t = 0$. At this time, a plasma has been present for some minutes at a pressure of $p_\mathrm{n} = 24\,\mathrm{Pa}$ and a forwarded power from the rf generator of 8 W. The gas flow amounts to 8 sccm argon and is bypassed to the rotary vane pump.

In the time before t_1, reference data in the absence of dust has been obtained. Then, acetylene is admixed to the argon gas flow. The flow is kept constant at 8 sccm and acetylene amounts for 20 % of the flow. This initiates the growth of dust particles, which can be observed in all diagnostics depicted in Fig. 5.1. The first indicator for the growth of dust particles is the change in the peak-to-peak voltage [200]. This is also found in the given data depicted in Fig. 5.1 (d).

At t_2 the acetylene flow is shut down so that the dust particle size and the optical depth saturate after some time. At t_3 the gas flow is reduced and the pressure begins to decrease. The optical depth data become noisy after the closure of the acetylene supply (t_2) and even more when reducing the pressure (t_3). This is due to the onset of DDWs, which are not fully averaged out on the line-of-sight of the extinction measurement. Af-

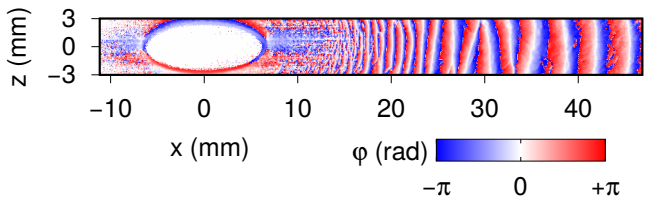

Fig. 5.2: Local phase from the HILBERT transform for a video of the FoV depicted in Fig. 4.6. Note that the HILBERT transform was applied on every pixel independently. The x- and z-axis are centered at the void center. [A.2]

ter some time, all monitored parameters in Fig. 5.1 have stabilized and video recording of the DDW starts at t_4. The following results are based on a recording of 0.512 s duration.

5.2 Characterization of the Wave Field

5.2.1 HILBERT Transform

For the extraction of wave parameters from the videos, the HILBERT transform is used. In the following, the quantity $\tilde{I}(t) = I(t) - \bar{I}$ denotes the average-free fluctuation of the intensity on a camera pixel. The HILBERT transform of this quantity is given by

$$H[\tilde{I}(t)] = \frac{1}{\pi} \int_{-\infty}^{+\infty} \frac{\tilde{I}(\tau)}{t-\tau} \, \mathrm{d}\tau \, . \tag{5.1}$$

The HILBERT transform is a convolution with $(\pi t)^{-1}$. In FOURIER space, the convolution equals a multiplication of the FOURIER transformed multiplicants. The FOURIER representation of $(\pi t)^{-1}$ is given by

$$F\left[(\pi t)^{-1}\right] = \frac{1}{\sqrt{2\pi}} \exp(i\,\pi/2\,\mathrm{sgn}(\omega)) \, . \tag{5.2}$$

This demonstrates the qualitative behavior of the HILBERT transform. It shifts the phasor of any periodic signal by $\pi/2$. Therefore, it can be utilized to construct the analytic signal:

$$A(t) = \tilde{I}(t) + i \cdot H[\tilde{I}(t)] = E(t) \cdot \exp(i \cdot \varphi(t)) \, . \tag{5.3}$$

The polar form of the analytic signal provides the instantaneous amplitude E and the instantaneous phase φ as the absolute value and the argument of the polar form. For any kind of wave, frequency and wave number are defined as:

$$\omega = -\frac{\partial \varphi}{\partial t}, \qquad \mathbf{k} = \nabla \varphi \, . \tag{5.4}$$

Therefore, the local phase of the wave obtained from the analytic signal allows to determine the wave parameters with spatial and temporal resolution.

5.2.2 Frequency and Wave Number

Using *setup A*, the instantaneous phase map obtained for a video taken from the FoV is given in Fig. 5.2. In this example, the video was taken at 2,000 fps and the number of

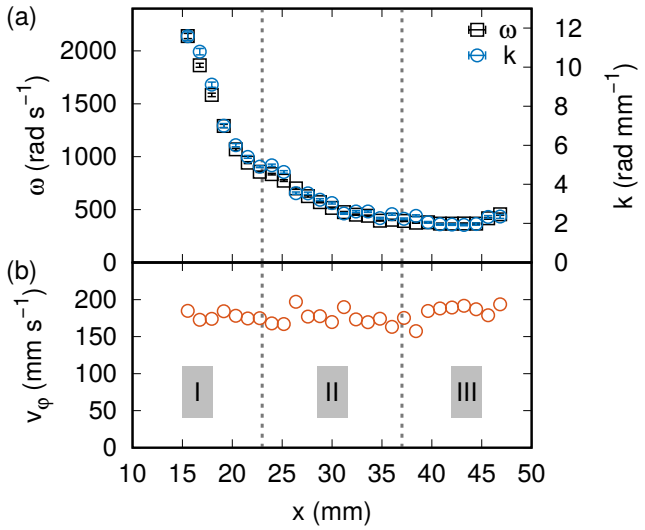

Fig. 5.3: (a) Wave frequency and wave number as obtained with the HILBERT transform. The horizontal axis is referenced to the center of the void, see Fig. 5.2 for clarification. It is sectioned into three regions with characteristic properties. Error bars are in the same range as the size of the points. (b) Phase velocity ω/k. In the observed area, the phase velocity is rather constant. For clarity, the original density of data points has been reduced by a factor of 30. The same applies for the subsequent Figs. 5.10, 5.11, and 5.12. [A.2, A.3]

frames was 1,024. This ensures that many wave periods in every location are included, which is important for the HILBERT transform to converge. The images have each been blurred with a GAUSSIAN filter before the HILBERT transform was applied.[1] This reduces the influence of uncorrelated noise on the camera chip. The filter options were a window length of 4 pixels and a sigma of 2 pixels. The maximum (minimum) wave number measured in the wave field is roughly $k = 11.5\,\mathrm{rad\,mm^{-1}}$ ($2\,\mathrm{rad\,mm^{-1}}$). A pure sine wave experiences a 15 % (0.5 %) amplitude damping effect by this filter. Since the larger wave numbers are only measured in a small area close to the void, the amplitude error introduced by the filter is only a few percent for most of the recorded data.

The resulting phase φ has no absolute reference, the respective values are between $-\pi$ and $+\pi$. The discontinuities in Fig. 5.2 have to be removed by "unwrapping" the phase information in time. A continuous phase is required to calculate the derivatives in time and space, which provide the frequency and the wave number.

The analysis of the wave is done on the Line of Interest (LoI) introduced in Fig. 4.6. The wave fronts are intersecting this line perpendicularly. From LANGMUIR probe measurements, see Fig. 6.2 in the next chapter, it is known that the ion flow is aligned with $\mathbf{k}$ on the LoI. A non-zero angle between $\mathbf{k}$ and $\mathbf{v}_i$ would be an additional parameter in the dispersion relation. Due to the symmetry of the system, oblique modes cannot appear on the LoI. Except for the LoI everywhere else the slope of φ would have to be calculated in two directions to calculate the wave vector.

The LoI is chosen for the analysis because it passes through the bulk plasma. Here, the drift velocity of the ions is low and the plasma density high compared to the area that is closer to the electrodes and to the plasma sheath. The waves can travel a long way with smooth variations of the plasma parameters. In the other directions, the parameters vary with larger gradients. Therefore, the complete analysis will be performed on the LoI.

[1] The "imfilter" function in *MATLAB*^{TM} was used for this.

Over the time of the video, a large number of instantaneous frequencies can be calculated on every pixel by determining the slope of the phase evolution in small parts of the video. Here, eleven subsequent frames (time steps) have been used to calculate the frequency for a distinct time and position. This leads to a distribution of frequencies whose average is treated as the wave frequency at that position. The same method was applied to the wave number. It follows from straight line fits in the phase data over a small window around each pixel. A window length of thirteen pixels has been used. This is done for every time step leading to a distribution of wave numbers. Here again, the average of the distribution is taken as the result for a location. At the same time, the distribution of instantaneous parameters provides a measure for the error. It is assumed that the error is given by the standard deviation of the mean. These errors are propagated into the consequent quantities by generating synthetic data sets with this standard deviation and repeating the data analysis to get a distribution of results and their standard deviation.
With this procedure, the wave number and wave frequency, as shown in Fig. 5.3 (a), are obtained. Several features become visible in this figure. First, the wave frequency and the wave number are almost aligned. This means that the phase velocity ω/k is constant. It has a value of about 175 mm s^{-1} [Fig. 5.3 (b)]. The constancy of the DDW phase velocity in this nanodusty experiment stands in contrast to observations in microdusty plasmas [128, 201]. The reason for this behavior is not clear yet. Further, it can be seen that both ω and k are monotonically decreasing, with large slope in region I, a diminishing slope in region II, and they are approximately constant from the center of region II throughout region III. The local constancy of ω and k will be an important requirement for the model used in Sec. 5.5.
The gradient in ω and k in region I and II shows that the wave is forced to adapt its parameters to the local plasma environment. The development of ω and k is smooth and shows no discrete jumps. Such discrete transitions of the frequency have been observed in a microdusty plasma [130] due to a local synchronization of neighbouring regions to one frequency. Such a region of fixed frequency is called a cluster. The absence of such clusters confirms the dominance of the local most unstable mode, which was discussed in Sec. 3.8.
The changing ω as in Fig. 5.3 (a) is a paradoxical behavior for a wave. If a wave passes points A and B one after another and has a lower frequency in B than in A, then more wave fronts enter the region between A and B than leave. Consequently, the number of wave fronts in this region increases. To resolve this problem, the gradient in ω makes it necessary to merge wavefronts. The merging position is called a phase defect. At the defect position, the wave amplitude is zero and the phase is undefined [202]. The appearance of defects will be discussed below.

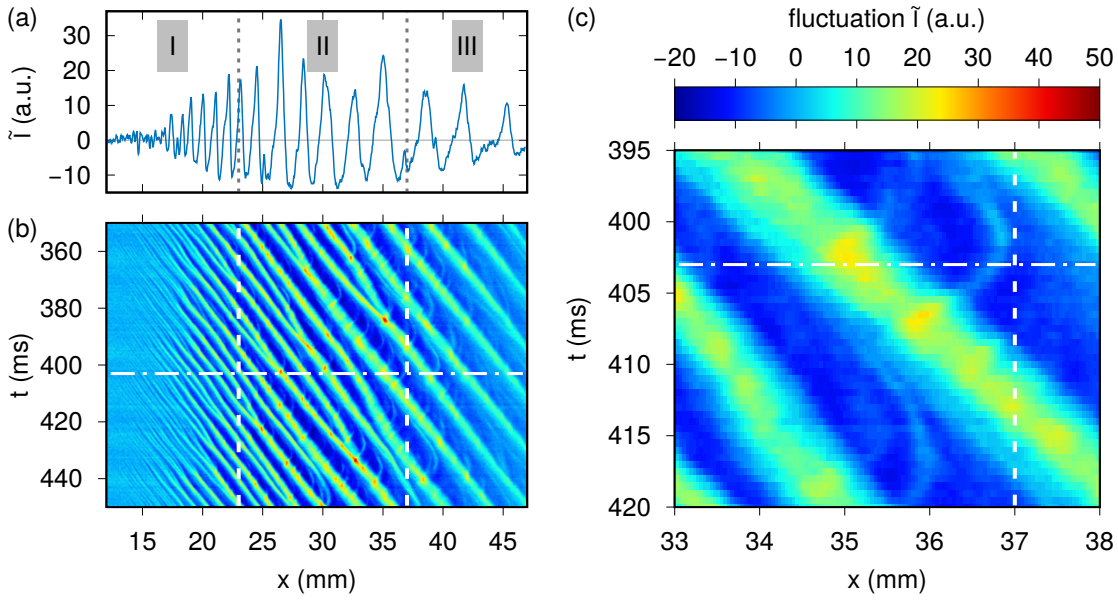

Fig. 5.4: (a) Fluctuation intensity $\tilde{I}(t) = I(t) - \bar{I}$ along the LoI. The zero-line is drawn in gray. (b) The fluctuation intensity over the same spatial dimension as in (a), but shown in color-coding and with time information on the vertical axis. This is a 100 ms long selection from a 512 ms video. The oscillations in (a) can be identified at $t = 403$ ms, which is marked with a horizontal dot-dashed line. Both subfigures share the same horizontal axis. The regions, which have been introduced in Fig. 5.3, are marked with vertical dashed lines. (c) A zoom into subfigure (b) sharing the same color legend.

5.2.3 Fluctuation Intensity

From the preceding subsection, the wave properties are available via the HILBERT transform. This method will be the main tool for the comparison with plasma theory in the next section, but it lacks some properties of the wave field, which can be better described by taking a look at the actual fluctuation of the wave.

In Fig. 5.4 (a), the fluctuation is shown along the LoI. On the very left, there is almost no deviation from the zero line. Starting at roughly $x = 15$ mm, very small waves can be found. Going outward, larger wave crests and troughs can be identified. In region II, the amplitude of the oscillations reaches its maximum. The fluctuation reaches twice as high values at the crests compared with the troughs. In region III, the amplitude of the oscillations gets smaller again. The waves are asymmetric w.r.t. the zero line. The right side of the crests is steeper than the left side. Additionally, the troughs become elongated and contain small-scale oscillations.

To show the dynamic features of the oscillations in Fig. 5.4 (a), the fluctuation from the LoI is transposed to a color axis and the time dimension introduced on the vertical axis in Fig. 5.4 (b). Now it can be seen that the onset of the waves on the left is not stationary, but is shifting its position between $x = 13$ mm and 17 mm. In contrast to Refs. [130, 201], the waves are not triggered at the void edge, but emerge somewhere in the dust cloud. While the waves travel towards region II, their wavelength increases and wavefronts

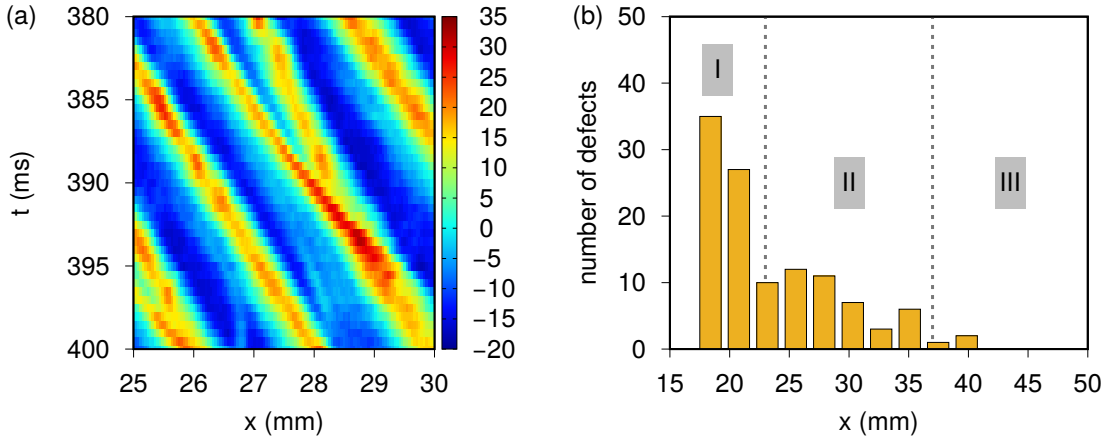

Fig. 5.5: (a) Zoom into the fluctuation intensity in Fig. 5.4 (b). A merging event of two wave crests is depicted. (b) Histogram of merging events (defects) over the LoI for the complete video.

merge. Many of those merging events can be identified in region I, some also in region II. No such event can be found in region III.

The defect positions for the complete video have been manually detected and registered into a histogram over the spatial axis. This is shown in Fig. 5.5 (b). In the given situation, every defect is a merger of wave fronts, splitting is not observed. From the distribution, it can be seen that defects appear where the wave changes its frequency ω, which is mainly the case in region I and II. In region III, the wave keeps its parameters constant and there are almost no defects. This is in accordance with the considerations above: a changing frequency requires the existence of defects. The distribution of the defects is continuous. MENZEL *et al.* found that the DDW shows frequency clusters [130]. These become visible by discrete jumps of the frequency on the spatial scale. Defects appear at the cluster boundaries. Therefore, the defect positions accumulated at these positions [201, 203]. In the present situation, the wave adapts its frequency smoothly, which makes it necessary to merge wave fronts with a continuous statistical distribution. If the defects accumulated in fixed positions, that would mean that the local most unstable mode is superimposed by the frequency synchronization within a cluster. Since the defect is a discrete synchronization process, a video of the DDW must be long enough to average out the discrete synchronization events. The life time of a cluster is usually some oscillation periods. With the given duration of the video recordings, at least 40 oscillations are captured on every pixel, which is sufficiently more than the life time of a cluster.

In region II and III, curved wave fronts can be identified in the t-x diagram [Fig. 5.13 (b, c)]. On the inward side of a wave crest, a group of particles separates from the crest forming a low-amplitude wave front. For a short time, this wave travels with the primary wave, but then gets slower, even stops in the laboratory frame. Finally, it changes direction and accelerates into the subsequent primary wave front, which peaks its amplitude during the collision. A zoom on such an event is depicted in Fig. 5.4 (c). Many

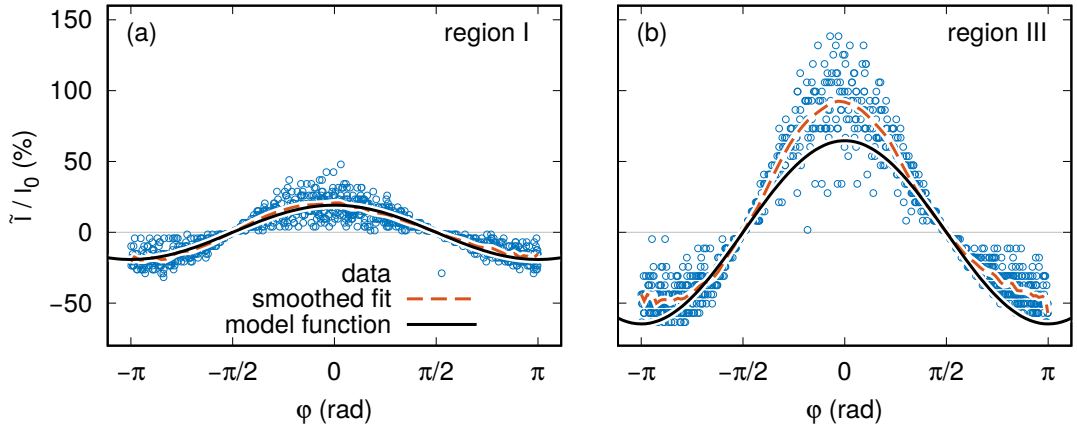

Fig. 5.6: Phase-resolved fluctuation degree for the positions (a) $x \approx 19\,\mathrm{mm}$ in region I and (b) $x \approx 39\,\mathrm{mm}$ in region III on the LoI. The data points are distributed on discrete levels because the oscillation amplitude is close to the camera bit resolution. The smoothed fit (dashed) is just a spline following the trend of the data points. The model function (solid) is $\bar{E} \cdot \cos(\varphi)$ with $\bar{E}$ being the medium amplitude from the complete time series.

of these events can be found in region II, some also in region III. This behavior indicates that the wave in region II and III is already in the nonlinear regime and shows effects, which are not included in the linear model of the DDW.

In the literature, many advanced phenomena in nonlinear DDWs have been explored yet: The group of MERLINO introduced two types of additional oscillations in the fluid model. It was shown that at high amplitude, second-order terms in the governing equations lead to higher harmonics in the wave field [204]. They also found that in the high-amplitude wave counter-streaming dust populations can excite a dust-dust instability, the secondary DDW [205]. Other groups identified the trapping and detrapping of particles in wave crests [140, 206, 207].

In my experiments, the single-particle trajectories are not accessible and it remains unclear what exactly causes the curved trajectories in the t-x diagram. It should be noted that nonlinearity in waves, which is clearly present in the experiment, is a long-standing subject of mathematics [208, 209].

5.2.4 Phase-Resolved Fluctuation Degree

The asymmetry of the oscillation intensity requires some discussion. The HILBERT transform assigns a phase φ for every pixel and time step of the recorded video. In Fig. 5.6 the relative fluctuation intensity for two representative positions in the wave field are plotted w.r.t. the phase information. In subplot (a) the data points are widely distributed, but reproduce a cosine curve quite well. This shows that the low amplitude waves in region I are well-suited for the planar wave ansatz. The amplitude calculated from the analytic signal is a good measure for the amplitude of the actual DDW.

In Fig. 5.6 (b) the relative amplitude is larger, but the data points at $\varphi = 0$ are farther away from the zero line than those at $\pm\pi$. The model function following from the medium oscillation properties is not symmetric in the data points, which becomes visible in the deviation of the model function from the smoothed fit. The wave-induced crests are up to 150 % over the medium density while the troughs are only up to 70 % under this value. This asymmetric shape is due to the fact that the dust density cannot be negative. The amplitude from the analytic signal averages the crests and the troughs. As this work limits its considerations to linear theory, one has to keep in mind that the wave in the experiment is not fully represented by the assumed model functions.
R. MERLINO showed that the asymmetric shape of the DDW in its nonlinear state as in Fig. 5.6 (b) follows from the second-order terms in the governing equations [204]. This shape can be reproduced as the sum of two cosines that represent the fundamental wave and its first harmonic.

5.3 Dust-Density Wave Diagnostic

The dust-density wave diagnostic (DDW-D) examines the naturally-occurring DDW. Experimental observations of the DDW provide its frequency, wave number, and amplitude. Hydrodynamic theory is independent of the amplitude. Thus, the diagnostic must handle all plasma and dust parameters while the experiment has an output of only two parameters from which everything else is determined. Therefore, it is necessary to employ all internal dependencies of the plasma, e.g., quasineutrality and charging, use external measurements—apart from the DDW itself—only where they have high accuracy, and require estimated parameters if their uncertainty introduces only a small error to the results. These were the requirements for the design of the DDW-D, which was published in Ref. [A.2] and further used in Refs. [A.3, A.4].

5.3.1 Reduction of Free Parameters in the Model Equations

Some of the parameters in the dispersion relation are known. By measurement of the neutral gas pressure, the ion-neutral, the dust-neutral, and the electron-neutral friction rate can be obtained. The dust particle size is given by CRAS-Mie, so the particle mass can be determined. The dust density is available with high spatial resolution by the method described in Sec. 4.4.2. The dust charge, electron and ion density, and the ion drift velocity are unknown. Ions and dust are at room temperature, for electrons a temperature of $k_\mathrm{B}T_\mathrm{e} = 5\,\mathrm{eV}$ is estimated [84]. It is assumed that the dust is non-drifting because even small drifts would suppress wave activity [210]. The simplifications discussed in Sec. 3.6 are applied.
With the four unknown parameters that have to be determined and only two measured parameters from the wave ($k,\ \omega$) the problem is underdetermined. Two restrictions from plasma theory are applied: The floating and the quasineutrality conditions Eqs. (2.27)

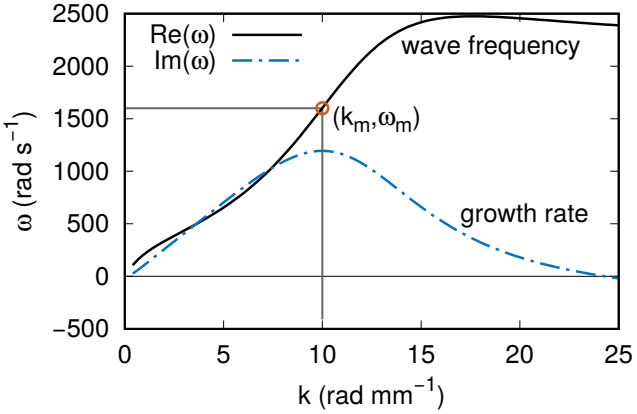

Fig. 5.7: Example dispersion relation for the nanodusty situation discussed in Tab. 2.1. The imaginary part of ω has a distinct maximum. This mode grows faster than all others. It is called most unstable mode or fastest growing mode.

and (2.28). These equations couple the ion density, the electron density, and the dust charge. For a given ion density, these equations determine the electron density and the dust charge. Thus, the inherent physical dependencies reduce the number of unknown parameters from four to two. By setting one pair of n_i and v_i one can calculate all parameters necessary for the dispersion relation.

In the dispersion relation, the local plasma parameters are present. From the HAVNES models in Sec. 2.2.3 only the local ion density model (LIM) includes the local ion density as a parameter. The HAVNES parameter in the BIM does not contain the local ion density, but the plasma density of the surrounding non-local plasma. Therefore, the choice of the HAVNES model can be justified by the fact that the dispersion relation contains only local plasma parameters and leads to a locally present mode of the wave.

Additionally, the ion mobility relates the electric field and the ion drift velocity, see Eq. (3.11). Solving Eq. (3.11), one is able to calculate the ion-neutral friction rate as $\nu_\mathrm{in} = e/(m_\mathrm{i}\mu)$. From the ion flow velocity the ion temperature follows with Eq. (3.17).

Given these prerequisites, a minimization method allows to find all unknown parameters at once. Starting with a certain set of parameters $(n_{\mathrm{i}0},\ v_{\mathrm{i}0})$, the most unstable mode $(k_\mathrm{m},\ \omega_\mathrm{m})$ can be determined by finding the maximum of the imaginary part of ω. The index m denotes the most unstable mode from the model. An example dispersion relation with real and imaginary part of ω is shown in Fig. 5.7. The deviation vector

$$(\Delta k,\ \Delta\omega) = (k_\mathrm{m}(n_\mathrm{i}, v_\mathrm{i}) - k_\mathrm{e},\ \omega_\mathrm{m}(n_\mathrm{i}, v_\mathrm{i}) - \omega_\mathrm{e}) \tag{5.5}$$

can be defined with the wave properties from the experiment $(k_\mathrm{e},\ \omega_\mathrm{e})$. Assuming that the most unstable mode is realized in the experiment, a root finding method can determine the $(n_\mathrm{i},\ v_\mathrm{i})$ for which the deviation vector vanishes. It can be helpful to minimize the absolute value of this vector and to introduce reference values k_r, ω_r, n_ir, and v_ir to make sure the root search is exploring both dimensions with equal weight:

$$\Delta = \left|\left(\frac{\Delta k}{k_\mathrm{r}},\ \frac{\Delta\omega}{\omega_\mathrm{r}}\right)\right| = \left|\left(\frac{k_\mathrm{m} - k_\mathrm{e}}{k_\mathrm{r}},\ \frac{\omega_\mathrm{m} - \omega_\mathrm{e}}{\omega_\mathrm{r}}\right)\right| . \tag{5.6}$$

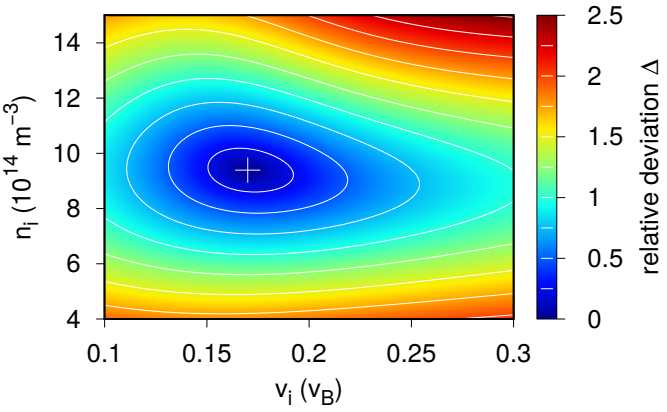

Fig. 5.8: Relative deviation Δ as in Eq. (5.6) for an example situation with $\omega_e = 1{,}600\,\mathrm{rad\,s^{-1}}$, $k_e = 10\,\mathrm{rad\,mm^{-1}}$. The reference wave parameters are $\omega_r = 600\,\mathrm{rad\,s^{-1}}$, $k_r = 5\,\mathrm{rad\,mm^{-1}}$. The dispersion relation is calculated with all parameters as given for the nanodusty situation in Tab. 2.1 and for a neutral pressure of $p_n = 11.5\,\mathrm{Pa}$. The deviation shows a clear root, which is marked by a plus (+).

The deviation Δ shows a global minimum, which can be found using standard root finding algorithms. An example situation is shown in Fig. 5.8. The function $\Delta = \Delta(n_i, v_i)$ originates from the dispersion relation, which is only implicitly given. From the dispersion relation only the most unstable mode is needed, which can be found with a maximum search algorithm. This utilizes the numerical solution of the dispersion relation. The accuracy of the maximum search algorithm produces a small-scale noise on the otherwise continuous behavior of Δ. Some measures must be undertaken to assure the root finding mechanism does not get stuck in minima created by numerical noise. The complete calculation of the deviations in the n_i-v_i plane takes one night of cpu time. In my programs, two solutions to this problem have been established. If the position of the global minimum is completely unknown and standard downhill methods fail to find it, simulated annealing algorithms will definitely reach a satisfying result. Unfortunately, they are very time-consuming but the only ones that can handle arbitrary configurations. An option that helped to keep the downhill minimum search from getting stuck in local minima is to set a minimum step width for the search.[2]

5.3.2 Discussion of the Method

By applying the described method on every point of Fig. 5.3, the DDW-D can map plasma parameters to the found wave parameters. Due to the spatial information that is attached to the wave parameters, the DDW-D provides spatially resolved plasma parameters, see Fig. 5.9. This is a big advantage compared to many other diagnostic methods like optical emission spectroscopy or microwave cavity methods. The dispersion of the wave in the experiment is acoustic. In the inhomogeneous medium only those waves are excited which correspond to the same phase velocity, see Fig. 5.9. From the current state of the literature [211] this effect cannot be fully explained yet. In the microdusty plasma, the phase velocity changes while the wave propagates [130].

[2] This was realized with the *DiffMinChange* option of *fsolve* in *MATLAB*^{TM}, version 9.2 (R2017a).

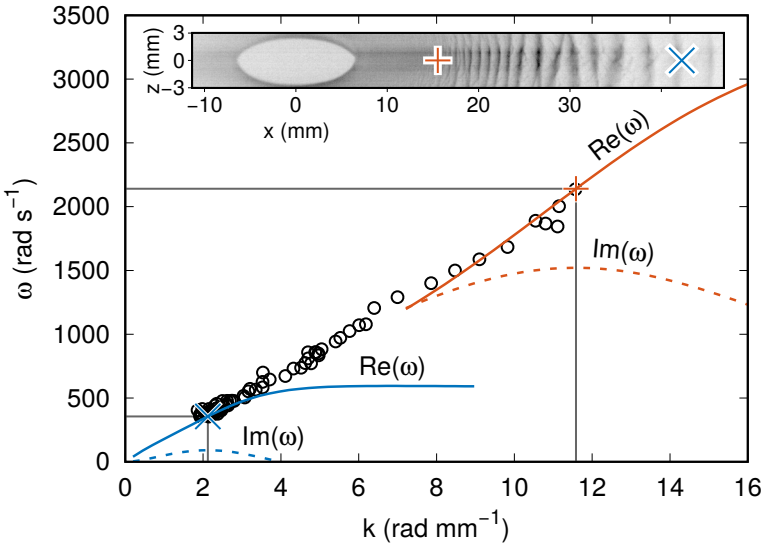

Fig. 5.9: Experimentally determined points in the k-ω-plane (black circles). The DDW-D determines the optimum fit by variation of ion density and flow velocity until the maximum growth rate (dashed lines) appears at the measured k and ω. Here, this is demonstrated for two different spots on the LoI (colored cross and plus in the inlay). The corresponding plasma parameters are $n_\mathrm{i} = 2.6 \times 10^{14}\,\mathrm{m}^{-3}$ and $v_\mathrm{i} = 0.27 v_\mathrm{B}$ at a dust density of $n_\mathrm{d} = 1.6 \times 10^{13}\,\mathrm{m}^{-3}$ for the blue curve and $n_\mathrm{i} = 2.3 \times 10^{15}\,\mathrm{m}^{-3}$ and $v_\mathrm{i} = 0.22 v_\mathrm{B}$ at a dust density of $n_\mathrm{d} = 4.3 \times 10^{13}\,\mathrm{m}^{-3}$ for the red curve. Other parameters are listed in Tab. 5.1. The data points fulfill a linear relation. This corresponds to a constant phase velocity over the LoI. [A.2]

The following restrictions come with the presented method: The hydrodynamic theory assumes full periodicity in the system. This would be realized in a homogeneous, large plasma. In the considered case of a small inhomogeneous plasma, the wave is forced to change its parameters during its propagation through the medium.

In analogy to the WKB approximation for the solution of the SCHRÖDINGER equation, it is assumed that within a small cell of the plasma, the parameters can be considered as constant. This cell represents the unlimited model system of the hydrodynamic model. The incoming wave has parameters close to the most unstable mode of each cell. Therefore, the wave has to adapt its parameters in the cell only slightly. The complete system is then given by a chain of such cells, which are placed one after another on the LoI. The wave parameters are obtained by averaging the instantaneous frequency and wave number over many oscillation periods. Therefore, the most unstable mode for each cell is known with high accuracy.

In the derivation of the electrostatic dispersion relation, it was assumed that second-order terms can be neglected. For low amplitudes of the DDW this assumption holds true, while for the larger amplitude further effects can be seen as discussed in Sec. 5.2.3. The model does not include saturation of the wave, predicting a temporal growth rate, which is independent of the wave amplitude. Of course, the observed waves are in equilibrium and do not change the amplitude with time. Some effects in the dispersion have not been

Fixed parameters	Value
Electron temperature	5 eV
Dust temperature	0.025 eV
Dust density	see Fig. 4.7
Dust radius	183 nm
Dust mass	3.34×10^{-17} kg
Neutral gas temperature	0.025 eV
Ion temperature	Eq. (3.17)
Neutral gas pressure	11.5 Pa
Free parameters	
Ion density	matched with experiment
Ion drift velocity	matched with experiment
Dependent parameters	
Electron density	Eqs. (2.27) and (2.28)
Electric field	Eq. (3.11) with μ from Ref. [152]
Ion-neutral friction	Eq. (3.11)
Dust charge	Eqs. (2.27) and (2.28)

Tab. 5.1: Input parameters used for the calculation of dispersion relations which are used to match experiment and model. Note that the assumed electron temperature for the nanodusty plasma is higher than in a dust-free plasma.

taken into account. These are deviations from a MAXWELLIAN velocity distribution and charge fluctuations [212]. An overview how to compose a dispersion relation for a given situation, can be found in Ref. [213].

5.4 Application of the DDW-D to an Unmagnetized Plasma

Now, the presented method is applied to experimental data. The results are published in Ref. [A.2] and Ref. [A.3]. A summary of the parameters is given in Tab. 5.1. Some values are different from the ones in the publication due to a refined implementation of CRAS-Mie, which provides a slightly different radius and consequently a different particle mass. For the deviation function Δ, the dispersion relation is explicitly given by Eq. (3.22) where the kinetic ion susceptibility from Eq. (3.15) is inserted with $\omega = 0$.

5.4.1 Ion Density and Dust Charge

With the method introduced in the preceding section, it is intended to determine the actual dust charge and ion density distribution in the nanodusty plasma. From the number density of dust, a significant deviation from the OML dust charge can be expected. Dust charge and ion density are depicted in Fig. 5.10 (a).
The ion density shows a monotonous decrease from the center of the plasma towards the wall. The ion density decrease is steep in region I, whereas it flattens in region II and III.

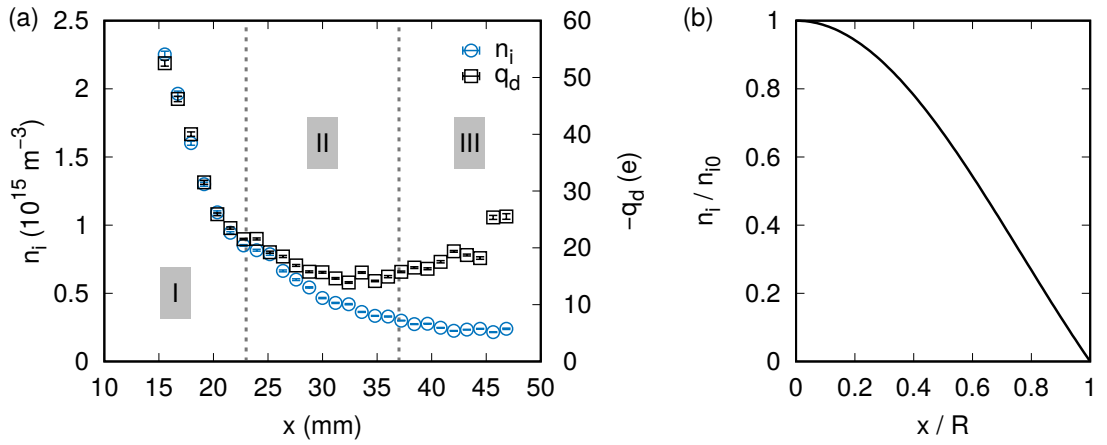

Fig. 5.10: (a) Ion density n_i and dust charge q_d along the LoI. In the following, the results will be discussed w.r.t. the three regions I, II, and III. (b) Theoretical ion density profile for a dust-free plasma in a long cylindrical tube with radius R and constant ionization rate in the volume. [A.2, A.3]

The absolute value of the ion density, about $10^{15}\,\mathrm{m}^{-3}$, is typical for the low-temperature rf plasma.

Comparing the experimentally observed ion density with the profile which is usually found with probe measurements in dust-free plasmas, a difference in curvature can be found here. The density profile for a plasma that has a constant ionization rate in the whole volume obtains a BESSEL-like profile [27] as in Fig. 5.10 (b):

$$n(x) = n_{\mathrm{i}0} \times J_0(2.405x) \tag{5.7}$$

with $n_{\mathrm{i}0}$ being the maximum density in the center and x being the relative radial coordinate. This formula leads to a negative curvature whereas the ion density profile obtained with the DDW-D has a positive curvature. Such a difference between a dusty and a dust-free plasma has also been found in a microdusty plasma under microgravity conditions [57]. Assuming that the ionization rate in the dusty volume is over-compensated by neutralization at the dust surface, a modification of the density profile seems plausible.

The dust charge shows a more complex behavior. In region I, the dust charge is aligned with the ion density and decreases fast. Here, the dust number density is constant, so the dust charge scales completely with the ion density. In region II, the dust charge reaches a minimum and separates considerably from the ion density. Further, in region III the dust charge even increases again where the ion density is still slowly dropping. Throughout regions II and III, n_d decreases, in region III even faster than n_i.

It is found that in region III, the dust charge rises although the ion density falls. This effect can be attributed to the confinement of the dust cloud. Since the cloud is trapped inside the plasma, its density (see Fig. 4.7) must drop faster than the ion density at the cloud

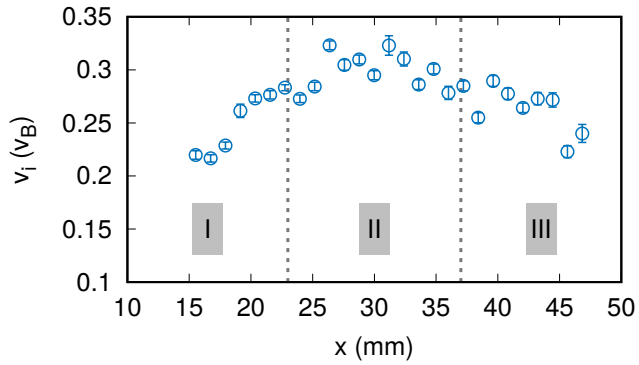

Fig. 5.11: Ion flow velocity in units of the BOHM velocity $v_B = \sqrt{k_B T_e / \pi m_i}$. Horizontal axis is equal to Fig. 5.10. Flow velocities of roughly 1/3 of the BOHM velocity are common for low-temperature rf bulk plasmas. [A.2]

edge. This leads to an increase of the ion to dust density ratio. This ratio determines the dust charge in this regime where almost all electrons are depleted from the plasma.
The overall dust charge is very low, ranging from 15 to 50 elementary charges. This value can be compared with the OML charge of an isolated dust particle in a plasma, which would be 1,500 elementary charges. The low value found by the DDW-D can be explained by the high dust density which leads to electron depletion in the plasma. The low electron density results in low charging currents to the dust. This emphasizes that the dust charge is completely regulated by the ratio of dust to ion density and can only be correctly determined by including the HAVNES effect. The DDW properties indicate a strong reduction of the charge. To my knowledge, this is the first spatially-resolved charge measurement inside a dense nanodust cloud.

5.4.2 Drift Velocity and Electric Field

The flowing ions experience a DOPPLER-shifted wave frequency. The resonance between the flowing ions and the spatial dust density modulation is the cause for the onset of DDWs. Therefore, the DDW is sensitive to the ion flow velocity, which is shown in Fig. 5.11. The ion flow velocities found here are common for the used low-temperature rf plasma. It increases in region I, stays constant in region II and decreases again in region III.
For reasons of symmetry the ion flow must vanish in the plasma center. The development of this flow velocity with distance from the center depends on the considered direction. In the z direction, the ion flow reaches BOHM velocity at the sheath edge. Here, the flow velocity is resolved in the x direction, which is given by the LoI.
The results found with the DDW-D in Fig. 5.11 show a low flow velocity in the center. The ion flow velocity increases towards a maximum, which is right above the electrode edge. Behind this edge, it decreases again. Similar results have been found in Ref. [A.1] for the unmagnetized system, which are reviewed in the next chapter, see Fig. 6.2.
The results in Fig. 5.10 and in Fig. 5.11 correspond to the same solution of the wave model to the experiment data. The ion temperature resulting from this solution, based on Eq. (3.17) is in the range of 0.1 eV. The electric field strength is about 1,000 V m^{-1}. The

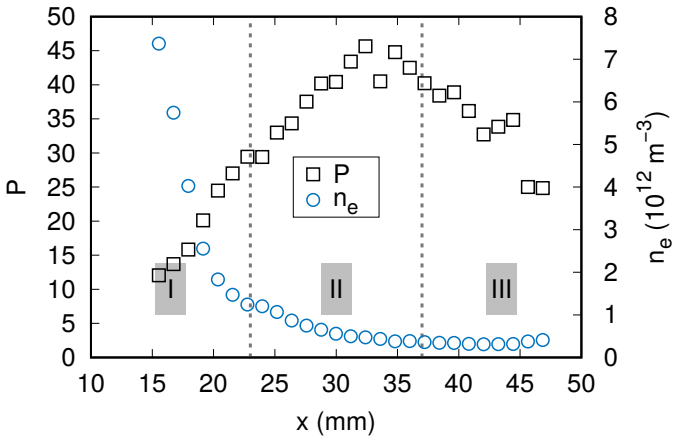

Fig. 5.12: HAVNES parameter P and electron density n_e along the LoI. Both quantities follow directly from the Eqs. (2.28) and (2.27) The HAVNES parameter is referenced to the local ion density (LIM) instead of the plasma density of the surrounding plasma (BIM). [A.2]

ion-neutral friction rate is about $3.5 \times 10^6\,\mathrm{s}^{-1}$ and the dust-neutral friction rate is $450\,\mathrm{s}^{-1}$. Electron-neutral friction can be neglected in the dispersion relation.

5.4.3 HAVNES Parameter and Electron Density

Finally, it is of high interest to quantify the strength of charge reduction in terms of the HAVNES parameter. This parameter is gained when solving the charging and quasineutrality equations.

Following the results from Fig. 5.12, the sectioning of the results becomes quite clear again. The HAVNES parameter starts at a value of 10 and increases throghout region I. Within region II it peaks at 50 and drops again throughout region III.

The electron density drops rapidly in region I and is in the order of $10^{12}\,\mathrm{m}^{-3}$. Here, it must be noted that the absolute value of the electron density depends strongly on the assumption of the electron temperature T_e which is only an estimate. Additionally, the electron density depends on the exact form of the charging current model. A modified equation for the ion current or the electron current will lead to a quite different value of the electron density.

Qualitatively, the n_e results from Fig. 5.12 can still be interpreted. The electron density is roughly two to three orders of magnitude smaller than the ion density. Diagnostics using microwave interferometry or microwave cavity resonance usually find a decrease of the electron density in the presence of nanodust by a factor of 5 to 10 [214, 215]. In another experiment, the electron density fell below the detection limit with the presence of dust, which makes it impossible to name an exact ratio [81].

It should be noted that microwave cavity resonance methods provide spatially averaged data with a complex spatial weighting function. A microwave interferometer averages over the line of sight. In the dust-free void, n_e is equal to n_i and there are high values

of n_i. Averaging over a vanishingly low electron density in the cloud and a high density in the void would result in a reduced ratio $n_\mathrm{i}/n_\mathrm{e}$. Therefore, it can be argued that the different results for n_e provided by the DDW-D compared to reported values of the electron density [80, 215, 216] might arise from the averaging of experimental methods to determine n_e.

5.5 Amplitude Evolution of Dust-Density Waves in an Inhomogeneous Plasma

The wave amplitude quantifies the effect that the wave has on the dust population. A high amplitude can introduce a heating mechanism [217]. It can provoke secondary waves [205], shocks [138], and even agglomeration of dust particles [147, 210, 218]. If it is known how the plasma parameters influence the amplitude, possibilities for manipulation become available. Therefore, it is of interest to study which parameters determine the amplitude.

The amplitude of the wave has been neglected so far. The linear model introduced in chapter 3 considers a wave that has a vanishing amplitude. In this way, all second-order terms are small compared to the first-order terms. The perturbation analysis shows whether modes grow or shrink. The actual growth rate is only valid for the medium in which the amplitude is zero. After a very short time, the amplitude saturates. This phenomenon cannot be observed in the experiment because the waves are self-excited and there is no preparable initial state without waves.

For the measurement of growth rates, the linear model can be used to determine the spatial growth of the wave. This means that the frequency becomes the independent variable in the dispersion relation and the wave number can be considered as complex. Then, the temporal growth is assumed to be zero—which is exactly the experimental situation—and the wave number has a real and an imaginary part. Theory and experiment deviate where the wave amplitude saturates due to effects which are not included in the model. The imaginary part of k has been measured in different experimental environments [119, 131, 133, 219, 220].

Here, the focus is on the evolution of the amplitude due to the inhomogeneity in the system. As there is no wave activity in the region next to the void, exponential amplitude growth can be found on the first few millimeters behind the point where the waves originate. The saturated wave evolves its amplitude due to the repelling interaction of the particles. From this principle, the behavior of the wave amplitude can be derived: The repelling interaction forces get stronger for increasing dust density and dust charge. It can be expected that an increased dust charge or density decreases the wave amplitude, because they increase the repelling interparticle forces. The wave is excited by the drifting ions. Therefore, its amplitude should increase with the ion density.

With the results from the preceding section, which include ion density, dust charge, and dust density, the amplitude evolution can be examined w.r.t. these parameters. The relative amplitude from the experiment is provided by the HILBERT transform. With the absolute dust-density measurement, the relative amplitude can be converted into absolute units.
Microdusty plasmas are well-suited for tracing single particles [218, 221, 222]. This allowed to find trapping of particles in the wave field [140, 146, 223], also in simulations [206]. Two-peaked velocity distribution functions were found [145, 217].
In the nanodusty DDW, single-particle trajectories are not accessible, but the dust density is high enough to provoke charge reduction and thus provide a charge gradient in the system. This allows to study the influence of a charge gradient on the amplitude.

5.5.1 Model for the Amplitude Evolution

The governing equations contain gradient operators. A variation in the wave amplitude due to variable system parameters can only be included by assuming that the system parameters are functions of the position. Inclusion of spatially varying parameters complicates the perturbation analysis from chapter 3.
In Ref. [224], gradients in q_d, n_d, n_i, $\tilde{n}_\mathrm{d}$, $\tilde{\Phi}$, $\tilde{v}_\mathrm{d}$, and n_e are allowed in the modelling of the system. An external driving mechanism of the wave is assumed which has a single frequency ω and wave number k. In the experiments, this mechanism is internal and self-excited.
The authors, SINGH and RAO, have utilized such an ansatz first without the charge inhomogeneity [225]. They do not incorporate friction with neutrals in their completely analytical model. From the governing equations, only the dust continuity and equation of motion are employed together with the POISSON equation. This finally leads to the amplitude function:

$$\tilde{n}_\mathrm{d} = C \cdot \frac{\sigma_\mathrm{ei} n_\mathrm{i} + n_\mathrm{e}}{q_\mathrm{d}^{3/2} n_\mathrm{d}^{1/2}}\,, \qquad \sigma_\mathrm{ei} = T_\mathrm{e}/T_\mathrm{i}\,, \tag{5.8}$$

where C is an arbitrary constant. In the given nanodusty plasma, the electron density is irrelevant because it is vanishingly low and the ratio σ_ei is quite large. Therefore, a modified version of this equation applies for the experiments:

$$\tilde{n}_\mathrm{d} = \tilde{C} \cdot \frac{n_\mathrm{i}}{q_\mathrm{d}^{3/2} n_\mathrm{d}^{1/2}}\,. \tag{5.9}$$

The wave increases its amplitude with the ion density and decreases it with increasing dust charge and dust density as argued above. The authors of Ref. [224] derived the exponents in Eq. (5.8) also for the nonlinear DDW and found them to be slightly different. In that case, the amplitude scales like $n_\mathrm{i}^{3/4} \times q_\mathrm{d}^{-1} \times n_\mathrm{d}^{-1/4}$, but this will not be considered here.

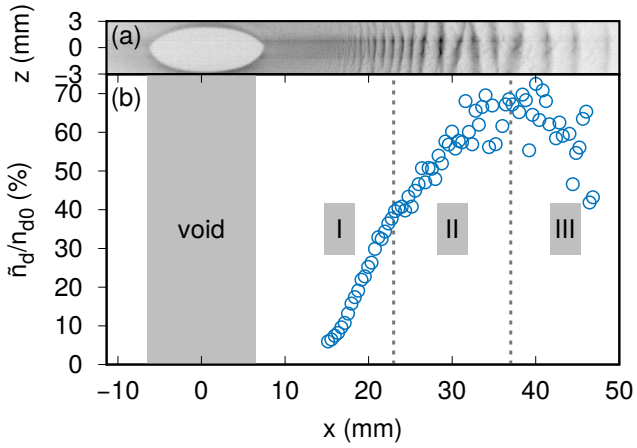

Fig. 5.13: (a) Image of the dust cloud as seen by the DDW camera. (b) Fluctuation degree of the DDW along the LoI. The values are calculated as the amplitude given from the HILBERT transform divided by the mean density. For clarity, the density of points is reduced by a factor of ten. [A.3]

5.5.2 Relative Amplitudes in the Experiment

The exponents in Eq. (5.8) could be determined independently if the experiment provided a possibility to prepare spatial gradients in one parameter while the others stay constant. Instead, the nanodusty plasma in the experiment has inhomogeneous profiles of nearly all parameters. Therefore, it is intended to compare the model function Eq. (5.8) using the parameters determined with the DDW-D to the measured amplitudes.

The HILBERT transform provides only the relative amplitude as long as the scattered light intensity is not calibrated to dust density. A profile of the relative amplitude is shown in Fig. 5.13. In the region very close to the void ($x < 15\,\mathrm{mm}$), no waves are observed. The HILBERT transform picks up camera noise and attributes an amplitude which has no physical meaning. Within region I, the wave emerges and the amplitude increases on a short scale. The fluctuation degree reaches 40 % at the border to region II. Beyond region I, the wave becomes a large perturbation to the system and has effects of nonlinearity. In this example, the relative wave amplitude increases throughout region II with a maximum of roughly 70 %. The form of the wave gets non-sinusoidal with very sharp wave crests. Towards region III, the form of the wave becomes flat again with decreasing fluctuation degree.

5.5.3 Comparison of Model and Experiment

By multiplication of the relative amplitude in Fig. 5.13 with the absolute dust density information in Fig. 4.7 one obtains the absolute DDW amplitude. This quantity is depicted in Fig. 5.14 and allows direct comparison to Eq. (5.8), which will be discussed in the following.

Starting in region I, the wave emerges from noise and shows exponential growth on the first few millimeters of its way. This strong spatial growth is not depicted by the model curve. Rather, it predicts a finite amplitude from the beginning. The underlying parameters that lead to this behavior are the decreasing dust charge and ion density. They result in a smooth increase of the amplitude. The deviations between theory and experiment in

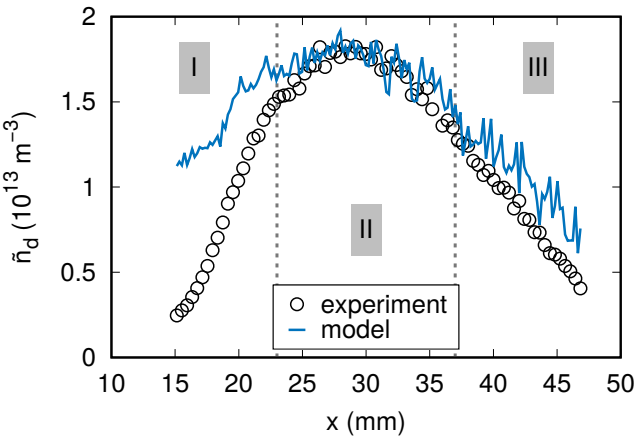

Fig. 5.14: Absolute DDW amplitude (circles) and model curve according to Eq. (5.9). For clarity, the density of points is reduced by a factor of ten. Ion density, dust charge, and dust density are inserted as given in Figs. 5.10 and 4.7. The free constant $\tilde{C}$ has been manually selected to match model and experiment. Compared with Fig. 5.13, the absolute amplitude has its maximum in the middle of region II instead of the border between region II and III. [A.3]

region I can be attributed to the self-excitation mechanism of the DDW. The wave is excited from the noise level in the region around the void and performs exponential growth as predicted by hydrodynamic theory. When the wave reaches its saturated amplitude at the border to region II, the model and the observed amplitude begin to coincide. An additional flaw to the applicability of the presented model to the experiment in region I is the fact that the wave parameters ω and k vary strongly in the experiment (see Fig. 5.3) and are assumed to be constant in theory.

In the middle of region II, the absolute amplitude has a maximum. This is a difference to the relative amplitude shown in Fig. 5.13. The maximum in the amplitude coincides with the minimum in the dust charge, see Fig. 5.10 (a). From Fig. 5.14 it can be seen that the observed and the predicted maximum are at the same position. The dust charge minimum is slightly shifted against this position to the right. Even this shift can be explained using the model function Eq. (5.8). The ion density is monotonously decreasing throughout all regions. Therefore, the decrease of n_i over the minimum of q_d leads to a shift of the amplitude maximum to the left.

From the maximum of the amplitude onward, the dust charge increases again, ion density and dust density decrease. The latter effect promotes an increasing amplitude, the first two effects support a decrease of the amplitude. Experiment and model show consistently that the behavior of n_i and q_d outweigh the decrease of n_d in regions II and III.

Altogether, a comparison of the experiment with the theory from SINGH and RAO shows good agreement in regions II and III and an understandable deviation in region I but still with matching trends. Especially for the right half of the data set it can be confirmed that the wave decreases its amplitude as it travels into a region of increasing dust charge. This is one of the main statements of Ref. [224] and has been confirmed here for the first time.

5.6 Conclusion

If the wave field can be measured with high resolution in space and time, the DDW-D allows to determine the profiles of plasma density and dust charge. A requirement is the knowledge of the mean dust density and the neutral pressure. The DDW-D utilizes some assumptions, the most important being the dominance of the most unstable mode from hydrodynamic theory.
The absence of frequency clusters and the smooth variation of ω and k on the LoI indicate that the local most unstable mode in every location is able to prevail against synchronization with the incoming wave.
The application of this method to DDWs observed in a nanodusty plasma results in plausible plasma parameters which show similar absolute values as comparable measurements in dust-free plasmas. The general change in the profile of the ion density was also found in microdusty plasmas.
The dust charge is found to be very low due to the high dust number density. The spatial distribution of the charge with an increase towards the cloud edge is beneficial for the confinement of the dust cloud.
The availability of the plasma parameters inside a dense dust cloud with gradients not only in the ion and dust density but also in the dust charge allows to study the interaction between these system parameters and the DDW amplitude experimentally, which was not possible before. Comparison with hydrodynamic theory with a static driver of a wave instead of self-excitation shows good agreement where the wave parameters are only slowly varying. The applicability of this model has implications for the prediction of the wave behavior in inhomogeneous systems. It explains why and where the wave is driven to nonlinear behavior and improves the design of nanodusty plasma reactors in research and technology w.r.t. the occurrence and strength of DDWs. It allows to choose parameters in a way that dampens the amplitude if DDWs are unwanted or to enhance it if they are appreciated.
The DDW-D is a diagnostic for the dusty plasma comparable to the LANGMUIR probe for the dust-free plasma. The quantitative influence of any input parameter on any output parameter can be determined. Examples are the influence of pressure, input power, bias voltage, dust density, dust size or any other parameter influencing the system. The effects can then be seen in the resulting ion density, drift velocity, and dust charge. There remains a large variety of applications for the DDW-D, not just in nanodusty plasmas, but in any dusty plasma that excites DDWs on its own.

6 Probing a Dusty Magnetized Plasma

Magnetized plasmas have been studied for a long time due to the confinement of the plasma, which is provided by the magnetic field. This is the core idea of magnetic fields in fusion-related devices. A strong magnetic field is needed to prevent contact between the hot plasma and the cold wall. In astrophysical situations magnetic fields that are orders of magnitude smaller have a strong influence on the plasma behavior due to the absence of friction [226].
In contrast to these classical situations, which have been under scrutiny for decades, the dusty plasma that is exposed to a magnetic field was only rarely studied although its appearance in processing plasmas is not unusual. An example is the magnetron sputtering plasma, which can be operated in a parameter range that favors the onset of DDWs [227]. There are some difficulties in producing a magnetized plasma that traps dust particles. Growing dust in a reactive plasma under the exposure of a magnetic field results in a hollow profile of negative ions preventing the creation of dust [A.1, 183, 228]. The deflection of ions in the magnetic field sets the dust cloud into rotation [85]. The centrifugal forces can overcome the confinement potential of the plasma [46]. In dusty plasmas, the appearance of filaments, regions of enhanced light emission and propably enhanced ion density elongated along the magnetic field line, disturb the dust cloud [229–231].
Magnetized dusty plasmas promise insights into the charging mechanism of dust under the influence of the magnetic field [232], the dynamics of dust in the magnetized plasma [230, 231, 233, 234], and the behavior of a magnetized plasma component if the dust can be magnetized [86, 88]. Additionally, waves [41, 196, 235] and modes [236] can be fundamentally different in the magnetized plasma environment.
In the following, a certain schedule for the conduction of experiments in the DUSTWHEEL is proposed that allowed to overcome the problem of filamentation and dust confinement in a certain regime of magnetic inductions. The DDW-D and all optical diagnostics are applied on the system while it is exposed to a vertical magnetic field. This is how the magnetized plasma inside the dust cloud is probed.

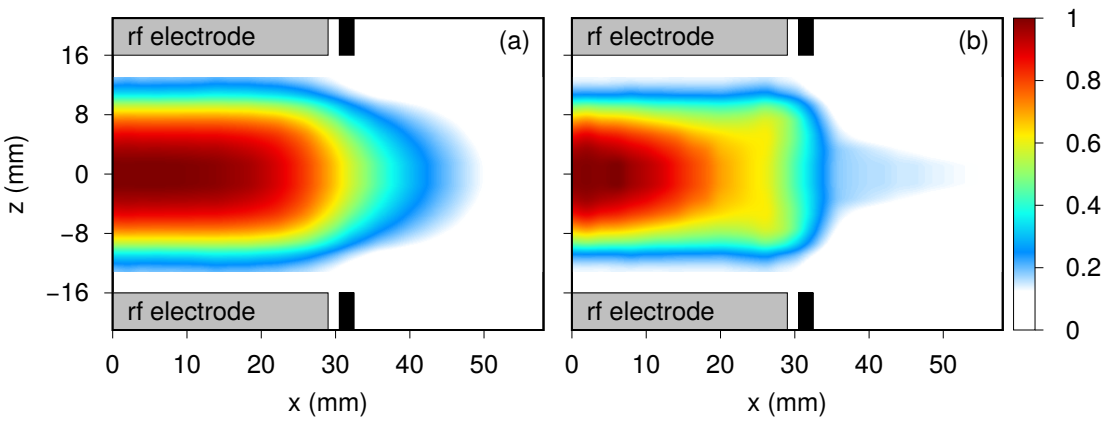

Fig. 6.1: Relative ion density profile w.r.t. the maximum value of each meaurement. Only the area between $z = -13\,\mathrm{mm}$ and $z = 13\,\mathrm{mm}$ is measured because probe theory is not applicable in the sheath. The densities have been determined with a LANGMUIR probe in the dust-free discharge by measuring the ion saturation current on a grid with a spacing of 2 mm. The data have been obtained for the lower quadrant and mirrored into the upper quadrant. The measurement has been performed twice, (a) in the unmagnetized and (b) in the magnetized case with $B = 400\,\mathrm{mT}$. The FARADAY shield of the electrodes is drawn in black. [A.1]

6.1 Comparison of Magnetized and Unmagnetized Plasma

6.1.1 LANGMUIR Probe Measurements

The LANGMUIR probe is the most common diagnostic in plasma physics, ranging from cold thin plasmas to dense hot fusion plasmas. For dusty plasmas its application is often impossible as it destroys the fragile force equilibrium that keeps the dust in place [237]. Although sophisticated experiments were able to use the LANGMUIR probe for this purpose [83, 84, 238], this is not intended here.

Instead, the plasma is studied with the probe in the absence of dust. In this configuration, the general plasma properties become visible whereas the actual situation with dust must be considered with the DDW-D. Therefore, a negatively biased probe was moved through the central plane of the plasma at $p_\mathrm{n} = 24\,\mathrm{Pa}$ and an rf power of 8 W with a spatial resolution of 2 mm in both directions. These studies have been conducted in *setup A* where the electrode diameter was still 58 mm. All other material presented in this chapter was obtained with *setup B* using 50 mm electrodes.

The motivation of the probe measurements was to distinguish the influence of the vertical magnetic field on the plasma. The 0 and the 400 mT cases are compared. The respective data are presented in Fig. 6.1. In the unmagnetized case, see Fig. 6.1 (a), the plasma has its maximum density in the bulk center, it drops towards the electrodes, and is rather diffuse in the direction towards the chamber wall. The influence of the electrode shield is visible since the plasma density is reduced close to the shield position.

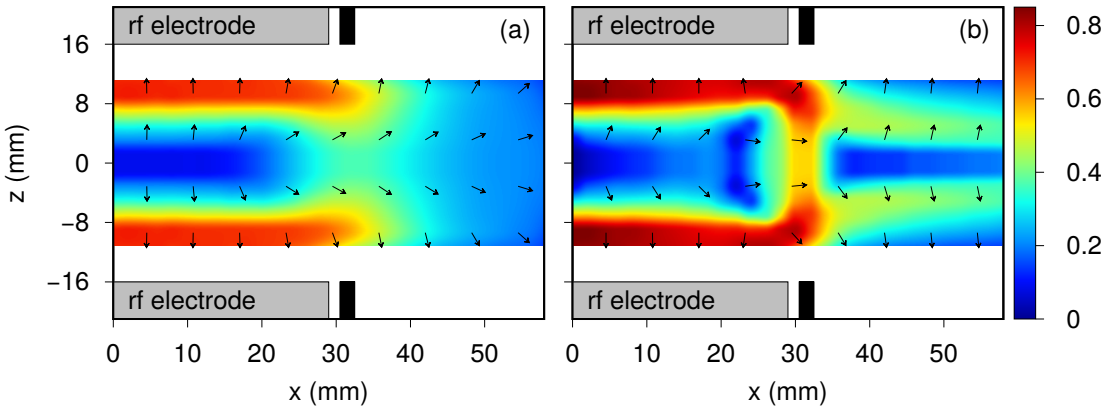

Fig. 6.2: Ion flow velocity calculated from the measured floating potential distribution. The vectors are only representing the local directions of the ion flow. The absolute strength of the ion flow velocity is given in color coding in units of the BOHM velocity assuming that the electron temperature is 3 eV over the whole space. [A.1]

This situation is contrasted by the magnetized case in Fig. 6.1 (b). Here, the profile towards the plasma sheath is steeper. The plasma is limited at the vertical connection line between the two shields. Beyond this line, the plasma density is quite low.

Beside the density distribution, the ion flow map should be determined since the ion flow is the source of energy for the DDW. It follows from the ambipolar electric field or the plasma potential distribution. Measuring the plasma potential itself with a probe is an ambiguous task. As a simplification, only the floating potential distribution is measured assuming that the electron temperature is relatively constant in the observed area. This was confirmed by measuring probe I-V-curves in representative locations. Therefore, a floating potential map is obtained that should have nearly the same gradients than the actual plasma potential.

From the potential distribution, the electric field can be calculated with $\mathbf{E} = -\nabla\Phi$. The ion flow vector follows generally from Eq. (3.9). This operation requires only the constancy of the electron temperature on distances that are as long as the grid size of the probe measurement. The effect of a field-dependent ion mobility must be taken into account especially for strong electric fields. Therefore, Eq. (6.4), which will be introduced below, was used.

This results in the vector field in Fig. 6.2. Along the LoI the flow velocity increases coming from the center towards a maximum at about $x = 30\,\mathrm{mm}$ and decreases again towards the wall. This is exactly the behavior found by the DDW-D, e.g., the data in Fig. 5.11. Close to the sheath, the flow velocity approaches BOHM velocity.

In the magnetized case depicted in Fig. 6.2 (b), the flow velocity is lower in the central part of the discharge and increased at the connection line between the two shields. There, the ion flow velocity is about $0.5 \times v_B$. This increased ion flow velocity is a consequence of a clearly increased electric field at the electrode edge. A stronger electric field increases

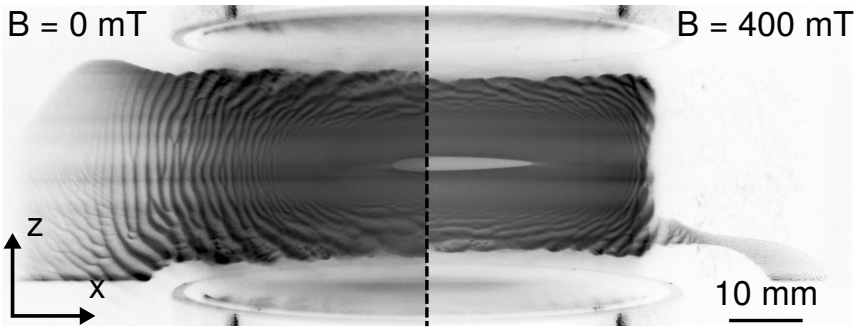

Fig. 6.3: Photo of the central vertical plane illuminated by a laser sheet. The images have been inverted. The electrodes with their respective shielding are visible at the top and bottom. In the unmagnetized case (left) the dust density drops smoothly in the radial direction. With the presence of a magnetic field (right), the dust cloud forms a sharp edge at the electrode shield. [A.1]

the confining force on the dust cloud. This effect can directly be seen in the arrangement of the dust cloud. A dust cloud that has just grown and is now subjected to a magnetic field is depicted in Fig. 6.3 before and after a magnetic induction is turned on. While the dust dilutes into the volume of the plasma chamber for the unmagnetized case, it is confined into a cylinder between the electrodes when a magnetic field is present.

6.1.2 Stability of the Dust Cloud

In a first attempt to create a dusty magnetized plasma, I added acetylene to the magnetized argon plasma. In Fig. 6.4 a dust cloud can be seen that is grown in this setup. The particles do not fill the bulk plasma. In accordance with earlier studies in Refs. [183, 228] the growth in the reactive magnetized plasma is inhibited due to a hollow profile of negative ions. Therefore, the dusty magnetized plasma can only be produced by preparation of the dust cloud in the unmagnetized reactive plasma. When the particles have reached a sufficient size, the acetylene supply is closed and the plasma switches back to a pristine argon plasma. After some seconds, the acetylene has left the plasma chamber and the DUSTWHEEL can be ramped to its maximum magnetic induction within seconds. The previously grown dust cloud stays in the plasma bulk even during this ramping procedure. It takes a few minutes to acquire the data to study the dust cloud in the magnetized

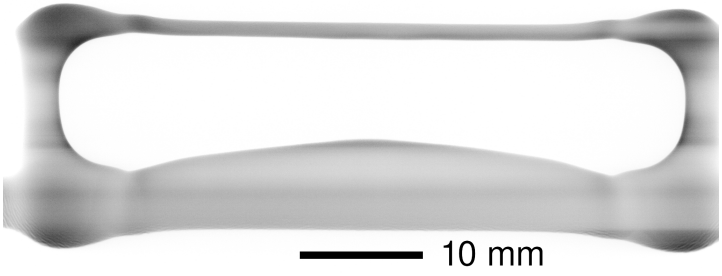

Fig. 6.4: Inverted Photo of the central vertical plane of a dust cloud grown in a magnetized argon-acetylene plasma at 50 mT. The central volume remains dust-free. [A.1]

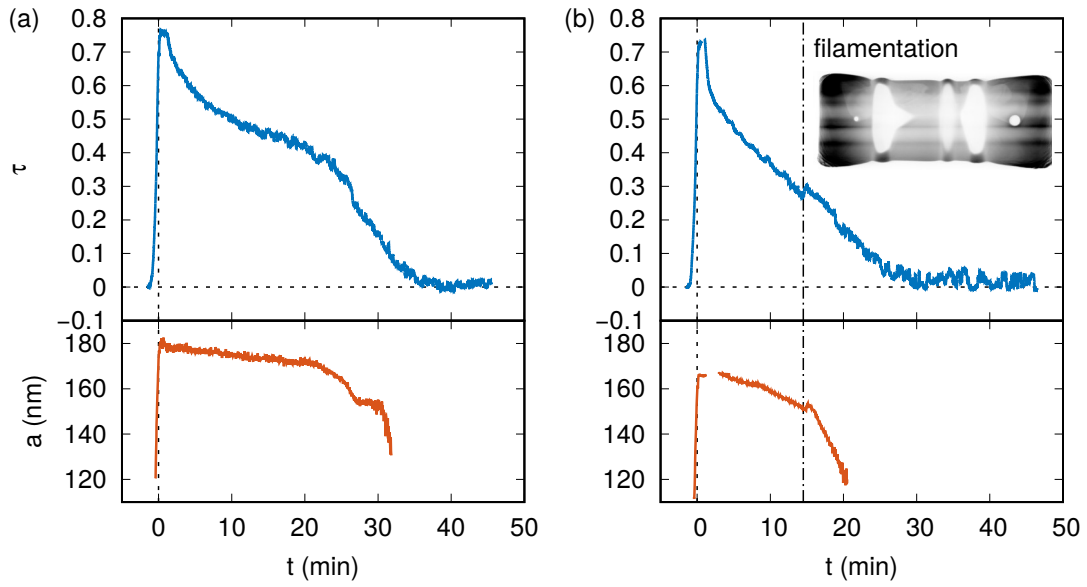

Fig. 6.5: Optical depth τ (upper panels) and particle radius (lower panels) for a long-time measurement. Dust is grown using acetylene and slowly disappears after the acetylene supply has been closed at $t = 0$. (a) In the unmagnetized situation, a two-stage process appears where the cloud is firstly losing particles and secondly the particles decrease in size. (b) In the magnetized situation with a magnetic induction of 400 mT, there is also a two-stage process, but the second stage is introduced by the appearance of filaments. The onset of filaments is marked by a vertical dot-dashed line. They become visible as vertical elongated voids in the central illuminated plane of the cloud. As an example, an inverted photo of such filaments in the central plane is included as an inlay. There is a gap in the data set of the lower panel in (b) because the optical depth was too high for the application of CRAS-MIE. [A.1]

plasma. However, it is important to check whether the cloud is stable for this amount of time.

Therefore, the optical depth τ and the polarization state of the scattered light from the particles were measured for the dust cloud in Fig. 6.3 in an unmagnetized and a magnetized configuration. The respective data are presented in Fig. 6.5. Using CRAS-MIE, the polarization data have been translated into a time-resolved radius development [B.2].

The long-term behavior of τ shows in both cases that the cloud disappears within 30 min. From the development of τ it can be inferred that the decay of the dust cloud happens in two stages. In the first minutes, the dust cloud is losing particles resulting in a decreased dust density. The particle size reduces only slowly during this first stage. After some time, the particle loss is accompanied by a dropping particle size, which marks the beginning of stage two. In the unmagnetized case, this transition between the two stages is at roughly $t = 24$ min. It is clearly visible that the optical depth accelerates its decrease at the beginning of the second stage.

A difference between the two cases is the dynamics of the dust cloud. In the magnetized case, the dust cloud shows filaments at roughly $t = 14$ min. This filamentation becomes visible in the dust cloud as vertical voids. A photo of them is included as an inlay in

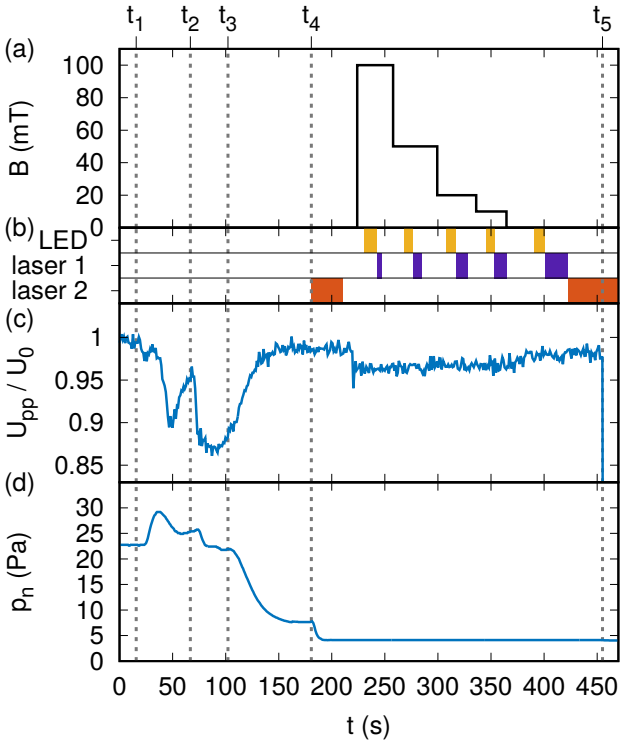

Fig. 6.6: Timing diagram. At $t_1 = 16\,\mathrm{s}$ the acetylene flow is opened, which is closed again at $t_2 = 67\,\mathrm{s}$. At $t_3 = 102\,\mathrm{s}$ the valve is opened to 40 %. The argon flow is reduced from 8 to 3 sccm at $t_4 = 181\,\mathrm{s}$. The plasma is turned off at $t_5 = 455\,\mathrm{s}$. (a) Magnetic induction. (b) On-times of the illumination sources. Every time the LED panel is on, it is used to make an extinction image of the cloud. Laser 1 is in operation when making a DDW video and laser 2 is active when measuring the polarization state of the scattered laser light. (c) Relative peak-to-peak voltage measured between the two electrodes. (d) Pressure from the combivac. The data between t_1 and t_2 are uncertain because the gauge is gas-type dependent.

Fig. 6.5 (b). Repeating this experiment with a horizontal instead of a vertical laser sheet showed that these column-shaped voids perform a rotational motion. Comparing the size development of the two cases, it is found that the particle size drops faster in the magnetized case. The transition to the second stage of the decay process coincides with the appearance of the filaments.

The decreasing particle size during plasma exposition is an effect that has been observed in many different situations [113, 239, 240]. In the following, the complete study will be concentrated on the first stage, which means that the particle density drops during the conduction of the experiment, but the particle size is constant.

6.2 Experiment Schedule

The setup to study the magnetized situation was altered as discussed in Sec. 4.4.5. The conduction of the experiment will be discussed w.r.t. Fig. 6.6.

A dust cloud is prepared as before by adding acetylene to the neutral gas flow through the chamber. After about 50 s the acetylene supply is closed again. The appearance of the dust is clearly visible in the rf voltage [Fig. 6.6 (c)] as the plasma impedance changes. During the growth of particles the turbomolecular pump is bypassed. Here, the experiments with a magnetic field are intended to be at low pressure to enhance the onset of DDWs. Therefore, the bypass is closed and the throttle valve to the turbomolecular pump opened slightly so that the system pressure remains constant while changing the pump. Afterwards, the valve is opened to 40 % at $t = t_3$. Consequently, the pressure in the sys-

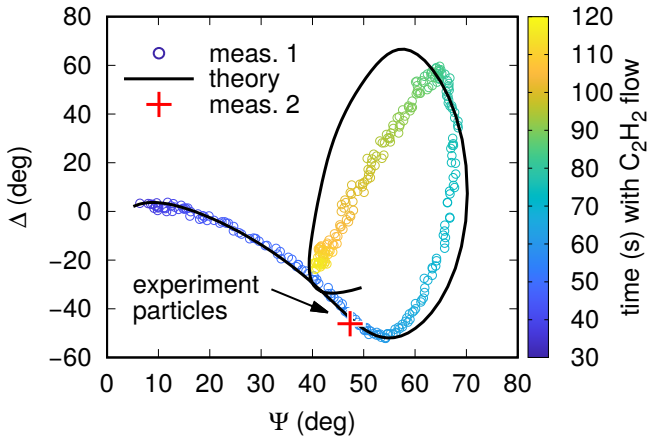

Fig. 6.7: Polarization state of the scattered light represented by ellipsometric angles Ψ and Δ. The colored circles (meas. 1) are measured polarization states of a complete growth process before the main measurement is initiated. The black curve represents the CRASMIE fit to these data. The red plus marks the average signal measured right before ramping the magnetic induction in the main measurement (meas. 2). © 2018 American Physical Society [A.4]

tem falls [Fig. 6.6 (d)]. When it has reached a stable value, the flow is reduced to 3 sccm at $t = t_4$ so that the pressure falls to 4 Pa.

The system in this state is of interest for the following experiments with magnetic fields. Now, the timing of the diagnostics must be adjusted to each other because all optical diagnostics use light of nearly the same wavelength. In Fig. 6.6 (b) the on-times of the different light sources are displayed. First, the size of the dust particles is determined by turning on laser 2, which allows to measure the polarization state of the scattered laser light on the RCE and the optical depth with the photodiodes. This is repeated at the end to ensure that the dust particles have not significantly changed in size during operation of the experiment. During the growth phase of the dust particles, the laser was off to make sure that it does not disturb the growth process. The complete growth history of the particles is needed to determine the refractive index. Therefore, the growth of particles was recorded with a measurement run right before this experiment was conducted.

Next, the DUSTWHEEL is turned on to 100 mT [Fig. 6.6 (a)]. The following schedule is repeated at 50, 20, 10, and 0 mT. The telecentric cam takes an image of the plasma and the DDW cam a dark image. The LED panel is turned on and the telecentric cam takes an extinction image of the dust cloud, which will later allow to determine the dust-density distribution. It is turned off, laser 1 is switched on, and the DDW cam records a video of DDWs with high temporal resolution.

The analysis and results from these data will be the main part of this chapter.

6.3 Characterization of the Dust Particles

For the experiments with a magnetic induction, the dust needs to be characterized using the laser-light scattering measurement depicted in Fig. 6.7 in order to determine a particle size and extinction efficiency. This is organized in two steps: First, a complete growth history is measured (meas. 1 in Fig. 6.7). The plasma is turned off, the particles are removed with the gas flow, and the main measurement is started as described in the preceding section.

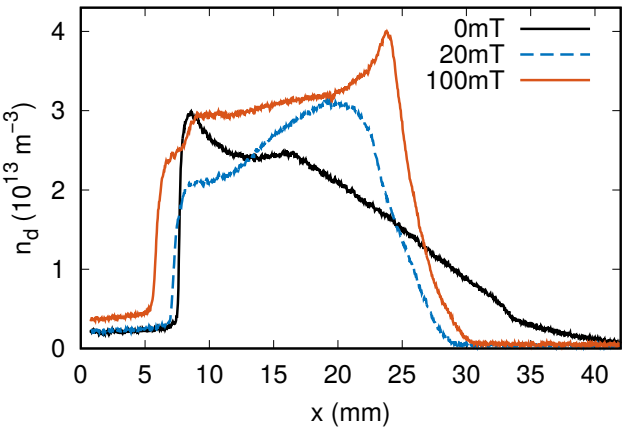

Fig. 6.8: Dust density along the LoI. Here, the density is obtained by absolute calibration of the intensity profile of the scattered light. The non-zero density in the center can be explained as the contribution from multiple-scattering events. © 2018 American Physical Society [A.4]

When the new dust cloud is grown, but the magnetic induction is not yet switched on, laser 2 is active for a couple of seconds and the polarization state of the scattered light from the particles is measured (red cross, meas. 2 in Fig. 6.7). The CRAS-MIE analysis of the $\Delta(\Psi)$ data results in a refractive index of $1.74 + 0.07i$. The dust particle radius of the experiment particles in the main measurement (meas. 2) is found to be $a = 152\,\mathrm{nm}$ and their extinction efficiency is $Q_{\mathrm{ext}} = 2.906$. As the optical properties of the particles are available, the intensity profile on the LoI can be translated into an actual density as described in Sec. 4.4.2.

This provides an insight into the structure of the dust cloud at different magnetic inductions, which will be completed by the 2D density measurement with an LED panel and telecentric lens. The density distribution along the LoI is shown in Fig. 6.8. In the sequence of events the 100 mT case was the first. A central void formed, from which the density increases towards a peak at $x = 24\,\mathrm{mm}$. From there, the dust density decreases to zero. Decreasing the magnetic induction, the excentric density maximum goes to the center and is finally located at the void edge. When the magnetic induction is decreased to zero, the dust cloud loses its sharp edge and extends itself into the chamber volume.

The excentric density maximum at $B = 100\,\mathrm{mT}$ is a surprising result. From the probe measurements, it can be assumed that the electric field at the electrode edge is much stronger than in the unmagnetized setup. This explains the sharp edge of the dust cloud, but it does not explain why the dust density reaches a maximum right before this edge. A simple guess would be that there is a new potential maximum before the edge. The DDW is propagating from the center to the wall, trespassing the density maximum. From this observation, it can be ruled out that the plasma potential has an additional local maximum on the LoI other than in the center. The slope of the potential distribution influences the propagation direction of the DDW since the ions excite the DDW in their flowing direction [241].

6.4 Dust-Density Waves in the Magnetized Discharge

The magnetization of a plasma depends on the influence that the magnetic field has on the plasma components. A magnetic field blocks the diffusion perpendicular to the magnetic field lines. The HALL parameter H, the ratio of cyclotron frequency to neutral collision rate, decides whether collisions or the magnetic field are dominating the motion of the particles. In the context of waves, another parameter is even more important for the magnetization, the ratio of cyclotron to plasma frequency. This ratio determines whether the gyration is dominant against plasma oscillations.

$$H_j = \frac{\omega_{cj}}{\nu_{jn}}\,, \qquad \beta_j = \frac{\omega_{cj}}{\omega_{pj}} \tag{6.1}$$

SATO *et al.* have introduced a classification for the magnetization of dusty plasmas [242]. They called the magnetic field weak if only the electrons were magnetized ($H_e, \beta_e > 1$). A strong magnetic field also leads to $H_i, \beta_i > 1$ and an ultrastrong magnetic field even magnetizes the dust particles.
At the given experimental conditions, electrons get magnetized at roughly 1 mT, ions at 3 T and dust at 8,000 T. The exact conditions for this calculation can be found in the Appendix, Sec. 8.2. In the following, a magnetic induction of 100 mT is applied. So electrons get magnetized while ions are weakly influenced by the magnetic field. The dust motion is not influenced by the magnetic induction. This means that the DDW-D under the given circumstances resolves the changes in the system due to electron magnetization. To stress that the magnetic field has no direct effects on the dust particles, the chapter title introduces "dusty magnetized plasma" instead of a "magnetized dusty plasma".

6.4.1 Wave Parameters

The wave properties can now be determined as in the unmagnetized case using the HILBERT transform. The resulting wave parameters are given in Fig. 6.9. In the magnetized cases, ω and k decrease towards zero right behind the electrode edge. In the intermediate case of $B = 20$ mT the frequency and wave number are already equalling the 0 mT case in the center but reduce to zero at the electrode edge. In the unmagnetized case, these parameters are monotonously decreasing but they reach a constant value, far beyond the electrode edge.
It has not been observed before that a DDW reduces its frequency and wave number to almost zero as it approaches the plasma and cloud edge. This is a unique property of a dusty plasma, which experiences very strong confinement.

6.4.2 Applicability of the DDW-D

So far, the DDW-D has been applied only in the case of an unmagnetized system. With the presence of a magnetic field, the ion flow gets deflected. Additionally, the ion mo-

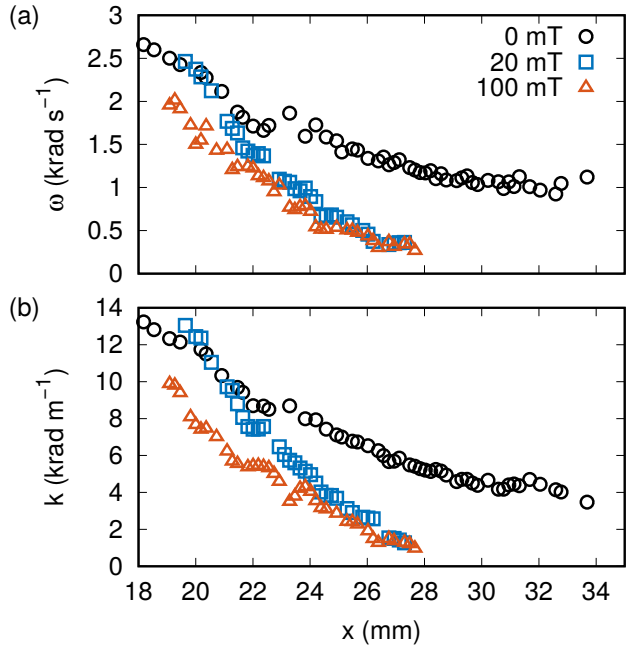

Fig. 6.9: DDW wave properties. (a) Wave frequency ω and (b) wave number k. Error bars are smaller than the circle diameter and therefore not shown. © 2018 American Physical Society [A.4]

bility and its dependence on the electric field should be taken into account. The original empirical formula for the ion mobility given by FROST is [152]:

$$\mu = \frac{\mu_0 p_0 / p_\mathrm{n}}{\sqrt{1 + a(E/p_\mathrm{n})}} \,. \tag{6.2}$$

with a, μ_0, and p_0 in the case of argon

$$a = 0.0352\,\mathrm{Pa\,m\,V^{-1}}\,, \qquad \mu_0 = 0.146\,\mathrm{m^2\,V^{-1}\,s^{-1}}\,, \qquad p_0 = 133\,\mathrm{Pa}\,. \tag{6.3}$$

KONOPKA *et al.* have introduced a modification to FROST's empirical formula. Assuming that the transition to an equation of motion with a magnetic field can be seen as a replacement of $\mathbf{E}$ with $(\mathbf{E} + \mathbf{v} \times \mathbf{B})$, the empirical formula to obtain the ion drift velocity now reads [243]:

$$\mathbf{v}_\mathrm{i} = \frac{\mu_0 p_0 / p_\mathrm{n}}{\sqrt{1 + a(|\mathbf{E} + \mathbf{v}_\mathrm{i} \times \mathbf{B}|/p_\mathrm{n})}} \left(\mathbf{E} + \mathbf{v}_\mathrm{i} \times \mathbf{B}\right) . \tag{6.4}$$

The experiments here have been conducted at $p_\mathrm{n} = 4\,\mathrm{Pa}$. This means that the angle with which the ions are deflected against the radial direction at 100 mT is roughly 14°. If the wave propagates with this angle, the error in determining the wavelength when using a vertical laser sheet is $(\cos(14°)^{-1} - 1) \approx 3\,\%$, which is acceptable.

Another aspect to consider is the influence of the magnetic field on the dispersion relation itself. As discussed above, the electron contribution to the dielectric function is negligible, so it remains to check if the magnetic induction has an influence on the ion or the dust susceptibility. Starting from the dispersion relation in the form Eq. (3.12), one gains a

System frequencies	Symbol	Value
ion-cyclotron frequency	ω_{ci}	2.4×10^5 rad/s
ion-plasma frequency	ω_{pi}	$2.1 - 6.6 \times 10^6$ rad/s
ion-neutral friction rate[a]	ν_{in}	9.4×10^5 rad/s
Doppler shift frequency	kv_i	$3.5 - 7 \times 10^6$ rad/s
Basic parameters		
ion density	n_i	$10^{14} - 10^{15}$ m^{-3}
pressure	p	4 Pa
wave number	k	$2 - 10$ krad/m
ion drift velocity	v_i	$1800 - 700$ m/s

[a]Reference [152].

Tab. 6.1: Parameters characterizing the magnetization of the plasma at 100 mT. These parameters comply with Eq. (6.5). The HALL parameter for ions $H_i = \omega_{ci}/\nu_{in}$ is 0.25 and $\beta_i = \omega_{ci}/\omega_{pi} \approx 0.1$.

simple condition for the validity of the unmagnetized dispersion relation:

$$\omega_{cj}^2 \ll (\mathrm{Re}(\omega) - \vec{k}\cdot\vec{v}_j)^2 - (\mathrm{Im}(\omega) + \nu_{jn})^2 \,, \tag{6.5}$$

which is valid for the case of a wave propagating perpendicularly to the direction of the magnetic field. Waves propagating in alignment with the magnetic field show the unmagnetized dispersion.

The dust-cyclotron frequency will certainly fulfill this condition, but for the ion-cyclotron frequency this is unsure. The wave frequency can be neglected. The DOPPLER shift and the friction rate are of importance. From Tab. 6.1 it can be seen that in the given situation, Eq. (6.5) is fulfilled by three orders of magnitude and the ions can be considered to be *unmagnetized* w.r.t. their susceptibility. The dispersion would be significantly altered by the magnetic field at an induction of about 2 T. Then, the squared ion-cyclotron frequency and the squared DOPPLER shift frequency would be equal.

As a demonstration how the increased magnetic induction changes the dispersion relation, calculations with Eq. (3.12) have been performed assuming parameters as in the right column of Tab. 2.1. The neutral pressure was set to $p_n = 4$ Pa. Fig. 6.10 shows no difference of $\mathrm{Re}(\omega)$ and $\mathrm{Im}(\omega)$ between 0 and 100 mT whereas for 2 or 3 T, the dispersion relation is significantly influenced.

An additional aspect of the applicability is the correct modelling of the charging currents in the magnetic field. This is important for the electron charging current since the electrons are significantly magnetized. In the given situation, only dense dust clouds are considered where the HAVNES parameter is much larger than unity. Therefore, the particle charge is determined by the ratio of ion to dust density. The exact formula of the charging

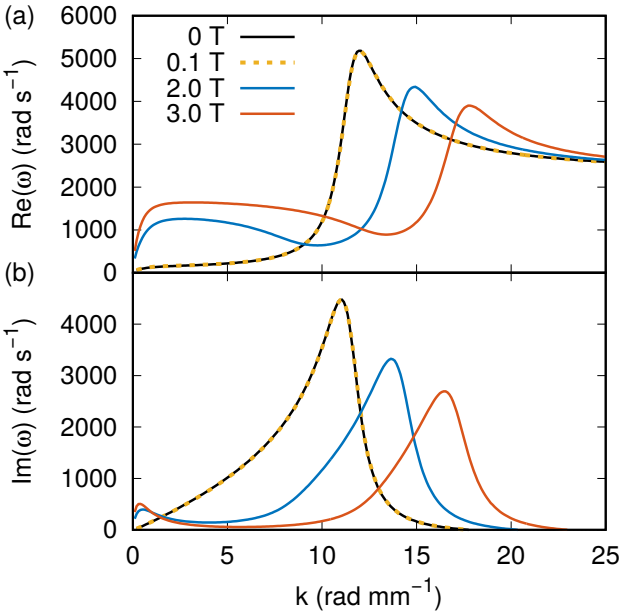

Fig. 6.10: Dispersion relations for different values of the magnetic induction for a wave propagating perpendicularly to the magnetic field direction and aligned with the ion flow. Depicted are (a) the real part of the frequency and (b) the imaginary part or the growth rate. The parameters are as in the right column of Tab. 2.1. A pressure of $p_n = 4\,\mathrm{Pa}$ is set.

currents has only a weak influence on the particle charge. Therefore, in the experiments presented below the unmagnetized DDW-D can be used without modification.

6.4.3 Results of the DDW-D

Since it is allowed to apply the DDW-D in its original form to the data obtained in the magnetized configuration, the results will be considered. The input parameters are summarized in Tab. 6.2. The following remarks will be given about the ion density, ion flow velocity, and the dust charge, see Fig. 6.11. The ion density is in the same range as found for the unmagnetized case in the previous chapter. The total values are slightly smaller, probably because the experiment has been conducted at a much lower pressure, which commonly results in a reduced plasma density.

Fixed parameters	Value
Electron temperature	5 eV
Dust temperature	0.025 eV
Ion temperature	0.025 eV
Neutral gas temperature	0.025 eV
Dust density	see Fig. 6.8
Dust radius	152 nm
Dust mass	1.91×10^{-17} kg
Neutral gas pressure	4 Pa

Tab. 6.2: Input parameters for the DDW-D.

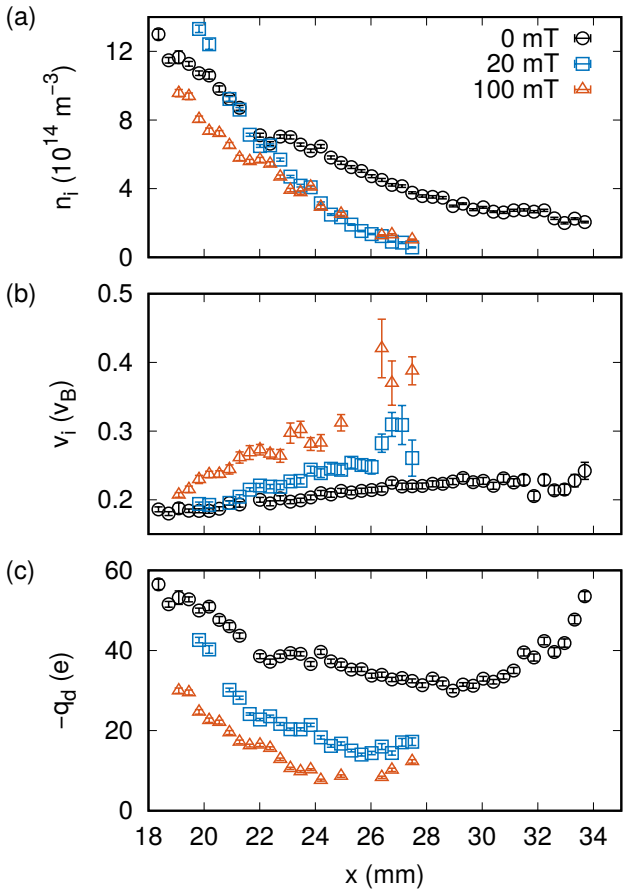

Fig. 6.11: Results of the DDW-D. (a) Ion density n_i, (b) ion flow velocity v_i in units of the BOHM velocity $v_B = \sqrt{k_B T_e / m_i}$ with an estimated electron temperature of $k_B T_e = 5\,\mathrm{eV}$, and (c) the dust charge q_d in units of the elementary charge. The error bars are calculated by error propagation of the errors in k and ω that follow directly from the distribution of the instantaneous wave properties. © 2018 American Physical Society [A.4]

The ion density reaches its maximum in the plasma center and not within the part of the dust cloud where the DDW can be analyzed. This is in contrast to the dust-density distribution, which has its maximum at about $x = 24\,\mathrm{mm}$. It is a plausible result for a magnetized plasma that its density drops at the electrode edge since it is horizontally confined by the magnetic field. This was confirmed by the LANGMUIR probe measurements [Fig. 6.1]. In the 20 mT and the 100 mT case, the ion density drops significantly below the values of the unmagnetized situation. At the plasma edge, there is no difference between the two magnetized cases, which shows that this effect can be seen as a consequence of the electron magnetization. The errors of the method for the ion density are generally small. The relative error increases at the electrode edge because the ion density becomes small there.

The differences between the magnetized and the unmagnetized situation also become visible in the ion flow velocity [Fig. 6.11 (b)]. In the unmagnetized case, the ions are drifting with about $0.2 \times v_B$. Their velocity increases slightly, beginning at values below $0.2 \times v_B$ in the center and increasing to $0.25 \times v_B$. With a magnetic field, the drift velocity has similar low values in the center, but increases higher towards the cloud edge. This effect is stronger with higher magnetic inductions. Here, the errors of the method are larger than in the unmagnetized situation. This can be attributed to the fact that

the waves close to the cloud edge have fluctuating properties. They propagate through a steep dust-density gradient and into a region with high electric fields. The instantaneous properties of the waves have a wide distribution and the DDW-D translates this uncertainty into a larger error of the wave parameters. The DDW-D is in good agreement with the LANGMUIR probe results in Fig. 6.2 (b) where it was found that the drift velocity increases significantly at the cloud edge if a magnetic field is present. The higher drift velocity can be attributed to an increased electric field, which explains why the dust cloud shows this strong confinement in the magnetized situations compared with the unmagnetized situation.
Finally, the resulting dust charges are considered [Fig. 6.11 (c)]. At first glance, it appears that the dust charge increases as the magnetic induction decreases. Since the ion density is similar in the plasma center for all considered cases, this cannot be the complete explanation. The ion density decreases at the cloud edge due to the increased plasma confinement. The dust density is increased there. Combining these two effects, a decrease of the dust charge as a consequence of the presence of the magnetic field is likely. But closer to the center, where the ion densities are almost equal in the three shown situations, the difference in the dust charge is a consequence of the timing of the experiment. In the following section, it will be shown that—as the magnetic inductions are set one after another, beginning at the largest magnetic induction—the system is losing particles. As less and less dust particles divide up the available electrons from the plasma, each single particle gets a higher charge.
Additionally, a general behavior of the dust charge becomes visible again: The dust charge is highest at the borders of the dust cloud. Over the spatial axis, it decreases reaching a minimum and then increases again. This behavior improves the confinement of the cloud as the particles being at the outside experience a stronger electric field force with their increased charge.

6.5 The Dust-Density Distribution

The dust-density distribution is recorded using a system of an LED illumination panel and a camera mounted with a telecentric lens. In order to calculate the 2D optical depth with this setup, it is necessary to take a dark image when all light sources are off. Additionally, one has to take an image of the LED panel without the presence of dust or plasma glow (reference image), one of the plasma glow without LED panel (plasma image), and one transmission image of the dust cloud (dust image). The plasma image must be taken because the telecentric lens is not protected with an intereference filter. Stray light from the laboratory can enter the chamber through the windows, which makes it necessary to take a reference image. Finally, the optical depth follows as:

$$\tau(x,z) = -\ln\left(\frac{\text{dust image} - \text{plasma image}}{\text{reference image} - \text{dark image}}\right). \tag{6.6}$$

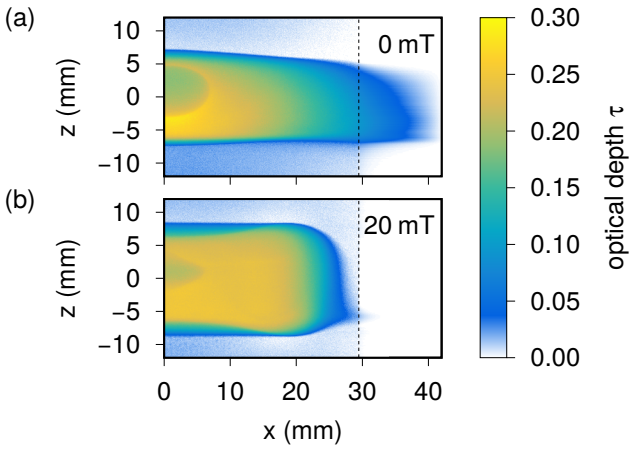

Fig. 6.12: Optical depth of the dust cloud in (a) the unmagnetized case. The dust cloud is extended over the field of view (FoV) of the telecentric lens. The data right of the vertical dashed line are extrapolated. (b) In the magnetized case, the particles are confined within the FoV, extrapolation is not necessary. © 2018 American Physical Society [A.4]

This rule is applied for every pixel. The optical depth τ of the dust cloud for two situations w/o a magnetic field is depicted in Fig. 6.12. The data of τ are not always sufficient to determine the density distribution of dust particles. This can happen when the dust cloud is extended over the FoV of the telecentric lens. In this case it becomes necessary to extrapolate the profile of τ. Here, this is done using an exponentially decaying function

$$f(x) = a \exp(-bx) + c\,. \tag{6.7}$$

The constants a, b, and c can then be determined by requiring that τ is continuously differentiable at the vertical dashed line in Fig. 6.12 and that it reaches zero at a position determined roughly from the DDW cam.
Application of the inverse ABEL transform leads to a 2D map of the dust-density distribution in Fig. 6.13. These data show that for the magnetized situation, depicted in Fig. 6.13 (a), the dust density has its maximum in front of the electrode edge. Towards the center, there is a gradual decrease of the density. The void is surrounded by a density minimum. The existence of a void points to an ion density maximum in the plasma center as it was found by the DDW-D. When the magnetic induction is decreased, the density maximum is shifted back from the electrode edge towards the void edge. The density maximum around the void is sometimes called a "cusp" and has been reported in Refs. [26, 71, 244]. While the magnetic induction is reduced, the dust cloud loses particles. The overall number of particles starts at 3 billion and drops to 1.4 billion particles.

The equilibrium of forces that creates this situation is difficult to explore due to the lack of diagnostics for the single particle behavior in this nanodusty situation. From earlier work with magnetized dusty plasmas, it is known that dust particles in magnetized plasmas are usually in rotation, either in a rotation about filaments [229] or about the central axis of the experiment [121, 233, 242, 243, 245–247]. This motion is driven by the deflection of the ions in the magnetic field or by momentum transfer from ions to the neutral gas [85]. In that case, the dust is swept with the rotating neutral gas.

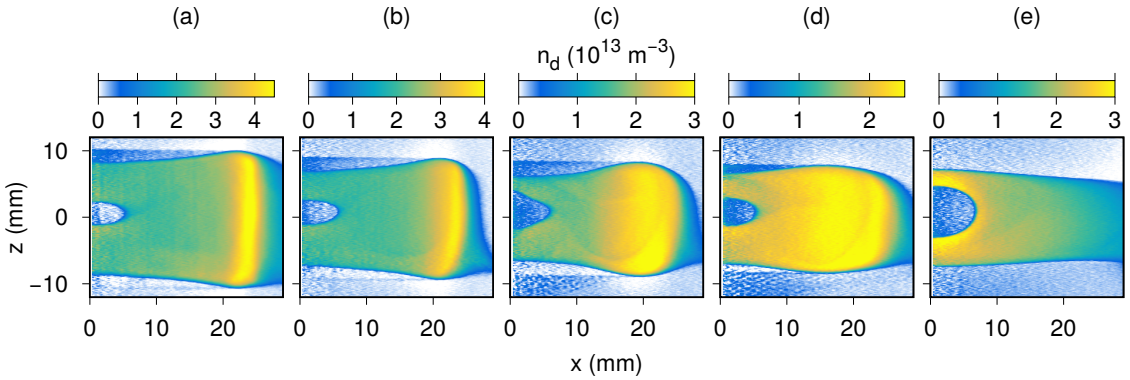

Fig. 6.13: Dust-density distribution for different values of the magnetic induction. By integration of the density in the complete volume, the total number of dust particles N_D can be calculated. The results are: (a) $B = 100\,\mathrm{mT}$, $N_D = 3 \times 10^9$, (b) $B = 50\,\mathrm{mT}$, $N_D = 1.9 \times 10^9$, (c) $B = 20\,\mathrm{mT}$, $N_D = 1.6 \times 10^9$, (d) $B = 10\,\mathrm{mT}$, $N_D = 1.6 \times 10^9$, and (e) $B = 0\,\mathrm{mT}$, $N_D = 1.4 \times 10^9$. © 2018 American Physical Society [A.4]

Due to the unusual density distribution of the dust, it is proposed that the nanodust particles are set into rotation by the rotating neutral gas. The rotation would impose a centrifugal force on the dust particles that could shift the density distribution to the edge of the electrode where the strong electric field balances this additional force. The direct momentum transfer by the ion drag on the dust is too small to create a significant rotation of the dust particles since the charge on the single particle is low. As we have much information about the system with the particle charges and the electric field strength from the DDW-D, it can be estimated, which rotation frequency would be necessary to cause the system to change its density distribution like this. This requires the centrifugal force to be at least 10 % of the confinement force F_E.
In the density maximum [Fig. 6.13 (a)], the single particle charge is roughly 10 elementary charges at an electric field of $450\,\mathrm{V\,m^{-1}}$. With the above-mentioned condition, this would require a rotation frequency of

$$f = \sqrt{\frac{0.1 F_E}{4\pi^2 m_d r}} \approx 2\,\mathrm{Hz}\,. \tag{6.8}$$

This rotation frequency seems high compared with rotation frequencies reported elsewhere, which are below 1 Hz [242, 247] or even below 0.1 Hz [243]. But these experiments have been performed at much higher pressure, e.g., Refs. [242, 243] or much lower magnetic induction [243]. With the low pressure and high magnetic induction given here, such a rotation frequency is realistic. The rotation of a dust cloud was also conjectured by observation of a plasma glow rotation [248]. But a direct proof of such a particle flow can only be provided by additional methods. This could be realized with laser DOPPLER anemometry. In unmagnetized nanodusty plasmas, such measurements have been possible [172].

6.6 Discussion

Within the scope of this work, a dense cloud of nanodust particles was confined in a magnetized plasma. The shape of the cloud is not conserved, but changes due to the modified plasma density and potential profile. The dust cloud was stable, i.e., there were no filamentary voids as observed in Fig. 6.5 (b) that disturb the system.
The dust cloud attains a hollow density profile when a magnetic field is present. It is proposed that the reason for this behavior is a rotation of the dust cloud that creates an outward-directed centrifugal force. The confining forces must be able to balance the centrifugal forces that appear when the cloud rotates. This is a limitation of the parameter space that is accessible in experiments. In the setup developed here, the confinement was strong due to the grounding of the FARADAY shield of the electrodes. The prospects of the results presented here go further.
The parameter space can probably be extended to even higher magnetic inductions if the particle confinement can be improved, e.g., by biasing the FARADAY shield. Here, the dust clouds were stable for 14 min. In superconducting magnets, this time would be needed to ramp the magnetic induction.
At a magnetic induction of about 2 T, the ion-cyclotron frequency starts to influence the DDW dispersion relation. Since large-scale magnetic devices can only be mounted on ground, not in space or on parabola flights, the preparation of nanodust clouds that are free of gravitational effects will be important for the understanding of the magnetized dusty plasma in future experiments.

7 Summary and Conclusions

In this thesis, I presented a new diagnostic method to determine the plasma parameters ion density, ion flow velocity, and dust charge in a dusty plasma with high spatial resolution by observation of self-excited dust-density waves (DDWs). This method fills a gap because classical diagnostics, e.g., electrostatic probes or emission spectroscopy, are not working in an environment with high dust density or they only provide this information with poor spatial resolution.

A reactive plasma is generated in a mixture of argon and acetylene to create a dust cloud, in which these DDWs can emerge. In this reactive environment almost monodisperse clouds with dust particles of radii between 150 and 200 nm were created resulting in a nanodusty plasma. By closure of the acetylene supply at different stages of the growth mechanism, the particle size can be chosen on purpose. The dust cloud in the pristine plasma exists for more than half an hour, which is enough time to study its properties. The experimental setup provides the dust size and number density in-situ by measurement of the polarization state of the scattered laser light and the extinction by the dust cloud. A camera records the wave activity in the central plane of the system.

The wave frequency and wave number change drastically over the observed area, since the wave adapts its properties to the local most unstable mode determined by the local plasma parameters. By combining the input parameters from the experiment with a hydrodynamic approach to model the system, the frequency and wave number in experiment and model can be matched by fitting the model parameters. This new method is named dust-density wave diagnostic (DDW-D). Its application to the nanodusty plasma led to the finding of low dust charges, while the ion density and the ion flow velocity are in a range common for low-temperature rf plasmas. Beside the considered nanodusty plasma, the DDW-D can be applied to many other dusty plasma situations.

Another configuration in which the DDW-D could be applied is a dusty magnetized plasma. Here, it was found that the dust-density distribution changes its center-peaked distribution to a hollow profile with an excentric peak. The DDW still propagates from the center to the outside revealing a center-peaked plasma potential. The DDW-D shows that the plasma keeps its center-peaked density profile in accordance with LANGMUIR probe measurements in the dust-free magnetized plasma.

The following conclusions can be drawn:

If the dust-density wave is unstable in a dusty plasma, its properties allow to determine the plasma parameters.

The DDW is a BUNEMAN-type instability, which is mainly excited by the interplay of dust inertia and ion flow [6]. The dispersion relation of the wave in a hydrodynamic model depends on all plasma parameters, but mainly on the dust plasma frequency, the ion flow velocity, and the ion density. The electron contribution can be neglected. Quasineutrality of the plasma and the floating condition of the dust reduce the number of unknown parameters in the dispersion relation. DDW frequency and wave number can be determined by application of the HILBERT transform to video data of the wave. For a dust cloud with known size and number density they allow to find a set of system parameters, ion density, ion flow velocity, and dust charge, that reproduces a dispersion relation with the most unstable mode being equal to the mode observed in the experiment.

The dust-density wave frequency and wave number are adapted to the local plasma parameters during the propagation of the wave.

The most unstable mode varies with the plasma parameters. Due to the self-excited nature of the DDW, the inhomogeneities in the plasma force the wave to change its properties during propagation. Earlier studies showed the dominance of the local most unstable mode by observing how the wave changes its propagation direction (oblique mode) while travelling into an area with increased ion flow velocity [125, 126]. Here, it was found that the wave parameters in the horizontal mid-plane of the experiment show strong gradients close to the void edge and they are almost constant far away from the void. The changing wave frequency means that wave crests have to disappear during the propagation of the wave. In accordance with the studies of MENZEL *et al.* [130] it was observed that this is organized with the merging of wave fronts, which becomes visible as defects in the wave field. The positions of the defects show a continuous spatial distribution. This behavior suggests that in the given situation the local most unstable mode defined by the local plasma parameters is dominating the wave properties. The system behaves like a chain of independent plasma cells, in which the parameters can be considered as constant.

The ion density profile in a nanodusty plasma is different from the dust-free plasma.

The ion-density profile for an unmagnetized low-temperature plasma usually has a negative curvature. The solution of the ambipolar diffusion problem in a system with spatially constant ionization rate is a bell shape. The DDW-D shows that in the nanodusty plasma the ion density profile has a positive curvature if enough dust is present. This finding is in accordance with Ref. [57] where the ion density profile was determined using a LANGMUIR probe in a microdusty plasma under microgravity conditions.

In a nanodusty plasma the dust charge of a single particle is reduced to a small fraction of its value in a dust-free plasma.

Nanodusty plasmas can easily produce dust number densities of $10^{13}\,\mathrm{m}^{-3}$. This is only two orders of magnitude lower than the ion density in a low-temperature rf plasma. Even if the complete positive ion charge was balanced by the negative dust charge, each dust particle could carry no more than 100 elementary charges. The DDW-D showed that even lower dust charges between 15 and 60 elementary charges reside on a single particle in the nanodusty plasma. The free-space OML value for the same situation would be 1,500 elementary charges for each dust particle. This HAVNES effect [100, 101, 249] is very strong in the nanodusty experiment whereas it is absent in most microdusty plasmas. Using a self-consistent model that takes into account the local floating condition of the dust particles, it follows that the free electron density in the plasma becomes two orders of magnitude smaller than the ion density. The electron charging current is reduced and so is the equilibrium dust charge.

The DDW amplitude increases when the wave propagates into a region of decreasing dust charge, dust density, and increasing ion density.

The considered system has the advantage that the inhomogeneous ion density leads to an inhomogeneous dust charge and dust-density distribution. The DDW propagates through the area with these varying parameters and adapts not only the frequency and the wave number, but also its amplitude. The DDW-D allows to follow the amplitude evolution w.r.t. the plasma parameters. The model function from Ref. [224] proved to represent the amplitude evolution in the experiment well. A deviation was only found in the area where the wave emerges from noise and changes its properties on a short spatial scale.

Dust clouds are better confined in a magnetized pristine plasma than in a magnetized reactive plasma.

Earlier studies have shown that reactive magnetized plasmas develop a hollow profile of negative ions [228]. With the experimental setup it was not possible to grow dust in the plasma bulk of the magnetized discharge. Therefore, an experiment schedule was created that utilizes the reactive plasma for dust production without a magnetic field. If it is ensured that the reactive species is completely removed before the magnetic field is turned on, then the dust stays in the plasma volume even when the magnetic field penetrates the system. Such a dust cloud stayed in the plasma for about 15 min, before the particles started to diminish in radius and the cloud became unstable due to the appearance of filaments in the plasma.

In magnetized plasmas, the dust-density distribution is changed due to a modified ion density and plasma potential distribution and probably due to the rotational motion of the dust cloud.

A vertical magnetic field improves the plasma confinement in the experiment. The DDW-D showed in agreement with LANGMUIR probe measurements in the dust-free discharge that the dust cloud can be trapped into the plasma cylinder by strong electric fields at the cylinder edge. The border of the cloud is comparable to the sheath edge. Outside of the inter-electrode space, the plasma density is low. The dust density is no longer peaked around the void but becomes hollow. A simple estimate of the centrifugal force leading to a shift of the density requires a rotation frequency in the range of 2 Hz. Such a rotation despite of the low single-particle charge can only be initiated by a rotation of the neutral gas [85]. The ion drag would not be strong enough for this effect.

8 Appendices

8.1 Equivalence of HAVNES Models

The equivalence of the CIM with the local HAVNES model can easily be seen. The particle floating potential can be rewritten as

$$\eta_{\text{fl.}} = \eta_{\text{f}} - \eta_{\text{c}} \,, \tag{8.1}$$

where η_{f} depicts the floating potential of the dust and η_{c} the plasma potential within the dust cloud. The electron density inside the cloud is given by

$$n_{\text{e}} = n_{\text{i}} \cdot \exp(-\eta_{\text{c}}) \qquad \Longrightarrow \qquad \zeta = \frac{n_{\text{e}}}{n_{\text{i}}} = \exp(-\eta_{\text{c}}) \,. \tag{8.2}$$

Note that the electron and ion densities are equal outside of the dust cloud. Substituting with Eqs. (8.1) and (8.2) in Eq. (2.27), one obtains

$$(\mu\tau)^{-1/2}[1 + \tau(\eta_{\text{f}} - \eta_{\text{c}})] - \exp(-\eta_{\text{f}}) = 0 \,, \tag{8.3}$$

which is equivalent to Eq. (2.25). Additionally, insertion in Eq. (2.28) leads to

$$\exp(-\eta_{\text{c}}) - 1 + P \cdot (\eta_{\text{f}} - \eta_{\text{c}}) = 0 \,, \tag{8.4}$$

which is equivalent to Eq. (2.26). Thus, the presented model is mathematically equivalent to the assumption of a constant ion density inside and outside the dust cloud.

8.2 Example Calculations for Magnetization of Plasma Components

The calculation of H and β requires some assumptions, which are adapted to the parameters at which experiments were conducted. The most important one is a neutral pressure of 4 Pa. The respective friction rates are 46×10^6 Hz (electrons), 9.4×10^5 Hz (ions), and 189 Hz (dust). For the dust, a mass of 1.9×10^{-17} kg and a charge of 33 elementary charges are assumed. For the plasma constituents, the following densities are used: $5.6 \times 10^{12}\,\mathrm{m}^{-3}$ (electrons), $1 \times 10^{15}\,\mathrm{m}^{-3}$ (ions), and $3 \times 10^{13}\,\mathrm{m}^{-3}$ (dust). Given these example values, the magnetic induction at which H or β reaches unity can be calculated. These are depicted in Tab. 8.1.

Species	B_H	B_β
Electrons	0.3 mT	0.8 mT
Ions	390 mT	2.7 T
Dust	680 T	8,000 T

Tab. 8.1: Magnetic inductions at which the respective plasma component gets magnetized in terms of H or β reaching unity. For a definition of H and β, see Eq. (6.1).

8.3 Photos of Dust Clouds

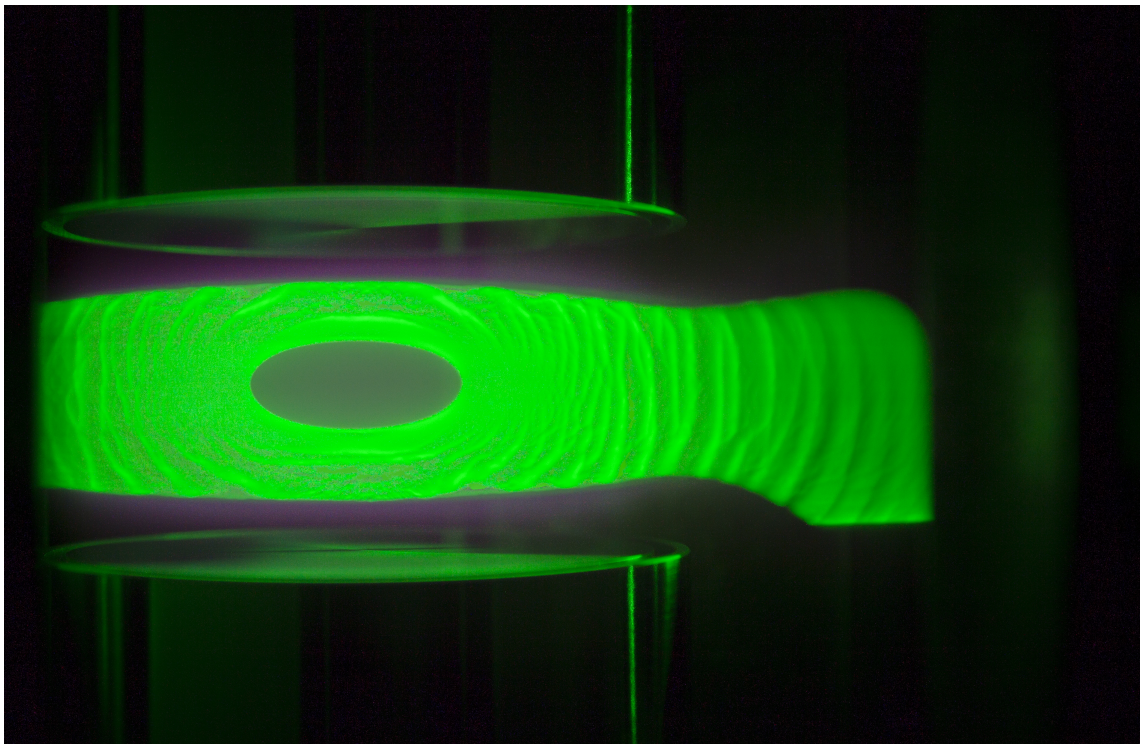

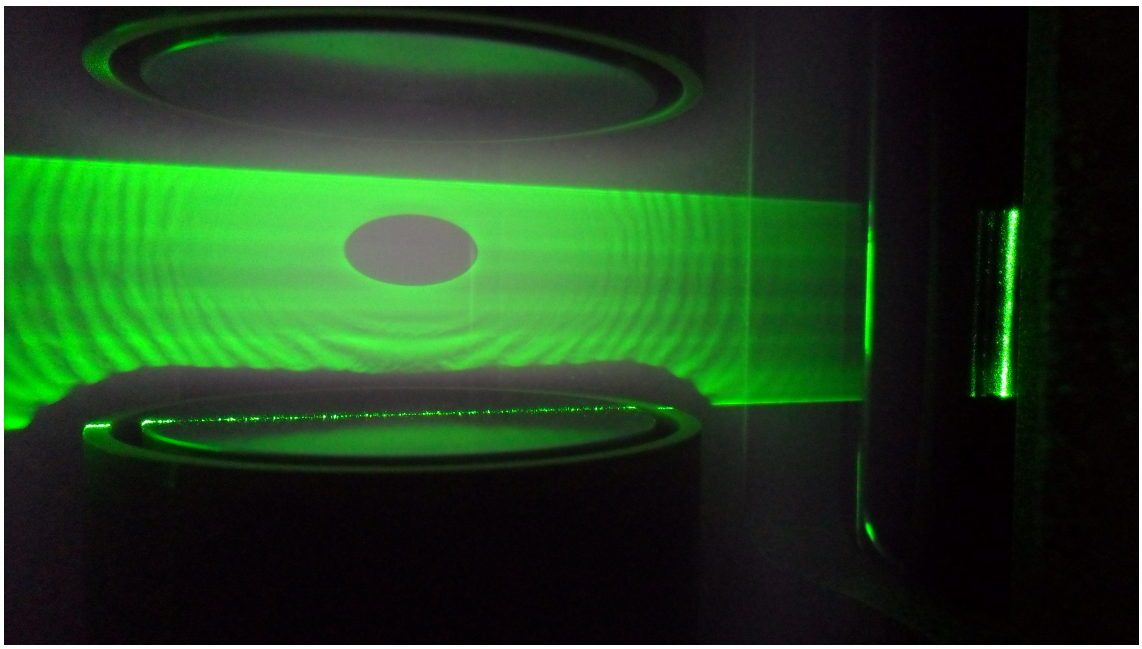

List of Publications

This thesis is based on the following original publications in peer-reviewed journals:

[A.1] B. TADSEN, F. GREINER, and A. PIEL, *Preparation of magnetized nanodusty plasmas in a radio frequency-driven parallel-plate reactor*, Phys. Plasmas **21**, 103704 (2014).

[A.2] B. TADSEN, F. GREINER, S. GROTH, and A. PIEL, *Self-excited dust-acoustic waves in an electron-depleted nanodusty plasma*, Phys. Plasmas **22**, 113701 (2015).

[A.3] B. TADSEN, F. GREINER, and A. PIEL, *On the amplitude of dust-density waves in inhomogeneous dusty plasmas*, Phys. Plasmas **24**, 033704 (2017).

[A.4] B. TADSEN, F. GREINER, and A. PIEL, *Probing a dusty magnetized plasma with self-excited dust-density waves*, Phys. Rev. E **97**, 033203 (2018).

Co-Authored Publications

[B.1] J. CARSTENSEN, F. HAASE, H. JUNG, B. TADSEN, S. GROTH, F. GREINER, and A. PIEL, *Probing the Plasma Sheath by the Continuous Mass Loss of Microparticles*, IEEE Trans. Plasma Sci. **41**, 764–768 (2013).

[B.2] S. GROTH, F. GREINER, B. TADSEN, and A. PIEL, *Kinetic Mie ellipsometry to determine the time-resolved particle growth in nanodusty plasmas*, J. Phys. D: Appl. Phys. **48**, 465203 (2015).

[B.3] C. KILLER, F. GREINER, S. GROTH, B. TADSEN, and A. MELZER, *Long-term spatio-temporal evolution of the dust distribution in dusty argon rf plasmas*, Plasma Sources Sci. Technol. **25**, 055004 (2016).

[B.4] F. GREINER, A. MELZER, B. TADSEN, et al., *Diagnostics and characterization of nanodust and nanodusty plasmas*, Eur. Phys. J. D **72**, 81 (2018).

Bibliography

[1] L. SPITZER, *Diffuse Matter in Space* (Interscience Publ., 1968).

[2] B. A. SMITH, L. SODERBLOM, R. BATSON, et al., *A New Look at the Saturn System: The Voyager 2 Images*, Science **215**, 504–537 (1982).

[3] C. K. GOERTZ, *Dusty plasmas in the solar system*, Rev. Geophys. **27**, 271–292 (1989).

[4] G. S. SELWYN, J. SINGH, and R. S. BENNETT, *In situ laser diagnostic studies of plasma-generated particulate contamination*, J. Vac. Sci. Technol. A **7**, 2758–2765 (1989).

[5] H. IKEZI, *Coulomb solid of small particles in plasmas*, Phys. Fluids **29**, 1764–1766 (1986).

[6] N. RAO, P. SHUKLA, and M. YU, *Dust-acoustic waves in dusty plasmas*, Planet. Space Sci. **38**, 543–546 (1990).

[7] J. H. CHU and L. I, *Direct observation of Coulomb crystals and liquids in strongly coupled rf dusty plasmas*, Phys. Rev. Lett. **72**, 4009–4012 (1994).

[8] H. THOMAS, G. E. MORFILL, V. DEMMEL, J. GOREE, B. FEUERBACHER, and D. MÖHLMANN, *Plasma Crystal: Coulomb Crystallization in a Dusty Plasma*, Phys. Rev. Lett. **73**, 652–655 (1994).

[9] Y. HAYASHI and K. TACHIBANA, *Observation of Coulomb-Crystal Formation from Carbon Particles Grown in a Methane Plasma*, Jpn. J. Appl. Phys. **33**, L804 (1994).

[10] A. BARKAN, R. L. MERLINO, and N. D'ANGELO, *Laboratory observation of the dust-acoustic wave mode*, Phys. Plasmas **2**, 3563–3565 (1995).

[11] O. ARP, D. BLOCK, A. PIEL, and A. MELZER, *Dust Coulomb Balls: Three-Dimensional Plasma Crystals*, Phys. Rev. Lett. **93**, 165004 (2004).

[12] A. PIEL, *Plasma crystals: experiments and simulation*, Plasma Phys. Control. Fusion **59**, 014001 (2017).

[13] G. PRABURAM and J. GOREE, *Experimental observation of very low-frequency macroscopic modes in a dusty plasma*, Phys. Plasmas **3**, 1212–1219 (1996).

[14] A. HOMANN, A. MELZER, S. PETERS, R. MADANI, and A. PIEL, *Laser-excited dust lattice waves in plasma crystals*, Phys. Lett. A **242**, 173–180 (1998).

[15] S. NUNOMURA, D. SAMSONOV, and J. GOREE, *Transverse Waves in a Two-Dimensional Screened-Coulomb Crystal (Dusty Plasma)*, Phys. Rev. Lett. **84**, 5141–5144 (2000).

[16] A. MELZER, M. KLINDWORTH, and A. PIEL, *Normal Modes of 2D Finite Clusters in Complex Plasmas*, Phys. Rev. Lett. **87**, 115002 (2001).

[17] J. SCHABLINSKI and D. BLOCK, *Selective mode excitation in finite size plasma crystals by diffusely reflected laser light*, Phys. Plasmas **22**, 023703 (2015).

[18] A. MELZER, A. HOMANN, and A. PIEL, *Experimental investigation of the melting transition of the plasma crystal*, Phys. Rev. E **53**, 2757–2766 (1996).

[19] H. M. THOMAS and G. E. MORFILL, *Melting Dynamics of a plasma crystal*, Nature **379**, 806–809 (1996).

[20] V. A. SCHWEIGERT, I. V. SCHWEIGERT, A. MELZER, A. HOMANN, and A. PIEL, *Plasma Crystal Melting: A Nonequilibrium Phase Transition*, Phys. Rev. Lett. **80**, 5345–5348 (1998).

[21] M. MULSOW and A. MELZER, *Experimental determination of phase transitions by means of configurational entropies in finite Yukawa balls*, Phys. Rev. E **96**, 053202 (2017).

[22] S. PETERS, A. HOMANN, A. MELZER, and A. PIEL, *Measurement of dust particle shielding in a plasma from oscillations of a linear chain*, Phys. Lett. A **223**, 389–393 (1996).

[23] M. BONITZ, D. BLOCK, O. ARP, V. GOLUBNYCHIY, H. BAUMGARTNER, P. LUDWIG, A. PIEL, and A. FILINOV, *Structural Properties of Screened Coulomb Balls*, Phys. Rev. Lett. **96**, 075001 (2006).

[24] Y. HAYASHI and K. TACHIBANA, *Analysis of Spherical Carbon Particle Growth in Methane Plasma by Mie-Scattering Ellipsometry*, Jpn. J. Appl. Phys. **33**, 4208–4211 (1994).

[25] M. KROLL, S. HARMS, D. BLOCK, and A. PIEL, *Digital in-line holography of dusty plasmas*, Phys. Plasmas **15**, 063703 (2008).

[26] C. KILLER, M. HIMPEL, and A. MELZER, *Computer tomography of large dust clouds in complex plasmas*, Rev. Sci. Instrum. **85**, 103711 (2014).

[27] A. PIEL, *Plasma Physics. An Introduction to Laboratory, Space and Fusion Plasmas* (Springer, Berlin Heidelberg, 2010).

[28] V. FORTOV and G. MORFILL, *Complex and dusty plasmas: from laboratory to space*, 2010.

[29] M. BONITZ, N. HORING, and P. LUDWIG, eds., *Introduction to Complex Plasmas*, Springer Series on Atomic, Optical and Plasma Physics (Springer-Verlag Berlin Heidelberg, 2010).

[30] N. TSYTOVICH, G. MORFILL, S. VLADIMIROV, and H. THOMAS, *Elementary Physics of Complex Plasmas* (Springer, 2008).

[31] A. MELZER and J. GOREE, *Fundamentals of Dusty Plasmas*, in *Low Temperature Plasmas*, edited by R. HIPPLER, H. KERSTEN, M. SCHMIDT, and K. H. SCHOENBACH (Wiley-VCH, Weinheim, 2008) Chap. 6, pp. 129–174.

[32] P. K. SHUKLA and A. A. MAMUN, *Introduction to Dusty Plasma Physics*, Plasma Phys. Control. Fusion **44**, 395 (2002).

[33] L. BOUFENDI, W. STOFFELS, and E. STOFFELS, *Dusty Plasmas. Physics, Chemistry and Technological Impacts on Plasma Processing*, edited by A. BOUCHOULE (Wiley-VCH, 1999), pp. 181–303.

[34] M. BONITZ, C. HENNING, and D. BLOCK, *Complex plasmas: a laboratory for strong correlations*, Rep. Prog. Phys. **73**, 066501 (2010).

[35] P. K. SHUKLA and B. ELIASSON, *Colloquium: Fundamentals of dust-plasma interactions*, Rev. Mod. Phys. **81**, 25–44 (2009).

[36] G. E. MORFILL and A. V. IVLEV, *Complex plasmas: An interdisciplinary research field*, Rev. Mod. Phys. **81**, 1353–1404 (2009).

[37] A. PIEL, O. ARP, D. BLOCK, I. PILCH, T. TROTTENBERG, S. KÄDING, A. MELZER, H. BAUMGARTNER, C. HENNING, and M. BONITZ, *Complex plasmas: forces and dynamical behaviour*, Plasma Phys. Control. Fusion **50**, 124003 (2008).

[38] R. MERLINO and J. GOREE, *Dusty Plasmas in the Laboratory, Industry, and Space*, Phys. Today **57**, 32–38 (2004).

[39] A. PIEL and A. MELZER, *Dynamical processes in complex plasmas*, Plasma Phys. Control. Fusion **44**, R1 (2002).

[40] D. A. MENDIS, *Progress in the study of dusty plasmas*, Plasma Sources Sci. Technol. **11**, A219 (2002).

[41] P. K. SHUKLA, *A survey of dusty plasma physics*, Phys. Plasmas **8**, 1791–1803 (2001).

[42] C. HOLLENSTEIN, *The physics and chemistry of dusty plasmas*, Plasma Phys. Control. Fusion **42**, R93 (2000).

[43] A. MELZER, T. TROTTENBERG, and A. PIEL, *Experimental determination of the charge on dust particles forming Coulomb lattices*, Phys. Lett. A **191**, 301–308 (1994).

[44] A. MELZER, S. NUNOMURA, D. SAMSONOV, Z. W. MA, and J. GOREE, *Laser-excited Mach cones in a dusty plasma crystal*, Phys. Rev. E **62**, 4162–4176 (2000).

[45] S. RATYNSKAIA, S. KHRAPAK, A. ZOBNIN, et al., *Experimental Determination of Dust-Particle Charge in a Discharge Plasma at Elevated Pressures*, Phys. Rev. Lett. **93**, 085001 (2004).

[46] J. CARSTENSEN, F. GREINER, and A. PIEL, *Determination of dust grain charge and screening lengths in the plasma sheath by means of a controlled cluster rotation*, Phys. Plasmas **17**, 083703 (2010).

[47] J. BECKERS, T. OCKENGA, M. WOLTER, W. W. STOFFELS, J. van DIJK, H. KERSTEN, and G. M. W. KROESEN, *Microparticles in a Collisional Rf Plasma Sheath under Hypergravity Conditions as Probes for the Electric Field Strength and the Particle Charge*, Phys. Rev. Lett. **106**, 115002 (2011).

[48] R. L. HEINISCH, F. X. BRONOLD, and H. FEHSKE, *Mie Scattering by a Charged Dielectric Particle*, Phys. Rev. Lett. **109**, 243903 (2012).

[49] M. S. BARNES, J. H. KELLER, J. C. FORSTER, J. A. O'NEILL, and D. K. COULTAS, *Transport of dust particles in glow-discharge plasmas*, Phys. Rev. Lett. **68**, 313–316 (1992).

[50] S. A. KHRAPAK, A. V. IVLEV, G. E. MORFILL, and H. M. THOMAS, *Ion drag force in complex plasmas*, Phys. Rev. E **66**, 046414 (2002).

[51] S. A. KHRAPAK, A. V. IVLEV, S. K. ZHDANOV, and G. E. MORFILL, *Hybrid approach to the ion drag force*, Phys. Plasmas **12**, 042308 (2005).

[52] I. H. HUTCHINSON, *Ion collection by a sphere in a flowing plasma: 3. Floating potential and drag force*, Plasma Phys. Control. Fusion **47**, 71 (2005).

[53] M. HIRT, D. BLOCK, and A. PIEL, *Measurement of the ion drag force on free falling microspheres in a plasma*, Phys. Plasmas **11**, 5690–5696 (2004).

[54] V. NOSENKO, R. FISHER, R. MERLINO, S. KHRAPAK, G. MORFILL, and K. AVINASH, *Measurement of the ion drag force in a collisionless plasma with strong ion-grain coupling*, Phys. Plasmas **14**, 103702 (2007).

[55] J. GOREE, G. E. MORFILL, V. N. TSYTOVICH, and S. V. VLADIMIROV, *Theory of dust voids in plasmas*, Phys. Rev. E **59**, 7055–7067 (1999).

[56] E. THOMAS, K. AVINASH, and R. L. MERLINO, *Probe induced voids in a dusty plasma*, Phys. Plasmas **11**, 1770–1774 (2004).

[57] M. KLINDWORTH, O. ARP, and A. PIEL, *Langmuir probe system for dusty plasmas under microgravity*, Rev. Sci. Instrum. **78**, 033502 (2007).

[58] A. M. LIPAEV, S. A. KHRAPAK, V. I. MOLOTKOV, et al., *Void Closure in Complex Plasmas under Microgravity Conditions*, Phys. Rev. Lett. **98**, 265006 (2007).

[59] V. LAND and W. J. GOEDHEER, *The plasma inside a dust free void: hotter, denser, or both?*, New J. Phys. **9**, 246 (2007).

[60] V. LAND and W. J. GOEDHEER, *How to make large, void-free dust clusters in dusty plasma under micro-gravity*, New J. Phys. **10**, 123028 (2008).

[61] A. BOUCHOULE, *Dusty Plasmas. Physics, Chemistry and Technological Impacts on Plasma Processing*, edited by A. BOUCHOULE (Wiley-VCH, 1999).

[62] J. BENEDIKT, *Plasma-chemical reactions: low pressure acetylene plasmas*, J. Phys. D: Appl. Phys. **43**, 043001 (2010).

[63] J. WINTER, *Dust: A new challenge in nuclear fusion research?*, Phys. Plasmas **7**, 3862–3866 (2000).

[64] D. L. RUDAKOV, J. H. YU, J. A. BOEDO, et al., *Dust measurements in tokamaks (invited)*, Rev. Sci. Instrum. **79**, 10F303 (2008).

[65] S. I. KRASHENINNIKOV, R. D. SMIRNOV, and D. L. RUDAKOV, *Dust in magnetic fusion devices*, Plasma Phys. Control. Fusion **53**, 083001 (2011).

[66] G. E. MORFILL, H. M. THOMAS, U. KONOPKA, H. ROTHERMEL, M. ZUZIC, A. IVLEV, and J. GOREE, *Condensed Plasmas under Microgravity*, Phys. Rev. Lett. **83**, 1598–1601 (1999).

[67] C. KILLER, T. BOCKWOLDT, S. SCHÜTT, M. HIMPEL, A. MELZER, and A. PIEL, *Phase Separation of Binary Charged Particle Systems with Small Size Disparities using a Dusty Plasma*, Phys. Rev. Lett. **116**, 115002 (2016).

[68] A. P. NEFEDOV, G. E. MORFILL, V. E. FORTOV, et al., *PKE-Nefedov: plasma crystal experiments on the International Space Station*, New J. Phys. **5**, 33 (2003).

[69] H. M. THOMAS, G. E. MORFILL, V. E. FORTOV, et al., *Complex plasma laboratory PK-3 Plus on the International Space Station*, New J. Phys. **10**, 033036 (2008).

[70] M. Y. PUSTYLNIK, M. A. FINK, V. NOSENKO, et al., *Plasmakristall-4: New complex (dusty) plasma laboratory on board the International Space Station*, Rev. Sci. Instrum. **87**, 093505 (2016).

[71] H. ROTHERMEL, T. HAGL, G. E. MORFILL, M. H. THOMA, and H. M. THOMAS, *Gravity Compensation in Complex Plasmas by Application of a Temperature Gradient*, Phys. Rev. Lett. **89**, 175001 (2002).

[72] G. M. JELLUM, J. E. DAUGHERTY, and D. B. GRAVES, *Particle thermophoresis in low pressure glow discharges*, J. Appl. Phys. **69**, 6923–6934 (1991).

[73] R. L. MERLINO, *25 years of dust acoustic waves*, J. Plasma Phys. **80**, 773–786 (2014).

[74] J. H. CHU, J.-B. DU, and L. I, *Coulomb solids and low-frequency fluctuations in RF dusty plasmas*, J. Phys. D: Appl. Phys. **27**, 296 (1994).

[75] N. D'ANGELO, *Coulomb solids and low-frequency fluctuations in RF dusty plasmas*, J. Phys. D: Appl. Phys. **28**, 1009 (1995).

[76] U. KORTSHAGEN, *On the use of dust plasma acoustic waves for the diagnostic of nanometer-sized contaminant particles in plasmas*, Appl. Phys. Lett. **71**, 208 (1997).

[77] N. HAYASHI, *Observation of submicron dust particles trapped in a diffused region of a low pressure radio frequency plasma*, Phys. Plasmas **8**, 3051–3057 (2001).

[78] V. E. FORTOV, A. G. KHRAPAK, S. A. KHRAPAK, V. I. MOLOTKOV, A. P. NEFEDOV, O. F. PETROV, and V. M. TORCHINSKY, *Mechanism of dust-acoustic instability in a direct current glow discharge plasma*, Phys. Plasmas **7**, 1374–1380 (2000).

[79] S. RATYNSKAIA, M. KRETSCHMER, S. KHRAPAK, R. QUINN, M. THOMA, G. MORFILL, A. ZOBNIN, A. USACHEV, O. PETROV, and V. FORTOV, *Dust mode in collisionally dominated complex plasmas with particle drift*, IEEE Trans. Plasma Sci. **32**, 613–616 (2004).

[80] A. BOUCHOULE and L. BOUFENDI, *High concentration effects in dusty plasmas*, Plasma Sources Sci. Technol. **3**, 292–301 (1994).

[81] T. WEGNER, A. M. HINZ, F. FAUPEL, T. STRUNSKUS, H. KERSTEN, and J. MEICHSNER, *Influence of nanoparticle formation on discharge properties in argon-acetylene capacitively coupled radio frequency plasmas*, Appl. Phys. Lett. **108**, 063108 (2016).

[82] C. KILLER, T. WEGNER, A. MELZER, and J. MEICHSNER, *Influence of dust particles on the bulk electron density in radio frequency plasmas measured by microwave interferometry*, Phys. Plasmas **22**, 123702 (2015).

[83] I. GOERTZ, F. GREINER, and A. PIEL, *Effects of charge depletion in dusty plasmas*, Phys. Plasmas **18**, 013703 (2011).

[84] N. BILIK, R. ANTHONY, B. A. MERRITT, E. S. AYDIL, and U. R. KORTSHAGEN, *Langmuir probe measurements of electron energy probability functions in dusty plasmas*, J. Phys. D: Appl. Phys. **48**, 105204 (2015).

[85] J. CARSTENSEN, F. GREINER, L.-J. HOU, H. MAURER, and A. PIEL, *Effect of neutral gas motion on the rotation of dust clusters in an axial magnetic field*, Phys. Plasmas **16**, 013702 (2009).

[86] T. OTT and M. BONITZ, *Diffusion in a Strongly Coupled Magnetized Plasma*, Phys. Rev. Lett. **107**, 135003 (2011).

[87] E. THOMAS JR, R. L. MERLINO, and M. ROSENBERG, *Magnetized dusty plasmas: the next frontier for complex plasma research*, Plasma Phys. Control. Fusion **54**, 124034 (2012).

[88] T. OTT, H. LÖWEN, and M. BONITZ, *Magnetic Field Blocks Two-Dimensional Crystallization in Strongly Coupled Plasmas*, Phys. Rev. Lett. **111**, 065001 (2013).

[89] M. ROSENBERG, *Beam cyclotron instability in a dusty plasma*, Phys. Scr. **89**, 085601 (2014).

[90] A. MELZER, *Introduction to colloidal (dusty) plasmas*, Lecture Notes, 2016.

[91] I. H. HUTCHINSON, *Collisionless ion drag force on a spherical grain*, Plasma Phys. Control. Fusion **48**, 185 (2006).

[92] O. VAULINA, S. KHRAPAK, and G. MORFILL, *Universal scaling in complex (dusty) plasmas*, Phys. Rev. E **66**, 016404 (2002).

[93] S. HAMAGUCHI, R. T. FAROUKI, and D. H. E. DUBIN, *Triple point of Yukawa systems*, Phys. Rev. E **56**, 4671–4682 (1997).

[94] R. T. FAROUKI and S. HAMAGUCHI, *Thermodynamics of strongly-coupled Yukawa systems near the one-component-plasma limit. II. Molecular dynamics simulations*, J. Chem. Phys. **101**, 9885–9893 (1994).

[95] H. M. MOTT-SMITH and I. LANGMUIR, *The Theory of Collectors in Gaseous Discharges*, Phys. Rev. **28**, 727–763 (1926).

[96] J. E. ALLEN, *Probe theory – the orbital motion approach*, Phys. Scr. **45**, 497 (1992).

[97] E. C. WHIPPLE, *Potentials of surfaces in space*, Rep. Prog. Phys. **44**, 1197 (1981).

[98] B. WALCH, M. HORÁNYI, and S. ROBERTSON, *Charging of Dust Grains in Plasma with Energetic Electrons*, Phys. Rev. Lett. **75**, 838–841 (1995).

[99] C. K. GOERTZ and W.-H. IP, *Limitation of electrostatic charging of dust particles in a plasma*, Geophys. Res. Lett. **11**, 349–352 (1984).

[100] O. HAVNES, G. E. MORFILL, and C. K. GOERTZ, *Plasma potential and grain charges in a dust cloud embedded in a plasma*, J. Geophys. Res. **89**, 10999–11003 (1984).

[101] O. HAVNES, C. K. GOERTZ, G. E. MORFILL, E. GRÜN, and W. IP, *Dust charges, cloud potential, and instabilities in a dust cloud embedded in a plasma*, J. Geophys. Res. **92**, 2281–2287 (1987).

[102] A. BARKAN, N. D'ANGELO, and R. L. MERLINO, *Charging of Dust Grains in a Plasma*, Phys. Rev. Lett. **73**, 3093–3096 (1994).

[103] Y. S. CHOU, L. TALBOT, and D. R. WILLIS, *Kinetic Theory of a Spherical Electrostatic Probe in a Stationary Plasma*, Phys. Fluids **9**, 2150 (1966).

[104] Z. ZAKRZEWSKI and T. KOPICZYNSKI, *Effect of collisions on positive ion collection by a cylindrical Langmuir probe*, Plasma Phys. **16**, 1195–1198 (1974).

[105] M. TICHÝ, M. SICHA, P. DAVID, and T. DAVID, *A Collisional Model of the Positive Ion Collection by a Cylindrical Langmuir Probe*, Contrib. Plasma Phys. **34**, 59–68 (1994).

[106] S. A. KHRAPAK, S. V. RATYNSKAIA, A. V. ZOBNIN, et al., *Particle charge in the bulk of gas discharges*, Phys. Rev. E **72**, 016406 (2005).

[107] M. LAMPE, R. GOSWAMI, Z. STERNOVSKY, S. ROBERTSON, V. GAVRISHCHAKA, G. GANGULI, and G. JOYCE, *Trapped ion effect on shielding, current flow, and charging of a small object in a plasma*, Phys. Plasmas **10**, 1500–1513 (2003).

[108] A. PIEL and C. SCHMIDT, *Dust charging and charge fluctuations in a weakly collisional radio-frequency sheath at low pressure*, Phys. Plasmas **22**, 053701 (2015).

[109] R. HEGERBERG, M. T. ELFORD, and H. R. SKULLERUD, *The cross section for symmetric charge exchange of Ne + in Ne and Ar + in Ar at low energies*, J. Phys. B: At. Mol. Phys. **15**, 797 (1982).

[110] N. KOBAYASHI, *Low Energy Ion-Neutral Reactions. VI. $Ar^+ + Ar$, $N_2^+ + N_2$, $O_2^+ + O_2$ and $CO^+ + CO$*, J. Phys. Soc. Jpn. **38**, 519–523 (1975).

[111] A. C. FERRARI, A. LIBASSI, B. K. TANNER, V. STOLOJAN, J. YUAN, L. M. BROWN, S. E. RODIL, B. KLEINSORGE, and J. ROBERTSON, *Density, sp^3 fraction, and cross-sectional structure of amorphous carbon films determined by x-ray reflectivity and electron energy-loss spectroscopy*, Phys. Rev. B **62**, 11089–11103 (2000).

[112] P. S. EPSTEIN, *On the Resistance Experienced by Spheres in their Motion through Gases*, Phys. Rev. **23**, 710–733 (1924).

[113] C. KILLER, M. MULSOW, and A. MELZER, *Spatio-temporal evolution of the dust particle size distribution in dusty argon rf plasmas*, Plasma Sources Sci. Technol. **24**, 025029 (2015).

[114] K. R. SÜTTERLIN, A. WYSOCKI, A. V. IVLEV, et al., *Dynamics of Lane Formation in Driven Binary Complex Plasmas*, Phys. Rev. Lett. **102**, 085003 (2009).

[115] I. PILCH and F. GREINER, *Diagnostics of void expansion during cyclic growth and formation of layered nanoparticle clouds*, J. Appl. Phys. **121**, 113302 (2017).

[116] O. BUNEMAN, *Instability, Turbulence, and Conductivity in Current-Carrying Plasma*, Phys. Rev. Lett. **1**, 8–9 (1958).

[117] O. BUNEMAN, *Instability, Turbulence, and Conductivity in Current-Carrying Plasma.*, Phys. Rev. Lett. **1**, 119 (1958).

[118] M. ROSENBERG, *Ion-dust streaming instability in processing plasmas*, J. Vac. Sci. Technol. A **14**, 631–633 (1996).

[119] T. TROTTENBERG, D. BLOCK, and A. PIEL, *Dust confinement and dust-acoustic waves in weakly magnetized anodic plasmas*, Phys. Plasmas **13**, 042105 (2006).

[120] C. THOMPSON, A. BARKAN, N. D'ANGELO, and R. L. MERLINO, *Dust acoustic waves in a direct current glow discharge*, Phys. Plasmas **4**, 2331–2335 (1997).

[121] I. PILCH, A. PIEL, T. TROTTENBERG, and M. E. KOEPKE, *Dynamics of small dust clouds trapped in a magnetized anodic plasma*, Phys. Plasmas **14**, 123704 (2007).

[122] S. KHRAPAK, D. SAMSONOV, G. MORFILL, et al., *Compressional waves in complex (dusty) plasmas under microgravity conditions*, Phys. Plasmas **10**, 1–4 (2003).

[123] V. V. YAROSHENKO, B. M. ANNARATONE, S. A. KHRAPAK, et al., *Electrostatic modes in collisional complex plasmas under microgravity conditions*, Phys. Rev. E **69**, 066401 (2004).

[124] S. V. ANNIBALDI, A. V. IVLEV, U. KONOPKA, S. RATYNSKAIA, H. M. THOMAS, G. E. MORFILL, A. M. LIPAEV, V. I. MOLOTKOV, O. F. PETROV, and V. E. FORTOV, *Dust-acoustic dispersion relation in three-dimensional complex plasmas under microgravity*, New J. Phys. **9**, 327 (2007).

[125] A. PIEL, M. KLINDWORTH, O. ARP, A. MELZER, and M. WOLTER, *Obliquely Propagating Dust-Density Plasma Waves in the Presence of an Ion Beam*, Phys. Rev. Lett. **97**, 205009 (2006).

[126] A. PIEL, O. ARP, M. KLINDWORTH, and A. MELZER, *Obliquely propagating dust-density waves*, Phys. Rev. E **77**, 026407 (2008).

[127] M. SCHWABE, S. K. ZHDANOV, H. M. THOMAS, A. V. IVLEV, M. RUBIN-ZUZIC, G. E. MORFILL, V. I. MOLOTKOV, A. M. LIPAEV, V. E. FORTOV, and T. REITER, *Nonlinear waves externally excited in a complex plasma under microgravity conditions*, New J. Phys. **10**, 033037 (2008).

[128] I. PILCH, T. REICHSTEIN, and A. PIEL, *Synchronization of dust density waves in anodic plasmas*, Phys. Plasmas **16**, 123709 (2009).

[129] W. D. S. RUHUNUSIRI and J. GOREE, *Synchronization mechanism and Arnold tongues for dust density waves*, Phys. Rev. E **85**, 046401 (2012).

[130] K. O. MENZEL, O. ARP, and A. PIEL, *Spatial Frequency Clustering in Nonlinear Dust-Density Waves*, Phys. Rev. Lett. **104**, 235002 (2010).

[131] E. THOMAS, *Measurements of spatially growing dust acoustic waves in a dc glow discharge plasma*, Phys. Plasmas **13**, 042107 (2006).

[132] A. V. ZOBNIN, A. D. USACHEV, O. F. PETROV, and V. E. FORTOV, *Dust-acoustic instability in an inductive gas-discharge plasma*, J. Exp. Theor. Phys. **95**, 429–439 (2002).

[133] T. M. FLANAGAN and J. GOREE, *Observation of the spatial growth of self-excited dust-density waves*, Phys. Plasmas **17**, 123702 (2010).

[134] J. R. HEINRICH, S.-H. KIM, J. K. MEYER, and R. L. MERLINO, *Experimental quiescent drifting dusty plasmas and temporal dust acoustic wave growth*, Phys. Plasmas **18**, 113706 (2011).

[135] J. PRAMANIK, B. VEERESHA, G. PRASAD, A. SEN, and P. KAW, *Experimental observation of dust-acoustic wave turbulence*, Phys. Lett. A **312**, 84–90 (2003).

[136] T. M. FLANAGAN and J. GOREE, *Development of nonlinearity in a growing self-excited dust-density wave*, Phys. Plasmas **18**, 013705 (2011).

[137] Y.-Y. TSAI, M.-C. CHANG, and L. I, *Observation of multifractal intermittent dust-acoustic-wave turbulence*, Phys. Rev. E **86**, 045402 (2012).

[138] J. HEINRICH, S.-H. KIM, and R. MERLINO, *Laboratory Observations of Self-Excited Dust Acoustic Shocks*, Phys. Rev. Lett. **103**, 115002 (2009).

[139] R. L. MERLINO, J. R. HEINRICH, S.-H. KIM, and J. K. MEYER, *Dusty plasmas: experiments on nonlinear dust acoustic waves, shocks and structures*, Plasma Phys. Control. Fusion **54**, 124014 (2012).

[140] C.-T. LIAO, L.-W. TENG, C.-Y. TSAI, C.-W. IO, and L. I, *Lagrangian-Eulerian Micromotion and Wave Heating in Nonlinear Self-Excited Dust-Acoustic Waves*, Phys. Rev. Lett. **100**, 185004 (2008).

[141] C.-T. LIAO, L.-W. TENG, C.-Y. TSAI, C.-W. IO, and L. I, *Erratum: Lagrangian-Eulerian Micromotion and Wave Heating in Nonlinear Self-Excited Dust-Acoustic Waves [Phys. Rev. Lett. 100, 185004 (2008)]*, Phys. Rev. Lett. **103**, 089903 (2009).

[142] E. T. JR., R. FISHER, and R. L. MERLINO, *Observations of dust acoustic waves driven at high frequencies: Finite dust temperature effects and wave interference*, Phys. Plasmas **14**, 123701 (2007).

[143] J. D. WILLIAMS and E. THOMAS, *Measurement of the kinetic dust temperature of a weakly coupled dusty plasma*, Phys. Plasmas **14**, 063702 (2007).

[144] J. D. WILLIAMS and E. K. SNIPES, *Measurements of the Dust Temperature in the Dispersion Relation of the Dust Acoustic Wave*, IEEE Trans. Plasma Sci. **38**, 847–851 (2010).

[145] M. HIMPEL, C. KILLER, B. BUTTENSCHÖN, and A. MELZER, *Three-dimensional single particle tracking in dense dust clouds by stereoscopy of fluorescent particles*, Phys. Plasmas **19**, 123704 (2012).

[146] L.-W. TENG, M.-C. CHANG, Y.-P. TSENG, and L. I, *Wave-Particle Dynamics of Wave Breaking in the Self-Excited Dust Acoustic Wave*, Phys. Rev. Lett. **103**, 245005 (2009).

[147] C.-R. DU, H. M. THOMAS, A. V. IVLEV, U. KONOPKA, and G. E. MORFILL, *Agglomeration of microparticles in complex plasmas*, Phys. Plasmas **17**, 113710 (2010).

[148] S. DAP, D. LACROIX, R. HUGON, L. de POUCQUES, J.-L. BRIANCON, and J. BOUGDIRA, *Cluster Agglomeration Induced by Dust-Density Waves in Complex Plasmas*, Phys. Rev. Lett. **109**, 245002 (2012).

[149] J. B. PIEPER and J. GOREE, *Dispersion of Plasma Dust Acoustic Waves in the Strong-Coupling Regime*, Phys. Rev. Lett. **77**, 3137–3140 (1996).

[150] S. ZHDANOV, S. NUNOMURA, D. SAMSONOV, and G. MORFILL, *Polarization of wave modes in a two-dimensional hexagonal lattice using a complex (dusty) plasma*, Phys. Rev. E **68**, 035401 (2003).

[151] Z. DONKÓ, G. J. KALMAN, and P. HARTMANN, *Dynamical correlations and collective excitations of Yukawa liquids*, J. Phys.: Condens. Matter **20**, 413101 (2008).

[152] L. S. FROST, *Effect of Variable Ionic Mobility on Ambipolar Diffusion*, Phys. Rev. **105**, 354–356 (1957).

[153] P. BEZBARUAH and N. DAS, *Collisional effects on interaction potential in complex plasma in presence of magnetic field*, Phys. Plasmas **23**, 043701 (2016).

[154] G. SKADRON and J. WEINSTOCK, *Nonlinear stabilization of a two-stream plasma instability in the ionosphere*, J. Geophys. Res. **74**, 5113–5126 (1969).

[155] W. E. DRUMMOND, *Nonlinear Development of the Beam-Plasma Instability*, Phys. Fluids **13**, 2422 (1970).

[156] O. ISHIHARA, A. HIROSE, and A. B. LANGDON, *Nonlinear Saturation of the Buneman Instability*, Phys. Rev. Lett. **44**, 1404–1407 (1980).

[157] M. ROSENBERG, *A note on ion–dust streaming instability in a collisional dusty plasma*, J. Plasma Phys. **67**, 235–242 (2002).

[158] A. TJULIN, A. I. ERIKSSON, and A. MATS, *Physical interpretation of the Padé approximation of the plasma dispersion function*, J. Plasma Phys. **64**, 287–296 (2000).

[159] J. HEIMERL, R. JOHNSEN, and M. A. BIONDI, *Ion–Molecule Reactions, $He^+ + O_2$ and $He^+ + N_2$, at Thermal Energies and Above*, J. Chem. Phys. **51**, 5041–5048 (1969).

[160] S. ROBERTSON and Z. STERNOVSKY, *Monte Carlo model of ion mobility and diffusion for low and high electric fields*, Phys. Rev. E **67**, 046405 (2003).

[161] J. FERCH, B. GRANITZA, C. MASCHE, and W. RAITH, *Electron-argon total cross section measurements at low energies by time-of-flight spectroscopy*, J. Phys. B: At. Mol. Phys. **18**, 967 (1985).

[162] R. C. DAVIDSON, N. A. KRALL, K. PAPADOPOULOS, and R. SHANNY, *Electron Heating by Electron-Ion Beam Instabilities*, Phys. Rev. Lett. **24**, 579–582 (1970).

[163] M. ROSENBERG and P. SHUKLA, *Instability of obliquely propagating dust waves in a collisional highly magnetized plasma*, J. Plasma Phys. **73**, 189–197 (2007).

[164] J. W. A. M. GIELEN, M. C. M. van de SANDEN, and D. C. SCHRAM, *Plasma beam deposited amorphous hydrogenated carbon: Improved film quality at higher growth rate*, Appl. Phys. Lett. **69**, 152–154 (1996).

[165] S. PETER, K. GRAUPNER, D. GRAMBOLE, and F. RICHTER, *Comparative experimental analysis of the a-C:H deposition processes using CH_4 and C_2H_2 as precursors*, J. Appl. Phys. **102**, 053304 (2007).

[166] E. KOVAČEVIĆ, I. STEFANOVIĆ, J. BERNDT, Y. J. PENDLETON, and J. WINTER, *A Candidate Analog for Carbonaceous Interstellar Dust: Formation by Reactive Plasma Polymerization*, Astrophys. J. **623**, 242 (2005).

[167] H. B. NIEMANN, S. K. ATREYA, J. E. DEMICK, D. GAUTIER, J. A. HABERMAN, D. N. HARPOLD, W. T. KASPRZAK, J. I. LUNINE, T. C. OWEN, and F. RAULIN, *Composition of Titan's lower atmosphere and simple surface volatiles as measured by the Cassini-Huygens probe gas chromatograph mass spectrometer experiment*, J. Geophys. Res.: Planets **115**, E12006 (2010).

[168] K. DE BLEECKER, A. BOGAERTS, and W. GOEDHEER, *Detailed modeling of hydrocarbon nanoparticle nucleation in acetylene discharges*, Phys. Rev. E **73**, 026405 (2006).

[169] T. FUJII, *Diagnostics of microwave plasmas of* C_2H_2 *: Mass spectrometric investigations of ionic and neutral species*, Phys. Rev. E **58**, 6495–6502 (1998).

[170] C. DESCHENAUX, A. AFFOLTER, D. MAGNI, C. HOLLENSTEIN, and P. FAYET, *Investigations of* CH_4 *,* C_2H_2 *and* C_2H_4 *dusty RF plasmas by means of FTIR absorption spectroscopy and mass spectrometry*, J. Phys. D: Appl. Phys. **32**, 1876 (1999).

[171] J. BERNDT, E. KOVAČEVIĆ, I. STEFANOVIĆ, and L. BOUFENDI, *Controlled dust formation in pulsed rf plasmas*, J. Appl. Phys. **106**, 063309 (2009).

[172] A. BOUCHOULE and L. BOUFENDI, *Particulate formation and dusty plasma behaviour in argon-silane RF discharge*, Plasma Sources Sci. Technol. **2**, 204 (1993).

[173] E. KOVAČEVIĆ, J. BERNDT, T. STRUNSKUS, and L. BOUFENDI, *Size dependent characteristics of plasma synthesized carbonaceous nanoparticles*, J. Appl. Phys. **112**, 013303 (2012).

[174] U. KORTSHAGEN and U. BHANDARKAR, *Modeling of particulate coagulation in low pressure plasmas*, Phys. Rev. E **60**, 887–898 (1999).

[175] C. HOLLENSTEIN, J.-L. DORIER, J. DUTTA, L. SANSONNENS, and A. A. HOWLING, *Diagnostics of particle genesis and growth in RF silane plasmas by ion mass spectrometry and light scattering*, Plasma Sources Sci. Technol. **3**, 278 (1994).

[176] F. GREINER, J. CARSTENSEN, N. KÖHLER, I. PILCH, H. KETELSEN, S. KNIST, and A. PIEL, *Imaging Mie ellipsometry: dynamics of nanodust clouds in an argon–acetylene plasma*, Plasma Sources Sci. Technol. **21**, 065005 (2012).

[177] I. DENYSENKO, J. BERNDT, E. KOVACEVIC, I. STEFANOVIC, V. SELENIN, and J. WINTER, *The response of a capacitively coupled discharge to the formation of dust particles: Experiments and modeling*, Phys. Plasmas **13**, 073507 (2006).

[178] J. BERNDT, E. KOVAČEVIĆ, I. STEFANOVIĆ, O. STEPANOVIĆ, S. H. HONG, L. BOUFENDI, and J. WINTER, *Some Aspects of Reactive Complex Plasmas*, Contrib. Plasma Phys. **49**, 107–133 (2009).

[179] Y. HAYASHI, *Structure of a Three-Dimensional Coulomb Crystal in a Fine-Particle Plasma*, Phys. Rev. Lett. **83**, 4764–4767 (1999).

[180] A. P. HICKMAN, *Approximate scaling formula for ion–ion mutual neutralization rates*, J. Chem. Phys. **70**, 4872–4878 (1979).

[181] T. M. MILLER, *Parametrization of ion–ion mutual neutralization rate coefficients*, J. Chem. Phys. **72**, 4659–4660 (1980).

[182] B. K. JANOUSEK, J. I. BRAUMAN, and J. SIMONS, *An experimental and theoretical determination of the electron affinity of the ethynyl radical, HC_2*, J. Chem. Phys. **71**, 2057–2061 (1979).

[183] S. KNIST, F. GREINER, F. BISS, and A. PIEL, *Influence of Negative Ions on Drift Waves in a Low-Density Ar/O2-Plasma*, Contrib. Plasma Phys. **51**, 769–784 (2011).

[184] S. KNIST, *Einfluss negativer Ionen auf Driftwellen in einem Ar/O2-Plasma geringer Dichte*, doctoral thesis (Kiel University, 2012).

[185] H. C. van de HULST, *Light scattering by small particles* (Dover Pubn Inc, New York, 1957).

[186] H. KETELSEN, *Mie-Ellipsometrie an staubigen Plasmen*, diploma thesis (Kiel University, Sept. 2009).

[187] C. F. BOHREN and D. R. HUFFMAN, *Absorption and Scattering of Light by Small Particles* (John Wiley & Sons, New York, 1983).

[188] C. MÄTZLER, *MATLAB Functions for Mie Scattering and Absorption, Version 2*, IAP Res. Rep. (2002).

[189] C.-R. DU, K. R. SÜTTERLIN, K. JIANG, et al., *Experimental investigation on lane formation in complex plasmas under microgravity conditions*, New J. Phys. **14**, 073058 (2012).

[190] F. KIRCHSCHLAGER, S. WOLF, F. GREINER, S. GROTH, and A. LABDON, *In-situ analysis of optically thick nanoparticle clouds*, Appl. Phys. Lett. **110**, 173106 (2017).

[191] N.-H. REHBEHN, *Simulation von Streulichtexperimenten an staubigen Plasmen*, bachelor thesis, Kiel University, July 2017.

[192] H. KRÜGER, C. KILLER, S. SCHÜTT, and A. MELZER, *Characterization of injected aluminum oxide nanoparticle clouds in an rf discharge*, Plasma Sources Sci. Technol. **27**, 025004 (2018).

[193] C. KILLER and A. MELZER, *Global coherence of dust density waves*, Phys. Plasmas **21**, 063703 (2014).

[194] C. KILLER, *Abel Inversion Algorithm*, Matlab Central, 2013.

[195] G. PRETZLER, *A New Method for Numerical Abel-Inversion*, Zeitschrift für Naturforschung **46a**, 639–641 (1991).

[196] R. L. MERLINO, A. BARKAN, C. THOMPSON, and N. D'ANGELO, *Laboratory studies of waves and instabilities in dusty plasmas*, Phys. Plasmas **5**, 1607–1614 (1998).

[197] V. V. YAROSHENKO, S. A. KHRAPAK, H. M. THOMAS, and G. E. MORFILL, *Excitation of dust density waves in weak electric fields*, Phys. Plasmas **19**, 023702 (2012).

[198] J. D. WILLIAMS, E. THOMAS, and L. MARCUS, *Observations of vertically propagating driven dust acoustic waves: Finite temperature effects*, Phys. Plasmas **15**, 043704 (2008).

[199] E. THOMAS, *Driven dust acoustic waves with thermal effects: Comparison of experiment to fluid theory*, Phys. Plasmas **17**, 043701 (2010).

[200] J. L. DORIER, C. HOLLENSTEIN, A. A. HOWLING, and U. KROLL, *Powder dynamics in very high frequency silane plasmas*, J. Vac. Sci. Technol. A **10**, 1048–1052 (1992).

[201] K. O. MENZEL, O. ARP, and A. PIEL, *Frequency clusters and defect structures in nonlinear dust-density waves under microgravity conditions*, Phys. Rev. E **83**, 016402 (2011).

[202] J. F. NYE and M. V. BERRY, *Dislocations in Wave Trains*, Proc. R. Soc. Lond. A **336**, 165–190 (1974).

[203] T. BOCKWOLDT, *Strömungen und nichtlineare Dichtewellen staubiger Plasmen unter Schwerelosigkeit*, doctoral thesis (Kiel University, Dec. 2014).

[204] R. L. MERLINO, *Second-order dust acoustic wave theory*, Phys. Scr. **85**, 035506 (2012).

[205] J. R. HEINRICH, S.-H. KIM, J. K. MEYER, R. L. MERLINO, and M. ROSENBERG, *Secondary dust density waves excited by nonlinear dust acoustic waves*, Phys. Plasmas **19**, 083702 (2012).

[206] L.-J. HOU and A. PIEL, *Trapped particles by large-amplitude waves in two-dimensional Yukawa liquids*, Phys. Plasmas **15**, 073707 (2008).

[207] M.-C. CHANG, L.-W. TENG, and L. I, *Micro-origin of no-trough trapping in self-excited nonlinear dust acoustic waves*, Phys. Rev. E **85**, 046410 (2012).

[208] G. B. WHITHAM, *Linear and Nonlinear Waves* (John Wiley & Sons, Inc., June 1974).

[209] E. INFELD and G. ROWLANDS, *Nonlinear waves, solitons and chaos*, 2nd ed. (Cambridge University Press, 2000).

[210] T. BOCKWOLDT, O. ARP, K. O. MENZEL, and A. PIEL, *On the origin of dust vortices in complex plasmas under microgravity conditions*, Phys. Plasmas **21**, 103703 (2014).

[211] D. I. ZHUKHOVITSKII, *Dust acoustic waves in three-dimensional complex plasmas with a similarity property*, Phys. Rev. E **92**, 023108 (2015).

[212] F. MELANDSØ, T. ASLAKSEN, and O. HAVNES, *A new damping effect for the dust-acoustic wave*, Planet. Space Sci. **41**, 321–325 (1993).

[213] W. D. S. RUHUNUSIRI and J. GOREE, *Dispersion relations for the dust-acoustic wave under experimental conditions*, Phys. Plasmas **21**, 053702 (2014).

[214] I. DENYSENKO, K. OSTRIKOV, M. Y. YU, and N. A. AZARENKOV, *Behavior of the electron temperature in nonuniform complex plasmas*, Phys. Rev. E **74**, 036402 (2006).

[215] F. M. J. H. van de WETERING, R. J. C. BROOIMANS, S. NIJDAM, J. BECKERS, and G. M. W. KROESEN, *Fast and interrupted expansion in cyclic void growth in dusty plasma*, J. Phys. D: Appl. Phys. **48**, 035204 (2015).

[216] L. BOUFENDI, A. BOUCHOULE, and T. HBID, *Electrical characterization and modeling of a dust forming plasma in a radio frequency discharge*, J. Vac. Sci. Technol. A **14**, 572–576 (1996).

[217] M. HIMPEL, T. BOCKWOLDT, C. KILLER, K. OLE MENZEL, A. PIEL, and A. MELZER, *Stereoscopy of dust density waves under microgravity: Velocity distributions and phase-resolved single-particle analysis*, Phys. Plasmas **21**, 033703 (2014).

[218] M. SCHWABE, M. RUBIN-ZUZIC, S. ZHDANOV, H. M. THOMAS, and G. E. MORFILL, *Highly Resolved Self-Excited Density Waves in a Complex Plasma*, Phys. Rev. Lett. **99**, 095002 (2007).

[219] V. E. FORTOV, A. D. USACHEV, A. V. ZOBNIN, V. I. MOLOTKOV, and O. F. PETROV, *Dust-acoustic wave instability at the diffuse edge of radio frequency inductive low-pressure gas discharge plasma*, Phys. Plasmas **10**, 1199–1208 (2003).

[220] J. D. WILLIAMS, *Volumetric measurements of a spatially growing dust acoustic wave*, Phys. Plasmas **19**, 113701 (2012).

[221] M. HIMPEL, C. KILLER, T. BOCKWOLDT, K. MENZEL, A. PIEL, and A. MELZER, *Wave Crest Reconstruction of a Dust Density Wave Using Single Particle Trajectories*, IEEE Trans. Plasma Sci. **42**, 2676–2677 (2014).

[222] C. KILLER, M. HIMPEL, A. MELZER, T. BOCKWOLDT, K. O. MENZEL, and A. PIEL, *Oscillation Amplitudes in 3-D Dust Density Waves in Dusty Plasmas Under Microgravity Conditions*, IEEE Trans. Plasma Sci. **42**, 2680–2681 (2014).

[223] S. SCHÜTT, *Experimentelle Untersuchungen zu nichtlinearen Effekten in Staubdichtewellen*, master thesis (Kiel University, Aug. 2016).

[224] S. V. SINGH and N. N. RAO, *Effect of dust charge inhomogeneity on linear and nonlinear dust–acoustic wave propagation*, Phys. Plasmas **6**, 3157–3162 (1999).

[225] S. V. SINGH and N. N. RAO, *Linear and nonlinear dust-acoustic waves in inhomogeneous dusty plasmas*, Phys. Plasmas **5**, 94–99 (1998).

[226] R. M. CRUTCHER, *Magnetic Fields in Molecular Clouds*, Annu. Rev. Astron. Astrophys. **50**, 29–63 (2012).

[227] A. V. FILIPPOV, A. F. PAL, A. N. RYABINKIN, A. O. SEROV, and F. V. SHUGAEV, *Dusty waves and vortices in rf magnetron discharge plasma*, J. Phys. Conf. Ser. **946**, 012149 (2018).

[228] R. KAWAI and T. MIENO, *Effective Production of Negative Ions around Magnetized CF4 Plasma Column*, Jpn. J. Appl. Phys. **36**, L1123 (1997).

[229] M. SCHWABE, U. KONOPKA, P. BANDYOPADHYAY, and G. E. MORFILL, *Pattern Formation in a Complex Plasma in High Magnetic Fields*, Phys. Rev. Lett. **106**, 215004 (2011).

[230] E. THOMAS, B. LYNCH, U. KONOPKA, R. L. MERLINO, and M. ROSENBERG, *Observations of imposed ordered structures in a dusty plasma at high magnetic field*, Phys. Plasmas **22**, 030701 (2015).

[231] E. THOMAS, U. KONOPKA, R. L. MERLINO, and M. ROSENBERG, *Initial measurements of two- and three-dimensional ordering waves, and plasma filamentation in the Magnetized Dusty Plasma Experiment*, Phys. Plasmas **23**, 055701 (2016).

[232] D. LANGE, *Floating surface potential of spherical dust grains in magnetized plasmas*, J. Plasma Phys. **82**, 905820101 (2016).

[233] S. JAISWAL, T. HALL, S. LEBLANC, R. MUKHERJEE, and E. THOMAS, *Effect of magnetic field on the phase transition in a dusty plasma*, Phys. Plasmas **24**, 113703 (2017).

[234] E. THOMAS, U. KONOPKA, B. LYNCH, S. ADAMS, S. LEBLANC, R. L. MERLINO, and M. ROSENBERG, *Quasi-discrete particle motion in an externally imposed, ordered structure in a dusty plasma at high magnetic field*, Phys. Plasmas **22**, 113708 (2015).

[235] M. ROSENBERG, *On Dust Wave Instabilities in Collisional Magnetized Plasmas*, IEEE Trans. Plasma Sci. **44**, 451–457 (2016).

[236] H. KÄHLERT, J. CARSTENSEN, M. BONITZ, H. LÖWEN, F. GREINER, and A. PIEL, *Magnetizing a Complex Plasma without a Magnetic Field*, Phys. Rev. Lett. **109**, 155003 (2012).

[237] M. KLINDWORTH, A. PIEL, A. MELZER, U. KONOPKA, H. ROTHERMEL, K. TARANTIK, and G. E. MORFILL, *Dust-Free Regions around Langmuir Probes in Complex Plasmas under Microgravity*, Phys. Rev. Lett. **93**, 195002 (2004).

[238] I. GOERTZ, *Staub - Plasma Wechselwirkung in einer Doppelplasma-Anlage*, doctoral thesis (Kiel University, 2011).

[239] J. CARSTENSEN, H. JUNG, F. GREINER, and A. PIEL, *Mass changes of microparticles in a plasma observed by a phase-resolved resonance method*, Phys. Plasmas **18**, 033701, 033701 (2011).

[240] O. H. ASNAZ, H. JUNG, F. GREINER, and A. PIEL, *Size and density evolution of a single microparticle embedded in a plasma*, Phys. Plasmas **24**, 083701 (2017).

[241] C. SCHMIDT, O. ARP, and A. PIEL, *Spatially extended void-free dusty plasmas in a laboratory radio-frequency discharge*, Phys. Plasmas **18**, 013704 (2011).

[242] N. SATO, G. UCHIDA, T. KANEKO, S. SHIMIZU, and S. IIZUKA, *Dynamics of fine particles in magnetized plasmas*, Phys. Plasmas **8**, 1786–1790 (2001).

[243] U. KONOPKA, D. SAMSONOV, A. V. IVLEV, J. GOREE, V. STEINBERG, and G. E. MORFILL, *Rigid and differential plasma crystal rotation induced by magnetic fields*, Phys. Rev. E **61**, 1890–1898 (2000).

[244] V. N. NAUMKIN, D. I. ZHUKHOVITSKII, V. I. MOLOTKOV, A. M. LIPAEV, V. E. FORTOV, H. M. THOMAS, P. HUBER, and G. E. MORFILL, *Density distribution of a dust cloud in three-dimensional complex plasmas*, Phys. Rev. E **94**, 033204 (2016).

[245] F. CHEUNG, A. SAMARIAN, and B. JAMES, *The rotation of planar-2 to planar-12 dust clusters in an axial magnetic field*, New J. Phys. **5**, 75 (2003).

[246] K. MATYASH, M. FRÖHLICH, H. KERSTEN, G. THIEME, R. SCHNEIDER, M. HANNEMANN, and R. HIPPLER, *Rotating dust ring in an RF discharge coupled with a dc-magnetron sputter source. Experiment and simulation*, J. Phys. D: Appl. Phys. **37**, 2703–2708 (2004).

[247] M. VASIL'EV, L. D'YACHKOV, S. ANTIPOV, O. PETROV, and V. FORTOV, *Dusty plasma structures in magnetic fields in a dc discharge*, English, JETP Letters **86**, 358–363 (2007).

[248] M. SCHULZE, D. O'CONNELL, T. GANS, P. AWAKOWICZ, and A. von KEUDELL, *Rotation of a nanoparticle cloud in an inductively coupled plasma induced by weak static magnetic fields*, Plasma Sources Sci. Technol. **16**, 774 (2007).

[249] O. HAVNES, T. K. AANESEN, and F. MELANDSØ, *On dust charges and plasma potentials in a dusty plasma with dust size distribution*, J. Geophys. Res. **95**, 6581–6585 (1990).

Eidesstattliche Erklärung

Hiermit versichere ich an Eides statt, dass die vorliegende Dissertation – abgesehen von der Beratung durch den Betreuer und der Verwendung der angegebenen Hilfsmittel – nach Inhalt und Form meine eigene Arbeit ist. Sie hat weder ganz noch zum Teil schon einer anderen Stelle im Rahmen eines Prüfungsverfahrens vorgelegen. Die Arbeit ist unter Einhaltung der Regeln guter wissenschaftlicher Praxis der Deutschen Forschungsgemeinschaft entstanden.

Kiel, den 12. Juni 2018

.....

Danksagungen

An dieser Stelle möchte ich den Menschen danken, die diese Arbeit ermöglicht, zu ihrem Gelingen beigetragen oder mir Rückhalt gegeben haben.
An erster Stelle danke ich meinem Doktorvater, Herrn Prof. Dr. Alexander Piel, für die freundliche Aufnahme in seine Arbeitsgruppe Plasmadynamik. Seine Hinweise und Ratschläge haben meine Arbeit stets vorangebracht und seine Weitsicht über das konkrete Forschungsgebiet hinaus hat mir viele Erkenntnisse ermöglicht, die es ohne ihn nicht gegeben hätte. Seinem Einsatz ist es auch zu verdanken, dass der Sonderforschungsbereich SFB-TR24 von der Deutschen Forschungsgemeinschaft (DFG) eingeworben wurde. Daher gilt mein Dank Prof. Piel, der DFG und dem Land Schleswig-Holstein für die finanzielle Unterstützung und für die vielen Möglichkeiten, meine Forschungsergebnisse auf Tagungen und Workshops zu präsentieren und zu diskutieren. Prof. Dr. Jan Benedikt hat meine Stelle verlängert, wofür ich ihm dankbar bin.
Dr. Franko Greiner danke ich dafür, dass er mich frühzeitig für Laborarbeit und Plasmaphysik begeistert hat. Er hat mit Rat und Diskussionen dazu beigetragen, der Arbeit ihre Richtung zu geben, und hatte bei manchen Problemen den Blick für unkonventionelle Lösungsansätze. Ich möchte mich auch bei allen bedanken, die wichtige Vorarbeiten geleistet haben. Dazu gehören Dr. Jan Carstensen, bei dem ich meine ersten Lehrstunden in Laborarbeit genossen habe, und Dr. Sascha Knist, ohne den es das DUSTWHEEL in dieser Form nicht gäbe.
Ich danke meinen Ko-Doktoranden Hendrik Jung und Sebastian Groth, mit denen ich meinen wissenschaftlichen Werdegang bestreiten und gestalten durfte. Ich habe die Zeit mit ihnen genossen, im Labor, in den Kaffeerunden, auf Dienstreise und natürlich auch außerhalb der Universität. Dr. Jochen Wilms hatte immer ein offenes Ohr für mich, auch wenn es nicht um die Promotion ging.
Stephanie Thiedemann und Linda Sommer haben bei allen formalen Herausforderungen schnell und unkompliziert geholfen. Frank-Peter Hohmann danke ich für die Hilfe bei der Literaturbeschaffung. Volker Rohwer, Michael Poser und Mario Knüppel standen mir bei allen technischen Aufgaben mit Rat und Tat zur Seite, haben bei der Experimententwicklung mitgeholfen und hatten viele gute Ideen, die mit der Hilfe der Institutswerkstatt in die Tat umgesetzt werden konnten. Besonders hervorheben möchte ich in diesem

Zusammenhang den Werkstattleiter Michael Brix und den Mechaniker Tobias Marten. Bei allen Computerproblemen war Marek Anderson eine große Unterstützung.
Mit Malte Jacobsen als Bachelorand ist es das erste Mal gelungen, gute Videos von Staubdichtewellen aufzunehmen. Nils Rehbehn und Oguz Han Asnaz bin ich für ihren Einsatz dankbar, die Labor-Software zu verbessern. Sie haben meine Begeisterung für eine vollautomatische Experimentablaufsteuerung geteilt und bei ihrer Realisierung geholfen. Nils hat viele Geräte eigenständig programmiert, was sich bei meiner letzten Messkampagne ausgezahlt hat. Oguz Han hat mich immer mit Linux-Tipps versorgt. Dass er die DDW-D in 2D neu implementiert hat und in Zukunft am Leben erhalten möchte, ist für mich eine große Bestätigung – danke! Stefan Schütt und Dr. Tim Bockwoldt danke ich für zahllose Diskussionen rund um Wellen in staubigen Plasmen und Dr. Jan Schablinski dafür, dass er mich an das Mikrobank-System herangeführt hat. Viele weitere Kollegen und Büronachbarn haben den Arbeitsalltag verschönert und mit Kuchen versüßt, nämlich Jasmin Andersen, Prof. Dr. Dietmar Block, Tabea Gleiter, Dr. Judith Golda, Niklas Kohlmann, Armin Mengel, Dr. Christian Schmidt, Kerstin Sgonina und Frank Wieben. Besonderen Dank möchte ich auch dafür aussprechen, dass viele die Texte dieser Arbeit auf Rechtschreibfehler, Inkonsistenzen in der Argumentation oder schlechte Formulierungen durchgeschaut haben. Dies waren Dr. Franko Greiner, Dr. Judith Golda, Hendrik Jung, Sebastian Groth, Oguz Han Asnaz und Frederieke Maria Schnack. Ich danke Andreas Petersen für viele wertvolle Diskussionen über meine Diagramme und manche Idee, diese verständlicher zu machen. Darüber hinaus gilt allen mein Dank, die sich meinen Disputationsprobevortrag angehört und mit mir über Verbesserungsmöglichkeiten diskutiert haben.
Ferner danke ich auch allen, die mich außerhalb der Universität begleitet und mir Ablenkung und Freude geschenkt haben. Ich danke besonders Frederieke Maria Schnack für Vertrauen, Beistand und Geduld. Die Gespräche mit ihr haben mich immer bereichert.
Für Unterstützung, Ermutigung und Rat danke ich schließlich meinen Eltern Hans-Hinrich und Renate Johanna Tadsen sowie meiner Schwester Melanie Tadsen. Dies gilt nicht nur für die Zeit der Promotion.